

On The Habitability Of An Impacted Young Earth

ON THE HABITABILITY OF AN IMPACTED YOUNG EARTH: THE
EFFECTS OF A POST-IMPACT, REDUCING ATMOSPHERE ON
HADEAN EARTH'S HABITABILITY

By Kaitlin E. CERRILLO,

*A Thesis Submitted to the Department of Physics & Astronomy and the School of
Graduate Studies of McMaster University in the Partial Fulfillment of the
Requirements for the Degree of Master of Science*

McMaster University © Copyright by Kaitlin E. CERRILLO January 18, 2022

McMaster University

Master of Science (2022)

Hamilton, Ontario (Department of Physics & Astronomy)

TITLE: On The Habitability Of An Impacted Young Earth: The effects of a post-impact, reducing atmosphere on Hadean Earth's habitability

AUTHOR: Kaitlin E. CERRILLO (McMaster University)

SUPERVISOR: Dr. Ralph E. PUDRITZ

NUMBER OF PAGES: xvi, 101

Abstract

Atmospheres have an important role in determining whether a planet can both form and sustain life. In the case of early Earth under the faint young Sun, a heavy hydrogen-dominant atmosphere would have allowed for a temperate surface and the production of biomolecules necessary for life to form, such as HCN and H₂CO. This heavy atmosphere is thought to have been delivered to Earth by a large impact or series of large impacts on Earth's surface. In this work, we use a 1D radiative-convective equilibrium modelling code to obtain the thermal profiles for various post-impact atmospheres outlined by Zahnle et al. (2020). Our current results suggest that, in the work of Zahnle et al. (2020), early post-impact HCN yields were computed for atmospheres that are too hot for the necessary liquid surface water.

Acknowledgements

To both of my wonderful parents, for always supporting me and giving heartfelt congratulations when I do my best, regardless of the outcome. Thank you for continuing to encourage me into learning more and completing higher and higher levels of education that weren't accessible to either of you, even if part of the reason is to continue deferring payments on your Parent PLUS loans.

To my big sister Kahla, for always being the friendly competition in my life. I greatly appreciate the motivation you've given me through challenging times by becoming the first Dr. Cerrillo in the family so I can keep pushing to outdo you at every turn. I'll certainly usurp you in a few years after completing my next thesis.

To my cat Artemis, who assisted in the writing of this manuscript by walking across my keyboard as often as possible. Her contributions have been omitted from the final draft.

To my good friends Jeremy Karam and Veronika Dornan, for being a source of support and sanity through my mid-pandemic MSc. Those weekends at the cottage with some good food and games and our weekly Settlers of Catan sessions constituted the majority of the incredibly few things that kept me from giving up on my dreams and quitting online grad school to move to an off-grid yurt in the woods neither to be seen nor heard from again.

To Dr. Paul Mollière, who has been a source of invaluable knowledge through this journey. I appreciate the time you took every week to be an atmospheric and programming resource for us when the going got tough. I look forward to several more years of our ongoing collaboration through my upcoming PhD work.

To Dr. Ben K.D. Pearce, who taught me everything I know about writing a successful code and everything I know about the origins of life on Earth. I could not have completed

this thesis without you, and I am grateful for your guidance and contributions.

To the other members of my research group from 2019-2021: Dr. Matt Alessi, Rachel Pillsworth, Julie Inglis, Akash Shetty, Jess Speedie, and Gillian Bogert. I've learned much about the work I do and the life I live from you, and your guidance and support has left an impact on me professionally and personally. Like... don't worry, the impact was positive.

Very importantly, to Ms. Jan Guzzetta, my grade 3 teacher at Huth Road Elementary School, whose intense passion for learning — and for outer space — sparked something special in me. This has stuck with me ever since and has had a large impact on my academic career. I owe an excessively large part of where I am now to the endless inspiration I received from you then.

And most importantly, to my supervisor Dr. Ralph E. Pudritz, for taking a chance on a very-expensive-to-hire international student and fostering my continued passion for the work that I do. Your kindness, patience, encouragement, counsel, knowledge, and celebratory high-fives were the largest driving force behind the contents of this manuscript. Your extensive research interests and experience and your passion for STEM outreach continue to inspire me.

Thank you all.

- *Kaitlin*

Contents

| | |
|---|------------|
| Abstract | iii |
| Acknowledgements | iv |
| Declaration of Authorship | xv |
| 1 Introduction | 1 |
| 1.1 Life As We Know It | 2 |
| 1.1.1 Don't Be Such a Dim-Watt: Our faint young Sun | 2 |
| 1.1.2 Early Earth: A melted snowball | 5 |
| 1.1.3 Emergence of Life: Oceans | 5 |
| 1.1.4 Emergence of Life: Ponds | 6 |
| 1.1.5 Emergence of Life: Coming in with a <i>bang</i> | 8 |
| 1.2 Expanding Horizons | 9 |
| 1.2.1 <i>Pale New Dots: A vision of the exoplanets in space</i> (Sarl Cagan, 1994) | 9 |
| 1.2.2 Fetch, Sirius!: Exoplanet retrieval | 10 |
| 1.2.3 Give Me a Second: An atmosphere evolved | 11 |
| 2 Per Aspera Ad Atmosphaerās | 13 |
| 2.1 One D is Better Than Three: Solving the 1-dimensional atmosphere | 13 |
| 2.2 The German Connection: <i>petitRADTRANS</i> | 15 |
| 2.3 Written in Black & White: The grey atmosphere method | 17 |

| | | |
|----------|---|-----------|
| 2.4 | Heidelberg, We've Had a Problem: Modifying the code | 22 |
| 2.5 | An Adapted Code Comes to Life: <i>petitRADTRANS</i> and origins | 26 |
| 2.6 | A Titan of an Obstacle: Limitations in the model | 28 |
| 2.7 | Port of Entry: Customs and integration | 34 |
| 2.8 | Time Wars: Episode IV – A new code | 48 |
| 3 | The Habitability Of An Impacted, Young Earth | 50 |
| 3.1 | Methods | 53 |
| 3.1.1 | Models | 53 |
| 3.1.2 | Program | 55 |
| 3.1.3 | Procedure | 60 |
| 3.2 | Results – Thermal profiles | 62 |
| 3.3 | Results – Atmospheric chemistry | 67 |
| 3.4 | Discussion | 73 |
| 3.4.1 | Effects of Water | 78 |
| 3.4.2 | Effects of H ₂ | 79 |
| 3.4.3 | Possible Solutions | 80 |
| 3.4.4 | Relevance to the <i>Origins of Life</i> | 83 |
| 3.5 | Conclusions | 84 |
| | Bibliography | 86 |

List of Figures

| | | |
|-----|---|----|
| 2.1 | κ_{Pla} of our test Titan case using abundances from Yelle et al. (1997), the new two-temperature Planck mean from Malygin et al. (2014) for $T_{\text{rad}} = T_{\text{gas}}$, mimicking the old one-temperature treatment of <i>petitRADTRANS</i> 1.0 (blue), and for $T_{\text{rad}} = T_{\text{Sun}}$, the new treatment for our opacities in <i>petitRADTRANS</i> 1.5 (yellow). A clear order-of-magnitude increase in opacity from the one-temperature case is noted. | 24 |
| 2.2 | Tropospheric water vapour abundances for all 4 Hadean Earth models used by Pearce et al. (2022), computed using our addition of the Arden Buck equation (2.12) in <i>petitRADTRANS</i> 1.5. The values are given in molar mixing ratio, also known as mass fraction abundance. (Figure taken from Fig. S1, Pearce et al. 2022) | 26 |
| 2.3 | Comparison of <i>petitCODE</i> (green and blue) with our modified <i>petitRADTRANS</i> 1.5 (magenta) using our self-consistent H ₂ O abundances for our early Hadean reducing atmosphere (model A in Pearce et al. 2022; shown in Table 2.1 and Fig. 2.4) by Paul Mollière. | 27 |
| 2.4 | Pressure-Temperature profiles for all 4 Hadean Earth models used by Pearce et al. (2022), computed using our modified version of <i>petitRADTRANS</i> . (Figure taken from Fig. S2, Pearce et al. 2022) | 29 |

| | | |
|-----|---|----|
| 2.5 | The thermal profile (blue) of Titan computed self-consistently in the iterative Guillot version of <i>petitRADTRANS 1.5</i> , using measured abundances from, and compared with the measured thermal profile (yellow) from, Yelle et al. (1997). Our self-consistent temperature (blue) is much higher than the measured (yellow) value. | 30 |
| 2.6 | The thermal profile of Titan computed self-consistently in the iterative Guillot version of <i>petitRADTRANS 1.5</i> (blue), using measured abundances from, and compared with the measured thermal profile (yellow) from, Yelle et al. (1997). Of the abundances, with 10% of the N ₂ was replaced with O ₃ in the stratosphere of the blue curve, bound by 10 ⁻¹ and 10 ⁻⁴ bar. This caused the stratosphere of our blue curve to unexpectedly cool. | 32 |
| 2.7 | A plot of the absorption coefficient <i>k</i> vs. its cumulative probability (eqn. 2.13) for the 9.6μm absorption band of O ₃ at a pressure of 25mb and a temperature of 220K. This is shown as a function of wavenumber (left) and <i>g</i> (eqn. 2.13) (right). This demonstrates the necessity for a much higher resolution and more computationally intensive approach in a line-by-line opacity calculation than with the correlated-k method. (Plot from Fu and Liou 1992, Fig. 1) | 39 |
| 2.8 | The thermal profile of the Vesta 2 impactor case of Zahnle et al. (2020) (see Chapter 3) computed self-consistently in the newly ported version of <i>petitRADTRANS 2.0</i> (cyan), compared with the surface-less <i>petitCODE</i> (black). The vertical line shows the new surface temperature value from <i>petitRADTRANS 2.0</i> . It shows that this new ground interaction of the incoming stellar light must increase the surface temperature to balance the incoming and outgoing fluxes. | 46 |

| | | |
|-----|---|----|
| 2.9 | A modern Earth PT profile computed with the newest version of <i>petitRADTRANS 2.0</i> by Paul Mollière. The new surface temperature (vertical, dark blue line) does not account for latent heat release via water evaporation. The layer above has a temperature $T = 289.42$ K, very comparable to the average Earth surface temperature of $T_{surf} = 288$ K. Due to the current lack of a self-consistent chemistry code, the value of $\gamma = c_P/c_V$ was adjusted by eye based on the modern Earth’s moist γ until the calculated and observed PT profiles matched in their stratospheres (see section 3.1.2) (Mollière 2021b). | 48 |
| 3.1 | The self-consistent PT profiles for the dry atmosphere cases of Zahnle et al. (2020), using the input chemistry abundances found in Table 3.1 (Z_D). The bold sections of the thermal profiles indicate convective regions. The impactor in each plot represents the value for the surface temperature solution from Zahnle et al. (2020), found in Table 3.3, to allow for visual comparison between the analytic and computed surface temperatures. | 63 |
| 3.2 | The self-consistent PT profiles for the wet atmosphere cases of Zahnle et al. (2020), using the input chemistry abundances found in Table 3.1, and allowing H_2O to be built from the input chemistry as discussed in Section 3.1.3 (Z_W). The bold sections of the thermal profiles indicate convective regions. The impactor in each plot represents the value for the surface temperature solution from Zahnle et al. (2020), found in Table 3.3, to allow for visual comparison between the analytic and computed surface temperatures. The solutions for Sub Vesta 1 and South Pole Aitken 2 diverged, failing to meet convergence criteria, and are only included for completeness. | 66 |

| | | |
|-----|---|----|
| 3.3 | The self-consistent PT profiles for the dry atmosphere cases of Zahnle et al. (2020), with the opacity contribution of H ₂ -H ₂ collisions omitted from the radiative transfer, using the input chemistry abundances found in Table 3.1 (<i>H_D</i>). The bold sections of the thermal profiles indicate convective regions. The impactor in each plot represents the value for the surface temperature solution from Zahnle et al. (2020), found in Table 3.3, to allow for visual comparison between the analytic and computed surface temperatures. | 68 |
| 3.4 | The contribution of the collisional induced absorption of H ₂ -H ₂ collisions to the optical depth at each wavelength, applied to the surface layers of the <i>Z_D</i> cases with $\tau_{min,vis}^{surface} > 1$. The opacities are calculated accounting for the abundance of H ₂ , pressure, and temperature at the lowest layer of the atmosphere. This contribution to the optical depth is excluded from the thermal profile calculations of the <i>H_D</i> cases. | 69 |
| 3.5 | The self-consistent PT profiles for the wet atmosphere cases of Zahnle et al. (2020), with the opacity contribution of H ₂ -H ₂ collisions omitted from the radiative transfer, using the input chemistry abundances found in Table 3.1 and allowing H ₂ O to form from these input abundances (<i>H_W</i>). The bold sections of the thermal profiles indicate convective regions. The impactor in each plot represents the value for the surface temperature solution from Zahnle et al. (2020), found in Table 3.3, to allow for visual comparison between the analytic and computed surface temperatures. Vesta 1 and Vesta 2 strayed far from convergence, and are included for completeness. | 70 |

| | | |
|-----|---|----|
| 3.6 | The self-consistent number fraction abundances of the resulting chemistry species for the dry atmosphere cases of Zahnle et al. (2020), using the input chemistry abundances found in Table 3.1 (Z_D). The x-axes are plotted in a logarithmic scale for ease of differentiating the lower number mass abundances from the dominant species. An arbitrary cutoff number to plot the number fraction of each species was chosen because a very small number fraction is $\sim 0\%$ of the composition. | 73 |
| 3.7 | The self-consistent number fraction abundances of the resulting chemistry species for the wet atmosphere cases of Zahnle et al. (2020), using the input chemistry abundances found in Table 3.1, and allowing H_2O to form from the input species as describe in Section 3.1.3 (Z_W). For H_2O , g denotes the gas phase, l denotes the liquid phase, and c denotes the crystalline phase. The x-axes are plotted in a logarithmic scale for ease of differentiating the lower number mass abundances from the dominant species. An arbitrary cutoff number to plot the number fraction of each species was chosen because a very small number fraction is $\sim 0\%$ of the composition. | 74 |
| 3.8 | The self-consistent number fraction abundances of the resulting chemistry species for the dry atmosphere cases of Zahnle et al. (2020) without H_2 - H_2 collisional opacity, using the input chemistry abundances found in Table 3.1 (H_D). The x-axes are plotted in a logarithmic scale for ease of differentiating the lower number mass abundances from the dominant species. An arbitrary cutoff number to plot the number fraction of each species was chosen because a very small number fraction is $\sim 0\%$ of the composition. | 75 |

| | | |
|-----|--|----|
| 3.9 | The self-consistent number fraction abundances of the resulting chemistry species for the wet atmosphere cases of Zahnle et al. (2020) without H ₂ -H ₂ collisional opacity, using the input chemistry abundances found in Table 3.1, and allowing H ₂ O to form from the input species as describe in Section 3.1.3 (<i>H_W</i>). For H ₂ O, <i>g</i> denotes the gas phase, <i>l</i> denotes the liquid phase, and <i>c</i> denotes the crystalline phase. The x-axes are plotted in a logarithmic scale for ease of differentiating the lower number mass abundances from the dominant species. An arbitrary cutoff number to plot the number fraction of each species was chosen because a very small number fraction is ~0% of the composition. | 76 |
|-----|--|----|

List of Tables

| | | |
|-----|---|----|
| 2.1 | Summary of the 4 Hadean Earth models we computed for Pearce et al. (2022) using our modified <i>petitRADTRANS</i> . (Table summarized from Table 2, Pearce et al. 2022) | 28 |
| 3.1 | Table of impact models adapted from Zahnle et al. 2020 | 55 |
| 3.2 | List of model shorthand and meaning for this work. | 61 |
| 3.3 | Comparison of Zahnle et al. (2020) analytic surface temperature solutions using Eq. 3.1 to our self-consistent surface temperature calculations from Zahnle et al. (2020), Table 3.1. | 71 |
| 3.4 | Self-consistent Bond albedo for each atmosphere. | 72 |

Declaration of Authorship

I, Kaitlin E. CERRILLO, declare that this thesis titled, “On The Habitability Of An Impacted Young Earth: The effects of a post-impact, reducing atmosphere on Hadean Earth’s habitability” and the work presented in it are my own. I confirm that:

- **Chapter 1:** Written by Kaitlin E. Cerrillo with contributions from Dr. Ralph E. Pudritz
- **Chapter 2:** Written by Kaitlin E. Cerrillo with contributions from Dr. Ralph E. Pudritz, and includes a discussion of the contributions by Kaitlin E. Cerrillo to Pearce et al. (2022) and a summary of their findings.
 - *petitRADTRANS* and *petitCODE* were scripted by Dr. Paul Mollière
 - Initial modifications to *petitRADTRANS*, as outlined in section 2.4, were made by Kaitlin E. Cerrillo and Dr. Ben K.D. Pearce with guidance from Dr. Paul Mollière
 - Later modifications to *petitRADTRANS*, as outlined in section 2.7, were made by Kaitlin E. Cerrillo, Dr. Ben K.D. Pearce, and Dr. Paul Mollière
 - Presented test simulations in *petitRADTRANS* performed by Kaitlin E. Cerrillo and Dr. Paul Mollière
 - Comparison early Earth simulation in *petitCODE* made by Dr. Paul Mollière using data from simulation by Kaitlin E. Cerrillo and Dr. Ben K.D. Pearce
 - Early Earth atmosphere Pressure-Temperature profiles run by Kaitlin E. Cerrillo and Dr. Ben K.D. Pearce
 - Modern Earth test in the newest *petitRADTRANS* by Dr. Paul Mollière

- **Chapter 3:** Written by Kaitlin E. Cerrillo with contributions from Dr. Ralph E. Pudritz and Dr. Paul Mollière.
 - Based on work by Zahnle et al. (2020)
 - *petitCODE* scripted by Dr. Paul Mollière
 - All equilibrium atmospheric simulations run by Kaitlin E. Cerrillo

Chapter 1

Introduction

“Our land is more valuable than your money. It will last forever. . . As long as the Sun shines and the waters flow, this land will be here to give life. . .”

- Chief Crowfoot of the Siksiká Nation (c. 1885)

The origin of life on Earth is widely suspected to have required the presence of liquid water, along with the biomolecules used to build the nucleobases of RNA and DNA (Nisbet and Fowler 1996). The necessary existence of certain prebiotic molecules to form nucleobases — methane, ammonia, formaldehyde, and hydrogen cyanide — was first emphasized by Oparin (1938). An atmospheric source of these nucleobases has been recurrent throughout origins-of-life literature, starting with Haldane (1929) & Oparin (1938), and including Miller and Urey (1959), Schlesinger and Miller (1983), Zahnle (1986), Stribling and Miller (1987), and Pearce et al. (2022). These molecules inherently form best in a hydrogen-rich atmosphere, with very little oxygen, called a reducing atmosphere. The origins of such a heavy hydrogen atmosphere’s existence on Earth’s low mass are not fully understood, but current investigations suggest that this atmosphere would have formed following a large impact event or series of large impact events on Earth’s surface.

This thesis examines the post-impact state of Earth’s early atmosphere. A planet’s surface temperature is dictated by the balance of energy between incoming stellar light and outgoing thermal emissions. The atmosphere of a planet plays an important role in determining how much of this stellar light reaches the surface, and how much outgoing thermal emission is trapped. Here, we show that such reducing atmospheres may have rendered Earth uninhabitable — i.e., too hot for liquid water to have formed on its surface. Within this thesis, Chapter 1 outlines the state of the fields for origins of life on Earth and exoplanet study, Chapter 2 discusses numerical methods for solving the thermal profile of early Earth and modifications made for this work, and Chapter 3 presents the results of our investigation.

1.1 Life As We Know It

1.1.1 Don’t Be Such a Dim-Watt: Our faint young Sun

In his book *Structure and Evolution of the Stars*, Schwarzschild (1958) made some of the first recognition in scientific literature to the possibility of a variation in solar luminosity over the Sun’s early evolution (Sagan and Mullen 1972). He alluded to the implications that this realization would have on the history of Earth, stating that it could not go without geological or geophysical consequences that may ultimately be detectable on Earth, allowing for further study of this Faint Young Sun (Schwarzschild 1958).

Schwarzschild et al. (1957) first ran computational models that accounted for the Sun’s deep convection layer and formation of hydrogen into helium. They characterized the radiative interiors of the Sun using

$$C = \frac{3}{4ac} \left(\frac{k}{HG} \right)^{7.5} \frac{6.52 \times 10^{24}}{(4\pi)^{2.75}} \left(Z + \frac{X+Y}{59.3} \right) \frac{(1+X)^{0.75}}{\mu^{7.5}} \frac{LR^{1.25}}{M^{5.75}} \quad (1.1)$$

$$D = \left(\frac{HG}{k}\right)^{4.5} \frac{2.8 \times 10^{-33}}{4\pi} X^2 \mu^{4.5} \frac{M^{6.5}}{LR^{7.5}}, \quad (1.2)$$

where C is the mass-luminosity coefficient, and D is the energy output relation (Schwarzschild et al. 1957). Here, M is the solar mass, L is the luminosity of the Sun at time t , R is the radius of the Sun at time t , and μ is the reduced mass of the gas. We defer to Osterbrock (1953) for the definitions of the remaining variables therein, and discuss here only those relevant to the story of our faint young Sun. Notably, these equations are dependent upon X , the abundance of hydrogen; Y , the abundance of helium; and Z , the abundance of heavier elements, generally referred to as "metals." During the fusion of hydrogen into helium, the rate at which the hydrogen decreases was used by Schwarzschild et al. (1957) as

$$\frac{dX}{d\tau} = -\frac{\epsilon}{6.3 \times 10^{18}}, \quad (1.3)$$

in which dX is the change in hydrogen abundance over a period of time $d\tau$, and ϵ is the amount of energy generated by the ongoing hydrogen fusion, $\epsilon = 2.8 \times 10^{-33} X^2 \rho T^{4.5}$. The large possible errors in thermonuclear reaction rates and solar atmospheric opacity were later found to have negligible affect on the change in luminosity over time when compared with constraining solar age and initial Y value after the Sun's formation, both of which can be determined through geologic observations of Earth, the Moon, and asteroids (Sagan and Mullen 1972).

By removing R from equations 1.1 and 1.2 to avoid uncertainties due to radial contraction as the Sun formed, and assuming a constant mass M due to the Sun's non-fusing convective layers and negligible loss in total mass as the energy from fusion is released, Schwarzschild et al. (1957) found that the luminosity L is time-dependent in its proportionality $L \propto C^{1.2} D^{0.2}$. This is due to the change in certain values over time, e.g. the abundance of hydrogen via equation 1.3, altering the energy output and mass-luminosity

relation over time. They concluded that, over the last 5 Ga, the Sun would have increased in brightness by 0.5 mag, corresponding to a luminosity change ΔL by a factor of 1.6, providing an expected L at 5 Ga of $L = 0.63L_{\odot}$. Their computations for such a young Sun did not account for the higher luminosity of a contracting proto-star along its pre-main-sequence path. At 2.0 Ga, during the pre-Cambrian era, they found that the Sun’s luminosity would have been 20% lower than the modern $L_{\odot} = 3.839 \times 10^{33} \text{ ergs}^{-1}$. These values are consistent with the newer findings of Heller et al. (2020), who concluded that the solar luminosity at 4.5 Ga, after the Sun’s formation onto the main sequence, was below $0.70L_{\odot}$, and that the solar luminosity at 2.0 Ga was $\sim 0.80L_{\odot}$, supporting the early findings of Schwarzschild et al. (1957).

Over the following decade, stellar and solar scientists continued investigating the change in the Sun’s luminosity over geologic time using newly emerging stellar models and methods of computation. These values ranged from as little as 30% (e.g. Ezer and Cameron 1965), to as much as 50%-60% (e.g. Hoyle in *Stellar Populations* 1958; Schwarzschild et al. 1957, respectively). Sagan and Mullen (1972) concluded that the weighted mean of these computed values for ΔL over geologic time is $\Delta L = 40\% \pm 10\%$. Using a more conservative $\Delta L = 30\%$, they determined that the young Earth would have been a snowball, frozen until ~ 2.3 Ga. Since ice is very reflective, Newman and Rood (1977) also recognized that the solar constant must be raised to $1.3\times$ its modern value for a glacial Earth to melt. The findings of Sagan and Mullen (1972) and Newman and Rood (1977) raise an important disparity in Earth’s history: if Earth were to remain frozen over until 2.3 Ga, with a flux higher than that of today to thaw a full snowball Earth, how does fossilized evidence of single-celled life exist by 3.4 Ga (Wacey et al. 2011), with strong evidence of oxygenic photosynthesis by 2.95 Ga (Planavsky et al. 2014)?

1.1.2 Early Earth: A melted snowball

Evidence of a liquid water surface exists in Earth’s zircon record. Zircons are minerals that crystallize out of molten, silicate-based magma, where silicates are a class of minerals comprised of silicon and oxygen. These zircons show that, due to their formation temperature of $\sim 644\text{--}801^\circ\text{C}$, a portion of Earth’s surface was kept above freezing between 4.0 and 4.3 Ga (Watson and Harrison 2005). The enrichment of ^{18}O in zircons that formed 3.9–4.4 Ga shows that Earth would have had liquid water oceans at this time; however, some of this heavy oxygen enrichment may have possibly taken place in a sub-surface ocean, covered by ice (Pearce et al. 2018).

This enrichment of ^{18}O is defined using the equation

$$\delta^{18}\text{O} = \left(\frac{\left(\frac{^{18}\text{O}}{^{16}\text{O}} \right)_{\text{sample}}}{\left(\frac{^{18}\text{O}}{^{16}\text{O}} \right)_{\text{standard}}} - 1 \right) \times 1000\text{‰}. \quad (1.4)$$

Of these results, $\delta^{18}\text{O}$ values greater than 6.5‰ were determined to have formed from interaction of liquid water and a solidified crust (Valley et al. 2005). This $\delta^{18}\text{O} > 6.5\text{‰}$ has been measured in zircons dating back to 3.91–4.40 Ga. While it is possible that these zircons formed in a sub-surface ocean, these zircons have been interpreted across the geological literature as evidence for liquid surface water at the time of their formation (e.g. Pearce et al. 2018 and references therein). Attwater et al. (2013) were able to demonstrate that, under idealized lab conditions, RNA is able to polymerize in ice water as cold as -19°C . This lends some validation to the idea that a crust of ice may have covered Earth at the time that life began and the zircons formed beneath frozen surface, but the mechanisms by which life forms are not possible sub-surface.

1.1.3 Emergence of Life: Oceans

The emergence of the first reproducing cells on Earth in deep regions of the ocean at warm, hydrothermal vent systems was first proposed by Russell et al. (1993). Ballard

(1977) first discovered hydrothermal ocean vents 330km off of the northeastern coast of the Galápagos Islands. This region of the ocean floor had previously shown unexpected temperature patterns of Earth’s crust. Since The Galápagos Islands are a volcanic archipelago, they exist on a rift where Earth’s crust is separating due to tectonic activity. This rift had already been found to be similar to other sub-ocean rifts, such as the Mid-Atlantic Ridge, but the interesting patterns in temperature suggested a hydrothermal system created by the newly-formed crust at the ridge, indicating a flow of hot water from Earth’s interior at the ocean floor (Ballard 1977).

Samples of the water from The Galápagos Ridge showed high concentrations of hydrogen sulfide (H_2S), a food source for the bacteria that lived near the vents, which in turn functioned as a food source for other deep-sea organisms; this vent system was able to sustain a food chain of life without the need for sunlight from the surface (Ballard 1977). This infers the possibility of life forming beneath an icy, frozen ocean. Hydrothermal vent systems are host to chemical ingredients and thermal gradients that life can utilize for energy, and abiotic catalysts that can perform the roles of biotic enzymes. It has also already been found that the oldest common universal ancestor of life on Earth was most likely bacteria from hydrothermal vent regions (Rimmer and Shorttle 2019 and references therein); however, the nitrogen welling up from these hot vents in the form of ammonia (NH_3) would not have been in sufficient concentration to sustain the supply of necessary prebiotic chemistry both inside of a vent system and the surrounding waters (Schoonen and Xu 2001). It is also unlikely that RNA could have formed in such alkaline (pH ~9-11) hydrothermal environments, because RNA is most stable in acidic environments with a pH of 4-5 (Bernhardt and Tate 2012).

1.1.4 Emergence of Life: Ponds

The solution to these oceanic complications is via a wet-dry cycle in warm little ponds on Earth’s surface (e.g. Pearce et al. 2017; Pearce et al. 2022), first proposed by Charles

Darwin in correspondence with Sir Joseph Dalton Hooker (Peretó et al. 2009). This lends credence to the liquid *surface* water interpretation of the zircon record. Two important prebiotic molecules for life are hydrogen cyanide (HCN) and formaldehyde (H₂CO). When concentrated in one of these warm little ponds on Earth’s surface, HCN and H₂CO are able to form adenine, guanine, cytosine, uracil, and thymine, all of which are nitrogen-bearing biomolecules (Pearce et al. 2022). These biomolecules can then chain into long biopolymers, forming the helical structures of RNA and DNA. HCN and H₂CO can also form ribose, which functions as the backbone for RNA (Pearce et al. 2022). While it is possible for HCN and H₂CO to have been delivered via small meteorites to the ponds, they can also form via lightning and UV-driven chemistry in a reducing atmosphere before raining out into ponds. The drawback of a meteorite delivery system of biomolecules to these warm little ponds is that they would be destroyed within months through interactions with water, seepage through the pond’s walls, and degradation by UV rays. Due to this very transient biomolecule yield, a reducing chemistry atmosphere seems more likely to provide consistent concentrations of nucleobases via atmospheric precipitation, and can for over 100 Myr (Pearce et al. 2022).

It not enough for the HCN and H₂CO to rain out: is also necessary for the ponds to undergo a wet-dry cycle to polymerize the biomolecules into RNA or DNA (Rimmer and Shorttle 2019). Laboratory experiments have already concluded that only a few wet-dry cycles (1-16) are able to polymerize these essential biomolecules into chains of RNA with over 300 of these base molecules (Da Silva et al. 2015). This helps to further guide the zircon interpretation that the liquid water was present on Earth’s surface at this time, and demonstrates that Earth needed to be at the right temperature for a liquid water cycle.

1.1.5 Emergence of Life: Coming in with a *bang*

An atmosphere is characterized as either oxidized or reduced by the ratio of hydrogen to other atomic abundances that would attach to a carbon scaffold in a molecule, such as oxygen and nitrogen (Benner et al. 2020). The more reduced an atmosphere’s chemistry is, the higher amount of hydrogen will be present. From the experiments of Miller and Urey (1959), the biomolecules necessary for life to form would require a highly reduced atmosphere; however, geologic evidence of the mantle and CO₂-dominant volcanic outgassing suggests that Earth has been oxidized since its formation (Benner et al. 2020; Zahnle et al. 2020). Importantly, due to hydrogen’s ability to escape from a terrestrial mass planet by easily exceeding the escape velocity, Earth would not have been able to sustain the reduced chemistry necessary for life from its formation in the disk (Zahnle et al. 2020). The currently available literature thus points in one direction to remedy the current complications: a large mass impactor would be able to generate a transient reducing atmosphere, discussed further in Chapter 3 (Benner et al. 2020).

This transient reducing atmosphere would have initially contained a large amount of hydrogen. A large impactor rich in iron would have melted upon impact, and interacted with the water from the subsequently evaporated oceans, forming iron oxide (FeO) and diatomic hydrogen (H₂) (Zahnle et al. 2020). Not only would this reduced chemistry H₂ have created favourable atmospheric conditions for prebiotic chemistry, it could have provided a substantial greenhouse effect on Earth under the Faint Young Sun, warming it enough to sustain the necessary liquid water cycle (Zahnle et al. 2020; Pearce et al. 2022). For our modern Sun, with modern Earth’s atmospheric chemistry, the habitable zone of our solar system extends to ~1.7 AU. The habitable zone is characterized as the region around the Sun in which liquid water could remain stable on a rocky planet’s surface (Ramirez and Kaltenegger 2017). Ramirez and Kaltenegger (2017) determined that, by adding 30% H₂ to an Earth-like terrestrial atmosphere via volcanic outgassing, the modern Sun’s habitable zone can be extended out to ~2.23 AU. This same 30%

abundance of atmospheric H₂ was also found to decrease the solar flux necessary to maintain liquid water in the current habitable zone by 44%, consistent with the stellar luminosity changes calculated by Heller et al. (2020) and Schwarzschild et al. (1957).

1.2 Expanding Horizons

1.2.1 *Pale New Dots: A vision of the exoplanets in space*

(Sarl Cagan, 1994)

The first documented exoplanet discovery was published by Campbell et al. (1988), which was not verified to be a true exoplanet finding until corroborated by Hatzes et al. (2003). In their work studying the Doppler shifting of stellar spectra, they found long-term 2.7 year variations in their measured radial velocity alongside the large-amplitude signature of the γ Cephei binary system’s orbit. They concluded this variability is caused by the existence of a $1\text{-}9M_{Jup}$ planetary orbiting companion within the binary system, which was later confirmed to be a $\sim 13\text{-}16M_{Jup}$ companion orbiting the primary star of the system, γ Cephei A, with an orbital semi-major axis of 2.13 AU (Hatzes et al. 2003).

By 2009, fifteen exoplanets of less than 10 Earth masses (M_{\oplus}) had been discovered and confirmed (Kaltenegger and Traub 2009). According to NASA’s *Exoplanet Archive*, this number has risen to 376 exoplanets $<10M_{\oplus}$ of the over 4,000 total discovered and verified by end of 2021. Notable terrestrial-mass, rocky planets found orbiting in their system’s habitable zone are the seven planets of the Trappist 1 system (Gillon et al. 2017) and the nearby Proxima Centauri B (Anglada-Escudé et al. 2016), with both of these systems centred around an M-class dwarf star. While little data for terrestrial exoplanets currently exists for their spectral features and composition, this is expected to change quickly using the high-resolution near-IR spectrographs on-board *TESS*, *JWST*, and *PLATO* (Herbort et al. 2020). These instruments will give scientists a glimpse at the atmospheric composition of nearby exoplanets using the spectrographic absorption

and emission features of the atmospheres during primary and secondary transits of their host stars (Belu et al. 2011; Ricker et al. 2015).

1.2.2 Fetch, Sirius!: Exoplanet retrieval

In the field of exoplanet astronomy, retrieval refers to the process by which planets are characterized via their spectra (Mollière et al. 2019). Generally, forward-model retrieval codes will produce spectra for exoplanet atmospheres, before working back to solve for the model parameters that best fit the observed spectra (Barstow et al. 2020). These synthetic spectra are then compared to the observed spectra, and if their percent difference is larger than a certain value, the properties of the atmosphere are altered and a new spectrum is computed and compared. This method of characterization began as a way for astronomers to better understand the physical properties of planets within our own solar system using Earth-based satellite telescopes (Irwin et al. 2008). When matching a synthetic, computer-generated spectrum to observation, astronomers are able to tune the free parameters of the model, creating a distribution of parameters that may correspond with the atmospheric properties encoded in the spectrogram. Retrieval is typically carried out using low-resolution data from *Spitzer* and *Hubble*, but modern higher-resolution data, such as that expected from *JWST*, may allow astronomers a glimpse of atmospheric evolution processes (Mollière and Snellen 2018).

While deeper understanding through new detections is on the horizon for exoplanet astronomers, understanding terrestrial planets may pose a significant challenge. It is clear that, for small mass bodies, it is easy for UV radiation to break apart H₂O molecules, giving the lightweight H₂ the ability to escape, while the heavier oxygen remains behind (e.g. Zahnle et al. 2013). This does not hold for larger mass objects, such as the gas and ice giants of our solar system, that have sustained their post-formation primary atmospheres (Catling and Kasting 2017). This mechanism allows a low mass

planet to have both a primary (accreted) atmosphere, and a secondary (outgassed) atmosphere, following the loss of hydrogen to space, and the rate at which this atmosphere escapes is dependent upon the planetary mass and planetary temperature.

1.2.3 Give Me a Second: An atmosphere evolved

Over time, following the large Hadean impact event(s), the atmosphere of Earth oxidized. It is generally believed that Earth’s highly oxidized modern atmosphere was generated from respiration of photosynthetic life; however, the 200-700 Myr discrepancy between the formation of this photosynthetic life and the resulting highly oxidized atmosphere is theorized to have been caused not by this new life respiring O_2 , but by cooling ocean floors. This cooling would have lead to the loss of an H_2 outgassing source through lower serpentinization — the incorporation of water into a mineral’s crystal structure — of rocks on the ocean floor (Kasting 2013). This decrease in H_2 also made O_2 more stable at Earth’s surface than competing molecules such as CH_4 (Zahnle et al. 2013). Secondary-atmosphere constituent species are also more easily dissolved in magma than H_2 , with the ability to be outgassed later (Kite and Barnett 2020). As the general surface conditions in our solar system are oxidized (Zahnle et al. 2013), this process of atmospheric transmutation is expected to be ubiquitous among Earth-like exoplanets (Kite and Barnett 2020).

This mechanism has already been seen in $6M_{\oplus}$ exoplanets, whose $1.6R_{\oplus}$ radius implies a density consistent with total H_2 loss (Rogers 2015). Due to strong differences in chemistry of primary and secondary atmospheres, a reading of a planet may not provide a full picture of a planet’s habitability, especially considering the rate of detection of possibly old, $\sim 1 M_{\oplus}$ planets surrounding very long-lived M-type stars (Herbort et al. 2020). Mars is an important example of this, not only due to its proximity to Earth, but due to evidence of past liquid surface water. Mineralogical and geomorphological evidence shows that Mars’ primary atmosphere may have been capable of supporting

not only sustained liquid surface water, but mineral-rich and acidic water, spurring the search for evidence of past life on its surface (e.g. Fukushi et al. 2019). When detecting an exoplanet and determining its habitability, how well can we constrain its ability to host life without the full high-resolution picture of its atmospheric chemistry, proper detection of mass and radius, and expected level of hydrogen escape?

The goal of this thesis is to determine the habitability of a terrestrial planet based on its atmospheric chemical composition, with a focus on the currently only-known life-bearing planet: Earth. In particular, we perform a detailed investigation into the properties of a post-impact atmosphere, due to the likelihood that this transient atmosphere was dominant when life first emerged on Earth. This composition plays an important role in determining surface temperatures, possibly extending the habitable zone, as must have occurred with young Earth under our faint young Sun. The composition also dictates the amount of surface pressure, changing the temperature ranges in which liquid water is able to form. Investigating the complex interactions of the molecular species in newly discovered terrestrial-mass exoplanets may ultimately show that more planets than we realized are habitable, and a few may have the right cocktail of reducing chemistry to beget life of their own.

Chapter 2

Per Aspera Ad Atmosphaerās

Numerical methods

This thesis involved ongoing exploratory numerical work to determine which computational method is most appropriate for investigating the thermal profile of a terrestrial planet’s atmosphere, and investigate the hypothetical steady-state atmosphere present on Earth following the majority of its large impacts. In this chapter, that exploration is presented in its entirety. Firstly, we chose a widely-used semi-grey analytic method by Guillot (2010), common in exoplanet retrieval models. This method was then tested, modified, and found to be unsuitable for our studies. A less restrictive modelling method was tested and found to overcome the previous model’s limitations. This numerical method used for the results presented in Chapter 3 and its development are discussed in section 2.7.

2.1 One D is Better Than Three: Solving the 1-dimensional atmosphere

Many modern retrieval codes can be traced back to Toon et al. (1989) and their one-dimensional model (e.g. McKay et al. 1989; Marley et al. 1996; Fortney et al. 2008).

Their method was designed to compute the radiative transfer in a one-dimensional non-homogeneous atmosphere, quickly, and while accounting for scattering of thermal emission. They implemented a tri-diagonalization method to solve the two-stream equations of Meador and Weaver (1980), allowing for the radiative transfer to now be computed in a multi-layered atmosphere. This multi-layered 1D approach is known as a "plane-parallel" atmosphere, generally consisting of an order of ~ 100 of these layers (e.g. Baudino et al. 2017; Mollière et al. 2019). Of the treatments at the time that were successful at computing these types of atmospheres to within an accuracy of 1% (e.g. Lenoble 1985), this one-dimensional implementation proved to be much more computationally efficient, and its error of up to 10% was deemed appropriate for "most atmospheric applications" (Toon et al. 1989). In recent years, it has also become quite common for 1D retrieval codes to implement an analytic solution, which is discussed further and compared with the two-stream approximation in section 2.

Since planets are 3D objects (Newton 1726), the use of a 1D model is not without its faults. A drawback of 1D models is that only a dayside average, planetary average, or substellar temperature can be computed. This prevents latitude-dependent temperature calculations, which may have been important on the early Earth under the liquid equatorial belt hypothesis. This scenario suggests that Earth could have possibly existed as both a snowball and a temperate climate, dependent upon latitude (Charnay et al. 2013). This melted-equator snowball could have been possible due to the faster rotation of the early Earth weakening the Hadley cells — the winds that transfer heat from the equator to the poles — both cooling the poles and heating the equator (Charnay et al. 2020). This 1D approach also obscures the picture of heat transport from day to night side by winds.

Global Climate Models (GCMs) are a more advanced type of radiative transfer code. These models account for the "physical, biological, and chemical properties" of an atmosphere, including water cycles and carbon cycles (Shields 2019). GCMs are grid-codes,

dividing the spherical planet into a latitude and longitude grid, and computing the average physical properties within each cell. GCMs are even able to include ocean circulation, which functions as another method of heat transport to other regions of the planet, such as warm equatorial waters up toward the poles (Shields 2019).

A drawback to these models is the large number of input parameters that must be accounted for, all of which may be difficult to resolve through a more optically thick exoplanet atmosphere. These include the density and structure of the interior of the planet, the rate of rotation around its axis, the strength of magnetic fields, tidal effects from natural satellites, and both rate and composition of outgassing, just to name a few (Deeg and Belmonte 2018). Ocean currents can play a major role in climate, including here on Earth (e.g. Yin and Zhao 2021), and constraining the depth and amount of surface covered by these oceans on exoplanets may prove exceptionally difficult. On the other hand, 1D models use a simpler set of input parameters, focused on the luminosity of the host star and the semimajor axis of the planet’s orbit, as well as the chemical composition of the atmosphere to account for a greenhouse, to solve for the incoming radiative flux. The parameters necessary for 1D models and retrieval can be measured from both current and future observation (e.g. Birkmann et al. 2016; Herbort et al. 2020). While lacking the ability to solve for latitude-dependent temperatures and effects of winds and ocean currents that a GCM can, 1D models and their smaller number of inputs can still be used effectively to investigate the classical Habitable Zone (e.g. Kasting et al. 1993), which is the focus of this work and our future works.

2.2 The German Connection: *petitRADTRANS*

While several 1D, plane-parallel models exist, the publicly available *petitRADTRANS* (Pressure - Temperature Iterator and Spectral Emission and Transmission Calculator

for Planetary Atmospheres **R**adiative **T**ransfer) was chosen for this work.¹ For the purposes of this manuscript, we will refer to this version of *petitRADTRANS* as *petitRADTRANS 1.0*. Written by Mollière et al. (2019) at *Max-Planck-Institut für Astronomie* in Heidelberg, Germany, *petitRADTRANS* was designed for spectral characterization of exoplanets from *JWST* spectra. This program is widely accepted in the field of exoplanet astronomy, and is one of the front-running exoplanet retrieval programs where it has been implemented to propose a new method of planet characterization via their carbon to oxygen ratios (Molaverdikhani et al. 2019), to study the two Neptune-mass planets of a nearby binary system (Carleo et al. 2020), to investigate the effects of cyanide (CN) on super-Earth atmospheres (Zilinskas et al. 2020), and to — along with *POSEIDON* (MacDonald and Madhusudhan 2017) — classify the atmosphere of the only known transiting exoplanet within the *JWST* Continuous Viewing Zone (WASP-62b) (Alam et al. 2021), among others.

petitRADTRANS 1.0 is able to compute the thermal profile of an atmosphere from the input chemical abundances and equilibrium temperature. Mollière et al. (2019) implemented the Guillot temperature solution for this (see Guillot 2010; section 2.3) due to the heavy computational resources required to solve the full radiative transfer equations. Additionally, contrary to its namesake, *petitRADTRANS 1.0* was written with a focus on spectral calculations due to stellar radiation transferring through an atmosphere, not the thermal calculations of radiative transfer (Mollière et al. 2019). These calculations will, however, be implemented in future versions (see section 2.7).

petitRADTRANS 1.0 was benchmarked with *petitCODE*, a 1D plane-parallel radiative transfer modelling code by Mollière et al. (2015) exclusive to the Max Planck Institute in Heidelberg, which is discussed further in section 3.1.2. It has also successfully been used for test retrieval on synthetic *JWST* spectra of hot Jupiter exoplanet

¹Cerrillo wishes to note that it is by coincidence that *petitRADTRANS* is named after three adjectives that describe her.

TrES-4b (Mollière et al. 2019). *petitRADTRANS 1.0* functions similar to its predecessor *petitCODE*, using the same spectral data and correlated-k method for opacities of molecular species (described in sections 2.7 and 3.1.2); however, *petitCODE* is able to compute spectra, thermal structure, and chemical composition self-consistently, which are the retrievable parameters in *petitRADTRANS 1.0* (Mollière et al. 2019). One of the major upgrades in *petitRADTRANS 1.0* from its forerunner is that it comes packaged in a user-friendly Python wrapper with much of the processes computed in Python, as opposed to the Fortran implementation of *petitCODE*. This interface allows the novice user to evaluate transmission and emission spectra with few, user-friendly lines of code (Mollière et al. 2019). *petitRADTRANS* also benefits more experienced scientists by allowing for easy import of new opacity species to meet the needs of the research at hand by simply adding the correct files to a new folder, which are instead hard-coded into *petitCODE* and not designed in a way that can easily be altered by the end user.

2.3 Written in Black & White: The grey atmosphere method

Even though opacity can be calculated at each wavelength using spectral absorption lines or the correlated-k method (2.7,3.1.2), the implemented Guillot solution is a semi-grey approach. While a so-called "grey" atmosphere uses one average opacity across all wavelengths, a semi-grey model accounts for the average opacities over two separate ranges. Another simplified model is the picket-fence model (Chandrasekhar 1935; Mihalas et al. 1978), where opacity at certain wavelengths can take one of two opacities. While not technically a grey model itself, it is efficient for approximating a line-by-line approach in which all spectral line depths reach the same value (Parmentier and Guillot 2014). In the case of the Guillot solution and *petitRADTRANS 1.0*, this semi-grey covers opacities for the visible and infra-red portions of the spectrum, meaning that unlike a grey assumption, it is able to be used for irradiated atmospheres (Parmentier and Guillot 2014).

Not unlike the motivation behind the 1D model of Toon et al. (1989), Guillot (2010) derived an analytic solution to simplify the equations of radiative transfer, speeding computation time by circumventing the need to integrate the equations of radiative transfer to find the temperature at each layer of the atmosphere. The Guillot temperature solution is common in the field of exoplanet and stellar astronomy (e.g. Fortney et al. 2011; Heng et al. 2012; Seager et al. 2013; Diamond-Lowe et al. 2014; Koll and Abbot 2015; Heng and Lyons 2016; Lü et al. 2017; Kitzmann et al. 2018; Poser et al. 2019; Avila et al. 2021; Otegi et al. 2021 for a very condensed list). It is implemented in several benchmarked retrieval codes, such as *CHIMERA* (Line et al. 2013), *TauREx* (Waldmann et al. 2015), and *PYRAT BAY* (Cubillos and Blečić 2021).

Following the work of Chandrasekhar (1960) and Mihalas et al. (1978), Guillot (2010) chose to make an important assumption for their solution: the incoming and outgoing radiation do not have an overlap in their frequencies. This semi-grey approach uses an average opacity calculation κ across both the visible, κ_v , and thermal bands, κ_{th} . This choice dictates that their approach is valid in the regime where incoming stellar light is confined to visible frequencies, and outgoing thermal radiation is confined to infra-red frequencies.

The most fundamental quantity in radiative transfer is I_ν , the frequency-based specific intensity of a light ray through an atmosphere. It is this intensity that is attenuated by absorption and scattering, and strengthened by emission within an atmosphere. This intensity is related to other quantities of radiative transfer by three moments (Mihalas et al. 1978), given by

$$(J_\nu, H_\nu, K_\nu) \equiv \frac{1}{2} \int_{-1}^1 I_{\nu\mu}(1, \mu, \mu^2) d\mu, \quad (2.1)$$

which are used to calculate the mean intensity/energy of the beam (J_ν), the flux of radiation ($4\pi H_\nu$), and radiation pressure ($4\pi/cK_\nu$) (Guillot 2010). The subscripts ν

and μ denote the frequency of the light associated with that intensity and the angle from the normal at which the ray passes through the atmosphere, respectively. The value of μ relates to the angle θ from the normal through $\mu = \cos \theta$. In a plane-parallel atmosphere at equilibrium, the moments of radiative transfer were solved by Guillot (2010) to give

$$\frac{dH_\nu}{dm} = \kappa_\nu(J_\nu - B_\nu) \text{ and} \quad (2.2)$$

$$\frac{dK_\nu}{dm} = (\kappa_\nu + \sigma_\nu)H_\nu, \quad (2.3)$$

in which $dm = \rho dz$ is the column mass of the atmosphere through which the ray has travelled with density ρ and vertical height dz , B_ν is the frequency-dependent Planck function, and σ_ν is the frequency-dependent scattering coefficient, neglected by Guillot (2010).

The semi-grey opacities in *petitRADTRANS* are solved using the Rosseland mean for κ_{th} and the Planck mean for κ_ν . Due to the optical thickness of the greenhouse in the IR bands, the Rosseland mean is common implemented in this thick, diffusive regime (Nakamoto and Nakagawa 1994; Parmentier and Guillot 2014). Since the atmospheres of our study are much thinner in the visible than in the IR, and irradiated in the visible bands, the Planck mean’s common usage for an irradiated and optically thin gas motivated its use in this work (Malygin et al. 2014). While Guillot (2010) did not explicitly specify this usage, our choice to designate the mean opacity calculations in this way is consistent with existing semi-grey radiative transfer literature (e.g. Mihalas et al. 1978; Nakamoto and Nakagawa 1994; Parmentier and Guillot 2014; Parmentier et al. 2015). These opacity calculations are given in equations 2.4 & 2.5, respectively

(Nakamoto and Nakagawa 1994).

$$\frac{1}{\kappa_{\text{Ros}}} = \frac{\int_0^\infty \kappa_\nu^{-1} \frac{\partial B_\nu(T)}{\partial T} d\nu}{\int_0^\infty \frac{\partial B_\nu(T)}{\partial T} d\nu} \quad (2.4)$$

$$\kappa_{\text{Pla}} = \frac{\int_0^\infty \kappa_\nu B_\nu(T) d\nu}{\int_0^\infty B_\nu(T) d\nu} \quad (2.5)$$

The semi-grey approximation from Guillot (2010) assumes that the contribution of thermal emission in the visible is negligible, allowing Guillot (2010) to rewrite equation 2.2 as

$$\frac{dH_v}{dm} = \kappa_v J_v, \quad (2.6)$$

for the incoming visible light, which implies that the heat flux at the top of the atmosphere can be written as

$$H_v(0) = -\mu_* J_v(0), \quad (2.7)$$

in which μ_* is the average $\cos\theta$, and $= 1/\sqrt{3}$ for isotropic incoming radiation. $H_v(0)$ is negative as it represents the inward flux, defined as the negative direction by Guillot (2010). Given that $J_v \gg B_v$, this model also works well in the limit of optically thin atmospheres, where the mean incoming flux in the visible is comparatively much larger than the visible flux travelling out of the atmosphere. This semi-grey approximation also works best in the optically thin limit of $\tau_v \ll 1$ given that at deep depths in thick atmospheres, the thermal radiation will have a much larger flux contribution than the visible following attenuation of most if not all of the incoming visible radiation to reach such a depth (Guillot 2010).

For the thermal emission, Guillot (2010) followed the same semi-grey assumptions, finding that the source function at any given atmospheric layer can be calculated as

$$B = H \left[\frac{1}{f_{H\text{th}}} + \frac{\tau}{f_{K\text{th}}} \right] - H_{\text{v}}(0) \left[\frac{1}{f_{H\text{th}}} + \frac{\mu_{*}}{\gamma f_{K\text{th}}} + \left(\frac{\gamma}{\mu_{*}} - \frac{\mu_{*}}{\gamma f_{K\text{th}}} \right) e^{-\gamma\tau/\mu_{*}} \right], \quad (2.8)$$

where $H = \sigma T_{\text{int}}^4/4\pi$ is the imposed heat flux at the bottom of the atmosphere and, for isotropic radiation, $H_{\text{v}}(0) = -f\sigma T_{\text{irr}}^4/4\pi$ is the imposed heat flux at the top (Guillot 2010). In $H_{\text{v}}(0)$, an f value of $f = 1$ is used for the heat flux at the location which has the Sun directly at its zenith, and $f = 1/2$ and $f = 1/4$ are used for the dayside average flux and planetary average flux, respectively. With $\mu_{*} = 1/\sqrt{3}$ due to isotropy as previously stated, Guillot (2010) found that the solution to the temperature at each layer in the atmosphere can now be solved quite simply and efficiently using

$$T^4 = \frac{3T_{\text{int}}^4}{4} \left[\frac{2}{3} + \tau \right] + \frac{3T_{\text{irr}}^4}{4} f \left[\frac{2}{3} + \frac{1}{\gamma\sqrt{3}} + \left(\frac{\gamma}{\sqrt{3}} - \frac{1}{\gamma\sqrt{3}} \right) e^{-\gamma\tau\sqrt{3}} \right]. \quad (2.9)$$

In equation 2.9, $\gamma \equiv \kappa_{\text{v}}/\kappa_{\text{th}}$, and is the same averaged value throughout the atmosphere (Parmentier and Guillot 2014), while the optical depth $\tau = P\kappa_{\text{th}}/g$, where P is the pressure of that layer in $\text{dyn}\cdot\text{cm}^{-2}$ and g is the acceleration due to gravity in $\text{cm}\cdot\text{s}^{-2}$. Fortney et al. (2011) found that, in the cases of optical depths $\tau = 10^{-2} \rightarrow 100$, the mean derivation in the analytic solution of equation 2.9 from their self-consistent radiative transfer calculations was 1.4%.

In our work, we began using *petitRADTRANS 1.0* with the Guillot temperature solution to obtain equilibrium thermal profiles for the disequilibrium calculations of Pearce et al. (2022). We intended to compute thermal profiles based on equilibrium composition. This way, Pearce et al. (2022) could use the possible compositions of early Earth scenarios that are shown to have habitable surface temperatures to compute the rates of biomolecule production, narrowing down the constraints on atmospheric conditions on early Earth that lead to the formation of life under our faint young Sun.

2.4 Heidelberg, We’ve Had a Problem: Modifying the code

One can notice a problem for computing a final answer at equilibrium when looking at equations 2.9, 2.4, and 2.5. While the final temperature of equation 2.9 is dependent upon the thermal opacity (in τ) and visible opacity (in γ) at every layer, the opacities in equations 2.4 and 2.5 are dependent upon the temperature T (in the Planck function $B(T)$) at every layer. This motivated our first alteration to *petitRADTRANS 1.0*: an iterative solution must be implemented. This way, the input thermal profile can dictate the opacities which can dictate the new thermal profile which can dictate the opacities and so-on until convergence. For the purposes of this manuscript, we will be referring to this version of *petitRADTRANS* as *petitRADTRANS 1.5*. We used the chemistry and thermal profile data for Saturn’s largest moon Titan — an analogue to the reducing atmosphere suspected on early Earth (Hörst 2017) — from Yelle et al. (1997) as a benchmark for testing the program alterations. Along with its reducing power, Titan’s atmosphere also has the same thermal profile of modern Earth, possessing its own well-defined troposphere, stratosphere, mesosphere, and thermosphere (Hörst 2017 and references therein).

For this iterative treatment, we implemented a convergence criteria of $\Delta T = 1K$ for all layers with a pressure greater than the tropopause, set to the modern Earth tropopause pressure at 0.14 bar. We quickly discovered that in some cases, solving this way can cause an atmosphere’s thermal profile to "flip-flop" between being very hot and very cold. This was remedied by implementing

$$T_n = (0.95 \times T_{n-1}) + (0.05 \times T_{n(\text{computed})}), \quad (2.10)$$

in which the new thermal profile at iteration n was found using 95% of the previous solution, and 5% of the newly computed solution. This same method is applied to other radiative transfer codes to overcome this same hurdle, such as in *petitCODE* —

appropriately, the predecessor to *petitRADTRANS 1.5* (Mollière et al. 2015; Mollière et al. 2019).

Upon further inspection of the equations used, we also noted a subtle and easy-to-miss problem with the Planck mean opacity calculation in 2.5. The Planck mean opacity uses the Planck function at the temperature T of each layer in the atmosphere. Put simply, our visible opacity was calculated using the planet’s own radiation field. One may recall that Guillot (2010) assumed that the planet’s radiation field falls within the IR only, and we are also using a temperature regime where this would be the case. We realized that we must implement a two-temperature mean as Malygin et al. (2014) implemented for their protostellar gas disk models. They give this two-temperature mean to be

$$\kappa_{\text{Pla}} = \frac{\int_0^\infty \kappa_\nu(T_{\text{gas}})B_\nu(T_{\text{rad}})d\nu}{\int_0^\infty B_\nu(T_{\text{rad}})d\nu}, \quad (2.11)$$

where T_{gas} is the temperature at every layer of the atmosphere, of which the opacities κ_ν are dependent upon, and T_{rad} is the stellar effective temperature, of which the Planck function of the incoming visible light $B(T)$ is dependent upon. Prior to this implementation, the incoming visible light was not accounted for in the semi-grey opacities, and therefore ignored in the resulting Guillot temperature approximation of equation 2.9. This change resulted in an increase from the previous one-temperature solution to the new two-temperature mean (Fig. 2.1).

petitRADTRANS 1.5 is capable of modelling clouds using power law opacities or by specifying the particle size of condensed cloud species whose opacities are in the database (Mollière et al. 2019). Without its implementation of a self-consistent chemistry module at the time like the one found in *petitCODE* (see section 3.1.2), the necessary evaporating, condensing, and precipitating water cycle on Earth could not be modelled out-of-the-box. While we were able to justify a cloudless atmosphere (as with our later work, see section 3.4.1 for details), the important greenhouse effects of evaporated water

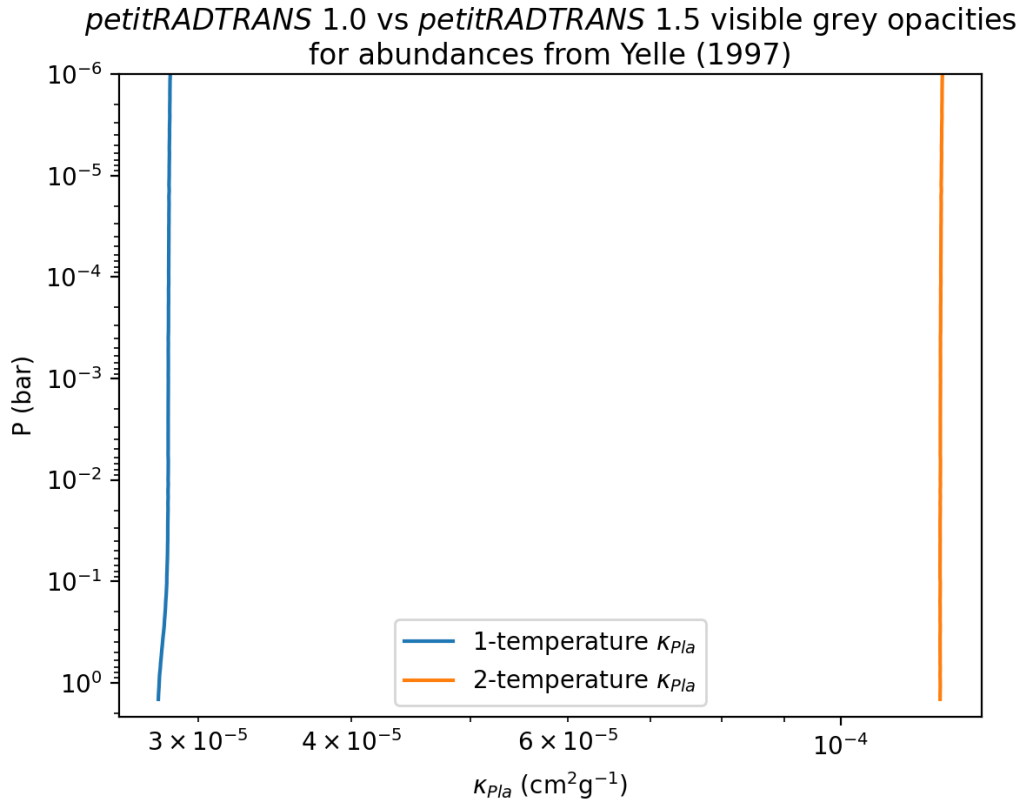


FIGURE 2.1: $\kappa_{\text{Pl},a}$ of our test Titan case using abundances from Yelle et al. (1997), the new two-temperature Planck mean from Malygin et al. (2014) for $T_{\text{rad}} = T_{\text{gas}}$, mimicking the old one-temperature treatment of *petitRADTRANS* 1.0 (blue), and for $T_{\text{rad}} = T_{\text{Sun}}$, the new treatment for our opacities in *petitRADTRANS* 1.5 (yellow). A clear order-of-magnitude increase in opacity from the one-temperature case is noted.

in the thermal profiles — and later the important water abundances for disequilibrium chemistry in Pearce et al. (2022) — needed to be accounted for.

To solve for this evaporation, Ben Pearce chose to implement what is known as the Arden Buck equation. This equation, shown in equation 2.12, was created by Buck (1981) and later modified by Buck (1996) as an analytic solution to calculate the saturation vapour pressure of moist air in the temperature range of -80 to 50°C . Equation 2.12 shows the saturation vapour pressure for $T > 0^\circ\text{C}$ in hPa using the modified Buck (1996) version. This analytic solution allows for swift computation, befitting the tandem use of

the analytic Guillot temperature solution.

$$P_s(T) = 6.1121 \exp\left(\left(18.678 - \frac{T}{234.5}\right)\left(\frac{T}{257.14 + T}\right)\right) \text{ hPa, for } T > 0^\circ\text{C}. \quad (2.12)$$

The mass fraction of water computed using equation 2.12 replaced the equivalent mass fraction abundance of N₂ in our atmospheres at every layer, which was chosen due to its distinct lack of absorption features, to keep the surface pressure constant and the chemical abundances normalized regardless of amount of water added. This new H₂O contributes to the overall greenhouse of Earth. We constrained the calculated water abundance using equation 2.12 to the troposphere, pressures greater than the tropopause, which allowed us to approximate both evaporation and Earth’s dry stratosphere — which only has ~1 ppm H₂O (Zahnle et al. 2020). To prevent a runaway greenhouse — in which a higher temperature will hold more water which will increase the temperature due to the strong thermal absorption by H₂O and so-on — we decreased the relative humidity for every °C of warming by a parameter $\beta = 6\%$ (Held and Soden 2000). This fits with the concept of vertical mixing, where relative humidity increases with height due to upwelling of evaporated water to the cooler tropopause layer, which creates the condensed cloud layer on modern Earth. This choice of β reduces surface relative humidity to ~80% on average (Held and Soden 2000). The resulting water abundances computed using this method and used in Pearce et al. (2022) are shown in Fig. 2.2.

Following these adjustments made to *petitRADTRANS*, the stellar parameters and molecular abundances, including the output self-consistent H₂O abundances, were fed into *petitCODE* by our collaborator Paul Mollière for our early Hadean reducing atmosphere (model A in Pearce et al. 2022; shown in Table 2.1 and Fig. 2.4). This final test before pushing forward with the simulations of Pearce et al. (2022), shown in Fig. 2.3, gave us confidence that our time-consuming modifications to *petitRADTRANS* were an acceptable substitute to the formal equations of radiative transfer.

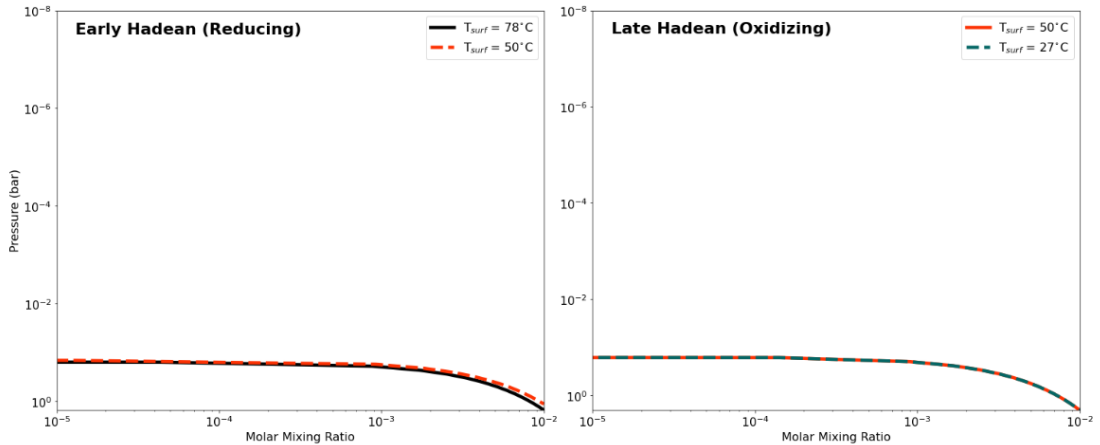


FIGURE 2.2: Tropospheric water vapour abundances for all 4 Hadean Earth models used by Pearce et al. (2022), computed using our addition of the Arden Buck equation (2.12) in *petitRADTRANS 1.5*. The values are given in molar mixing ratio, also known as mass fraction abundance. (Figure taken from Fig. S1, Pearce et al. 2022)

2.5 An Adapted Code Comes to Life: *petitRADTRANS* and origins

These alterations to *petitRADTRANS 1.5* were used to compute starting thermal profiles for four Hadean Earth atmospheres for Pearce et al. (2022). Of these models, two are oxidizing and two are reducing, with differences in surface pressure and abundances between them. The results for these atmospheres and their input parameters are shown in Fig. 2.4 and Table 2.1, respectively.

These PT profiles were then used by Pearce et al. (2022) to solve for disequilibrium chemistry and calculate biomolecule precursor yields using *ChemKM* (Molaverdikhani et al. 2019) and the chemical network module *CRAHCN-O* (Pearce et al. 2020; Pearce et al. 2022). While we’ve recognized that the opacity tables stop on the low pressure end at 10^{-6} bar and the nearest-neighbour opacity will be implemented when outside of the data set (see section 3.1.2; Mollière et al. 2015; Mollière et al. 2019), important photochemistry will occur at lower pressures, down to 10^{-8} bar (Pearce et al. 2022). At

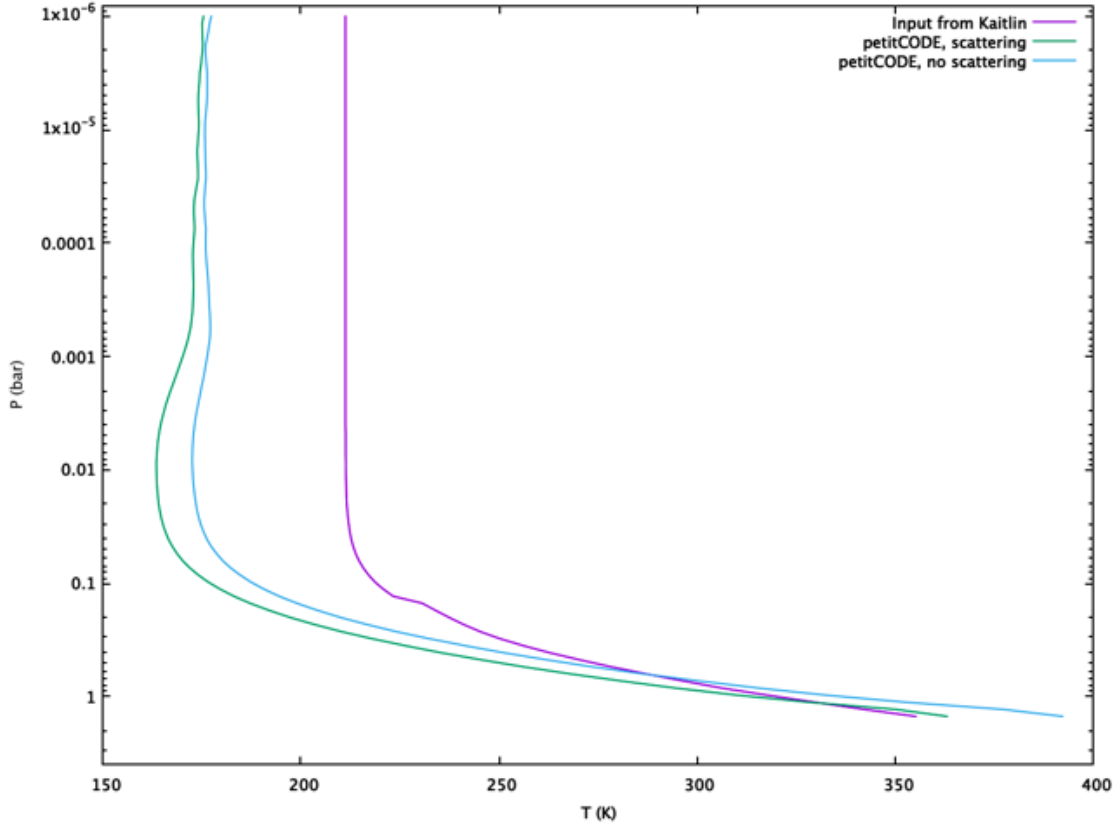


FIGURE 2.3: Comparison of *petitCODE* (green and blue) with our modified *petitRADTRANS 1.5* (magenta) using our self-consistent H₂O abundances for our early Hadean reducing atmosphere (model A in Pearce et al. 2022; shown in Table 2.1 and Fig. 2.4) by Paul Mollière.

such a low pressure, we found no difference in surface temperature for all models when computing the radiative transfer down to 10^{-8} bar for opacity data that ends at 10^{-6} bar.

With the use of our PT profiles in Fig. 2.4, Pearce et al. (2022) were able to determine that at 4.4 Ga, adenine could be maintained at peak concentration by atmospheric rainout in warm little ponds for over 100 My. They also noted that by 4.3 Ga, the buildup of methane (CH₄), the "critical feed molecule" for the formation of HCN, is terminated (Pearce et al. 2022). Their work further constrains the formation of life on Earth to be within ~200 My of the large Moon-forming impact (Pearce et al. 2022).

TABLE 2.1: Summary of the 4 Hadean Earth models we computed for Pearce et al. (2022) using our modified *petitRADTRANS*. (Table summarized from Table 2, Pearce et al. 2022)

| Model | Description | Date (Ga) | P_s (bar) | T_s ($^{\circ}\text{C}$) | Molar Composition |
|-------|----------------------------|-----------|-------------|------------------------------|--|
| A | Early Hadean (Reducing) | 4.4 | 1.5 | 78 | H ₂ : 90% N ₂ : 10% CH ₄ : 2 ppm H ₂ O: Fig. 2.2 |
| B | Late Hadean (Oxidizing) | 4.0 | 2 | 51 | CO ₂ : 90% N ₂ : 10% CH ₄ : 10 ppm H ₂ O: Fig. 2.2 |
| C | Early Hadean (Reducing) | 4.4 | 1.13 | 51 | H ₂ : 90% N ₂ : 10% CH ₄ : 1 ppm H ₂ O: Fig. 2.2 |
| D | Late Hadean (Oxidizing) | 4.0 | 2 | 27 | CO ₂ : 90% N ₂ : 10% CH ₄ : 1.5 ppm H ₂ O: Fig. 2.2 |

Our work with *petitRADTRANS 1.5* formed a part of the basis for the work by Pearce, Molaverdikhani, Pudritz, Henning, & Cerrillo (a.k.a. Pearce et al. 2022), who are the first authors to publish work that uses composition-dependent thermal profiles as part of the investigation into HCN yields on early Earth.

2.6 A Titan of an Obstacle: Limitations in the model

Before we get too ahead of ourselves and call the atmosphere of early Earth resolved, we must return to the Titan model used to benchmark the updated *petitRADTRANS 1.5*. While we implemented the Guillot solution to simulate atmospheres that fall well within the regime it is meant to function in (as discussed in section 2.3), the final temperature equation 2.9 has one covert limitation for modelling terrestrial atmospheres: the visible

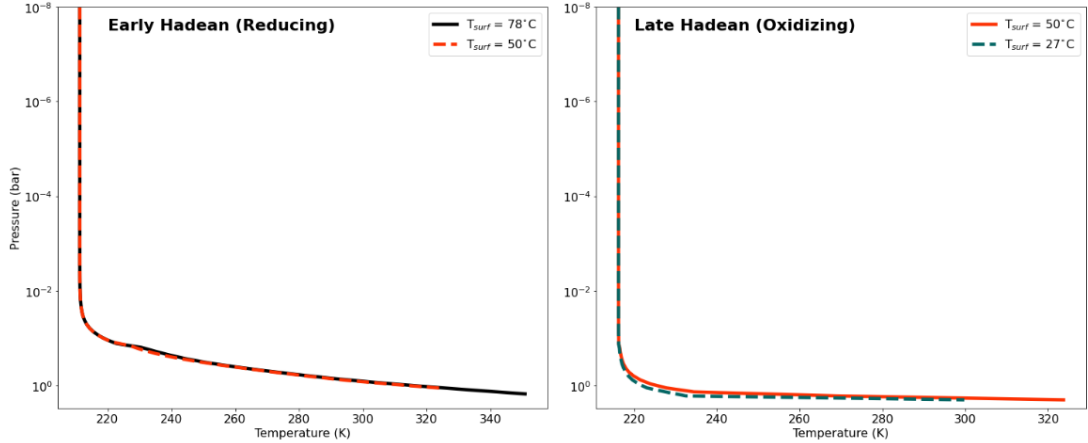


FIGURE 2.4: Pressure-Temperature profiles for all 4 Hadean Earth models used by Pearce et al. (2022), computed using our modified version of *petitRADTRANS*. (Figure taken from Fig. S2, Pearce et al. 2022)

opacity — due to its only contribution to the temperature calculation via the constant value $\gamma = \kappa_v / \kappa_{th}$ — must be the same at every layer of the atmosphere (Parmentier and Guillot 2014). This delayed realization created a significant setback in the work.

A limiting factor of this γ value is that there is no first-principles approach that can self-consistently include the effects that different atmospheric compositions can have (Mordasini 2020). In the case of the Guillot solution γ values used by Jin et al. (2014) (Table 2), it was necessary for them to manually adjust, by eye, the γ values for each case that gave a temperature in the isothermal zones ($\sim 100 - 1$ bar) of their models that was identical to the temperature of this isothermal zone found using a full numerical model (Mordasini 2020). This semi-grey approach is also unable to account for variations in temperature and pressure that would broaden absorption lines (Parmentier et al. 2015).

Using the molecular abundance data from Yelle et al. (1997), we tested our Titan model using the new *petitRADTRANS* containing the modified, iterative Guillot solution. Without the contribution of a visible absorber, our self-consistent PT profile was much too hot. This result is shown in Fig. 2.5. For certain optical depths, convection is also more efficient than radiation at cooling the lower layers of an atmosphere. In the

case of a semi-grey analytic solution, while it is possible to include convective regions, it is not possible to modify the radiative solution in the upper layers in accordance with the presence of the convective layers below (Parmentier et al. 2015). Due to the anti-greenhouse effect on Titan caused by scattering and absorption of incoming visible light (see 3.4.3), this was our first glimpse of how important the effects of a visible opacity will be in providing a net cooling the surface, especially in an analytic model.

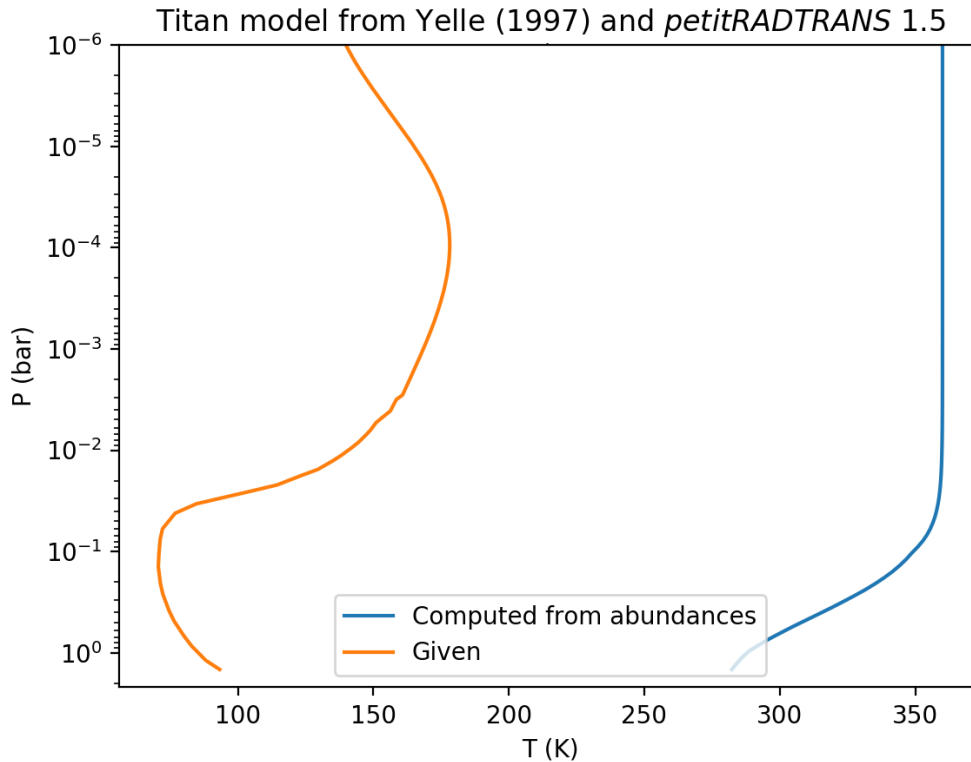


FIGURE 2.5: The thermal profile (blue) of Titan computed self-consistently in the iterative Guillot version of *petitRADTRANS* 1.5, using measured abundances from, and compared with the measured thermal profile (yellow) from, Yelle et al. (1997). Our self-consistent temperature (blue) is much higher than the measured (yellow) value.

The atmosphere of Titan, which is importantly the only known analogue to the early Earth’s, is ripe with visible light absorbers. The photochemical haze that envelops Titan

is so opaque across the visible wavelengths that it prevented the imaging cameras on-board Pioneer 11 and Voyagers 1&2 from seeing through to the surface (Hörst 2017). The early Earth is expected to have had a haze production rate for a highly reducing atmosphere of $10^3\times$ that of modern Titan, due to the $10^3\times$ greater UV flux from the faint young Sun at Earth compared to the UV flux of the modern Sun at Titan (Zahnle et al. 2020). Lacking the opacity species for the long-chain hydrocarbons that comprise Titan’s hazes, we attempted to simulate a visible opacity species on Titan by including O_3 abundances in the stratosphere only. The choice to use this available opacity species was due to ozone’s peak absorption cross-sections in the visible spectrum at both 575 and 603 nm Brion et al. 1998. This O_3 was constrained to replace 10% of the mass fraction of the inert N_2 between 10^{-1} and 10^{-4} bar, which are the order of magnitude constraints on the pressure values of Titan’s stratosphere (Hörst 2017).

Our result for the visible absorber experiment is shown in Fig. 2.6. Due to the nature of a constant visible opacity at every layer, the inclusion of a visible absorber not only marginally cooled the surface as we had hoped, it greatly cooled the stratosphere, which was unexpected. Due to a species attenuating the incoming stellar light via absorption, this increase in energy will heat the stratosphere (e.g. McKay et al. 1991). Our Titan models demonstrated that the Guillot solution, iterative or not, is not appropriate for terrestrial atmospheres.

In the case of Pearce et al. (2022), our Hadean Earth atmospheres (presented in table 2.1) lacked the presence of visible absorbers. This low κ_v reduced the effect of $\gamma = \kappa_v/\kappa_{th}$ in equation 2.9, allowing the homogeneous nature of a constant γ to be overlooked and the non-homogeneous thermal contribution in τ to dominate. It was also demonstrated in Fig. 2.3 that the results from the Guillot method closely matched those of a more complex self-consistent code.

Since Pearce et al. (2022) were interested in adjusting molecular abundances and

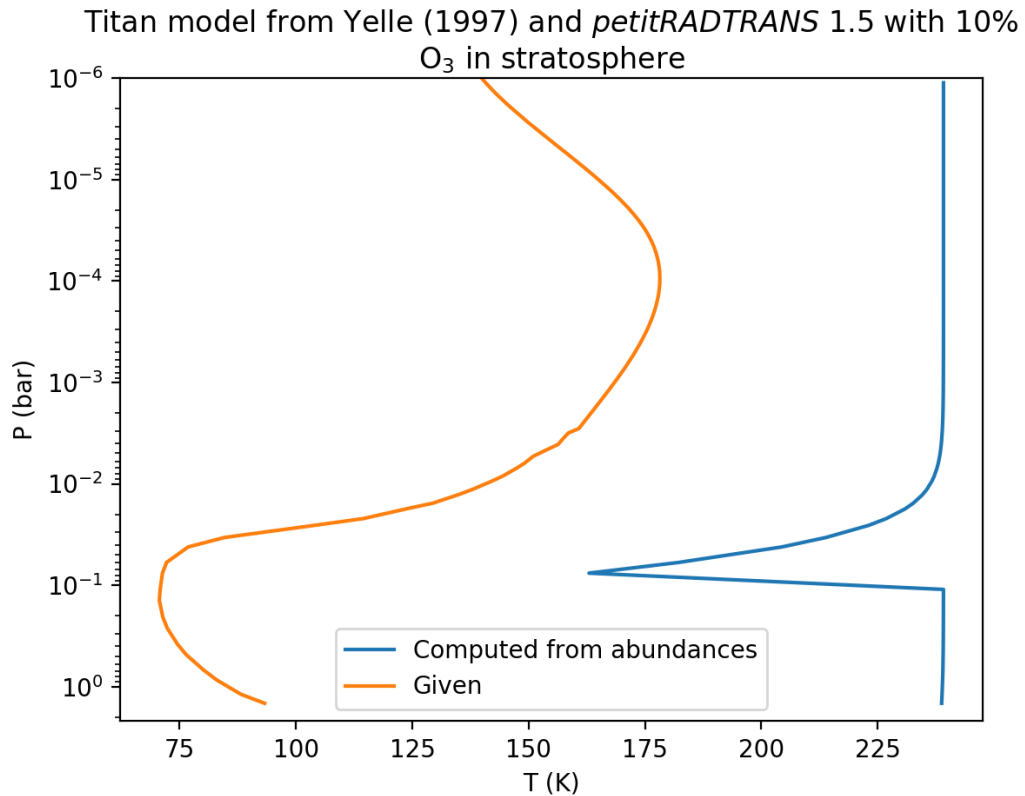


FIGURE 2.6: The thermal profile of Titan computed self-consistently in the iterative Guillot version of *petitRADTRANS* 1.5 (blue), using measured abundances from, and compared with the measured thermal profile (yellow) from, Yelle et al. (1997). Of the abundances, with 10% of the N₂ was replaced with O₃ in the stratosphere of the blue curve, bound by 10⁻¹ and 10⁻⁴ bar. This caused the stratosphere of our blue curve to unexpectedly cool.

surface pressures within constraints extrapolated from the geological record to find atmospheres that were both habitable and able to produce abundant biomolecules, it was very important for the changes in the greenhouse gas abundances to have the proper effects on the temperature. This also forced a limitation of the semi-grey Guillot model into view: The amount of trapped heat is less sensitive to the abundances of a real gas than to the those of a grey gas (Pierrehumbert 2010). With a grey gas greenhouse, little margin for error exists in greenhouse gas concentrations to maintain a habitable temperature (Pierrehumbert 2010). This tenuous balance is due to the lack of "windows" in

the spectrum through which the outgoing IR flux can pass. This highlights the requirement for a more complex handling of the opacities in the intended work. This further compelled the next approach, as outlined in section 2.7.

petitRADTRANS 1.5, from its development as a spectral retrieval code for gas giant exoplanets, also lacks a surface boundary condition that a modelling code needs for the terrestrial regime. This poses radiative transfer issues in an optically thin atmosphere. If an incoming ray of visible light reaches the 'surface', there is nothing there to absorb the remainder of the radiation. This poses an important issue when balancing the flux, and is discussed further in section 2.7. This lack of a surface boundary is also found in *petitCODE*, and discussed further in sections 2.7 and 3.1.3.

We, along with Pearce et al. (2022), also intended to investigate habitability and biomolecule production of transient early Earth atmospheres following the hypothesized Late Veneer impacts. The proposed Late Veneer atmosphere reached 90 bar of pressure at the surface, with a molar composition of 99% H₂. This type atmosphere is highly reducing with the ability to function as a very strong greenhouse Ramirez and Kaltenegger 2017, and warrants investigation for both habitability and biomolecule production. Even following our modifications, such as the new temperature computation of equation 2.10, we were unable to prevent such an atmosphere from "flip-flopping" greatly with each iteration, even trending toward total divergence as time went on. This post-impact atmosphere was able to be run to equilibrium using the more formal radiative transfer of *petitCODE*, whose results are presented in Chapter 3.

Upon recognizing our unfortunate luck with *petitRADTRANS 1.5* and our inability to circumvent its limitations in the computations that we required, we were forced back to the drawing board. While switching to a brand new code was imminent, we took a stab at requesting access to the Max Planck Institute Heidelberg's proprietary radiative transfer code — and elder sibling to our current — *petitCODE*. As luck would have

it, permission was granted to switch to the new radiative transfer code, conditionally (Henning 2020).

2.7 Port of Entry: Customs and integration

The intention since the creation of *petitRADTRANS 1.0* was to port in the self-consistent temperature calculations and chemistry calculations using the more formal equations of radiative transfer found in *petitCODE* (Mollière 2020). Integrated with the much more user friendly and more versatile interface of *petitRADTRANS*, this would ultimately generate a refined, publicly available version of *petitCODE*. This custom program will be a strong entry into the existing landscape of exoplanet retrieval and modelling codes. For the purposes of this manuscript, we will be referring to this two-stream version of *petitRADTRANS* as *petitRADTRANS 2.0*.

Enhancing existing work, this new publicly available *petitRADTRANS 2.0* would rival *ATMO* (Tremblin et al. 2015), an atmospheric modelling code owned and under-development by the University of Exeter’s Exoclimatology group. *ATMO* currently has a leg up on *petitCODE*’s chemistry computations by including the kinetic chemical network of Venot et al. (2012) and the ability to run 2D atmospheres to model the effects of latitudinal winds (Tremblin et al. 2015). This means that *ATMO* is capable of computing disequilibrium chemistry caused by interactions between the upper atmosphere and the incoming stellar flux, and *petitCODE 2.0* currently cannot. Still, some important drawbacks of *ATMO* are that it uses the computationally expensive line-by-line opacity method in its radiative transfer calculations for its limited opacity sources (H₂-H₂ collisional, H₂-He collisional, H₂O, CO, CO₂, CH₄, NH₃, K, Na, TiO, and VO), and, due to its design as a brown dwarf code, lacks a surface boundary condition (Tremblin et al. 2015). *ATMO* is also not available to download by anyone, anywhere, at any time like

petitRADTRANS 1.0 currently is (Mollière et al. 2019)², and *petitRADTRANS 2.0* will be.

Similarly, the modelling code *SCARLET* (Benneke 2015) implements a radiative-convective two-stream approximation as well as photochemistry, but focuses on the spectral implications of this chemistry and not the overall modelled thermal profile. Their chemical model is able to account for the chemical equilibrium in the deep atmosphere, convective quenching of chemical reactions in the mid-altitudes, and photochemistry in the upper atmosphere (Benneke 2015). While *SCARLET* also lacks a surface boundary condition, a concern is that it uses a proprietary method for speeding the line-by-line opacity calculations (Benneke 2015, Appendix). This method is unique to *SCARLET*, and is not well-verified or widely used like the correlated-k opacity method introduced by Goody et al. (1989).

These disadvantages are easily bested by the computationally efficient correlated-k opacity treatment of *petitRADTRANS 2.0* (explained later in this section and in section 3.1.2), and the ease of implementing new opacity species.³ At the time of its release in 2019, *petitRADTRANS 1.0* already contained the line opacity sources for CH₄, C₂H₂, CO, CO₂, H₂S, H₂, HCN, H₂O, K, Na, NH₃, O₃, OH, PH₃, TiO, VO, SiO, and FeH, with more included from the HITRAN database since (Mollière et al. 2019). *petitRADTRANS 2.0* also has the collision-induced opacities for H₂-H₂, H₂-He, N₂-N₂, O₂-O₂, N₂-O₂, and CO₂-CO₂, with Rayleigh scattering from H₂, He, H₂O, CO₂, O₂, N₂, CO, and CH₄. It can include the opacities for many species of crystalline and amorphous clouds across a wide range of atmospheric compositions, including H₂O, MgAl₂O₄, and MgSiO₃ (Mollière et al. 2019). Due to the hydrogen escape discussed previously, this comparably large amount of opacity species to choose from better suits applications

²Available via pip (instructions at <https://petitradtrans.readthedocs.io>) and <https://gitlab.com/mauricemolli/petitRADTRANS>

³A complete list of currently available opacity species is available in the code documentation at <https://petitradtrans.readthedocs.io>

to terrestrial atmospheres. Importantly for comparison with *ATMO* and *SCARLET*, while the newest published version of *petitRADTRANS 1.0* at the time of this writing has implemented the chemistry model *easyCHEM* (Mollière et al. 2017, Appendix A.2), the same as *petitCODE* (section 3.1.2), it is possible to implement the chemical model of our choosing as development of this new radiative-convective *petitRADTRANS 2.0* progresses.

Other retrieval codes, such as *TauREx* (Waldmann et al. 2015), are extremely modular and user-friendly, but lack the formal radiative transfer that we have ported to the new *petitRADTRANS 2.0*. *TauREx* was written for hot Jupiter retrieval, and performs retrieval similar to the original *petitRADTRANS 1.0*. Since its debut, it has also been successfully used for retrieval of sub-Jupiter mass planets, as has *petitRADTRANS 1.0* (Mollière et al. 2019; Al-Refaie et al. 2021). *TauREx* performs retrieval using either an input thermal profile, or an isothermal input profile. While it is possible for the end-user to include a formal radiative transfer code of their choosing, it does not come bundled with the framework (Waldmann et al. 2015; Al-Refaie et al. 2021), making our integrated updates to *petitRADTRANS 2.0* that much more enticing for the exoplanet research community.

With the presented evidence that an updated *petitRADTRANS 2.0* would fit well into the current selection of atmospheric retrieval and modelling codes and be worth the lengthy process to implement, debug, and benchmark this large change, that’s exactly what we did. While both *petitCODE* and *petitRADTRANS 1.0* were written by Paul Mollière, there were many noticeable differences at a first look through the subroutines, meaning that a direct copy-paste of the appropriate modules was not possible.⁴ What’s more, the current structure of *petitRADTRANS 1.0* had already undergone testing and debugging for many of the existing calculations (e.g. stellar spectrum, flux calculations, opacity treatments), and it was important that we port the radiative transfer calculations

⁴Study conducted by *the University of My Eyeballs*, 2021

over in a way that integrated them within the existing framework (Mollière 2021a). This led to the creation of a new `Fortran` module, of which *petitRADTRANS 1.0* has several, to compute the new radiative transfer codes. While nestled beneath a sleek and user-friendly `Python` wrapper, the `Fortran` modules are fast and better suited to heavy numerical computation. `Fortran` even outranks other swift languages like `C++` in spectral calculations (Elton 2015).

The radiative transfer of *petitCODE* follows the variable Eddington factor method, using a 2nd order Feautrier method on a 20-point Gaussian grid in g -space, the g bins of the correlated-k method, which is described and explained below (Mollière et al. 2015). This grid also accounts for 20 angles by which the rays can pass through the atmosphere. While differences were negligible, and *petitRADTRANS* was proven to replicate line-by-line opacities well using its smaller grid of g -bins, this is much more refined than the 16-point Gaussian grid in g -space of *petitRADTRANS 1.0*, which is also only able to account for 3 angles (Mollière et al. 2019). *petitCODE* also combines all opacities into one correlated-k table to solve for thermal structure. While treating the correlated-k opacities separately greatly decreases computation time for transmission spectra (Mollière et al. 2019), treating all opacity sources as one has since been implemented into the `mix_opa_tot` function of `radtrans.py` in *petitRADTRANS 1.0*. While already implemented in the new code, we now present a brief explanation of the correlated-k method for completeness.

The correlated-k method was first presented by Goody et al. (1989). This method was created to effectively account for pressure-broadening in inhomogeneously mixed atmospheres without sacrificing computation time to high-resolution line-by-line methods (Lacis and Oinas 1991). Prior to this, accurate modelling of absorption features was limited by how well the line depths and pressure-broadened line widths of an absorption spectrum could be resolved. The correlated-k method allows for the absorption coefficients to be sorted as a function of their recurrence, and sorted further into a distribution

of absorption coefficient probability. This method uses a function $h(k)$, in which similar values of absorption coefficient k_ν — written in the rest of this manuscript as the mass absorption coefficient kappa (κ_ν) — are grouped by similar values and summed. This function is constructed so that $h(k)dk$ gives the fraction of the frequencies $\Delta\nu$ that have absorption coefficients of values $k \rightarrow k + dk$ (Fu and Liou 1992; Kratz 1995). Now that the absorption coefficient exists as a smooth function of its frequency in the spectrum, this allows for a much lower resolution to be used without losing the narrow line cores at low pressures, greatly reducing computation time (Mollière 2017). With this method, the strength of absorption coefficients is generally expressed in terms of a cumulative frequency distribution (Lacis and Oinas 1991) called g -bins, getting their namesake from

$$g(k) = \int_0^k h(k')dk' \quad (2.13)$$

in which g is now a cumulative probability function. In the case of the g -bins, $g(0) = 0$ and $g(k \rightarrow \infty) = 1$ (Lacis and Oinas 1991; Fu and Liou 1992). Now, the absorption features of an atmosphere can be computed independently of the absorption coefficient order — the key that allows a lower resolution to be used (see Fig. 2.7). Since the correlated- k method already exists in *petitRADTRANS 1.0* and a port of this was not required, we will not wax further poetic about it in this manuscript (for more, see e.g. Lacis and Oinas 1991; Fu and Liou 1992; Kratz 1995). In the amalgamation of the old code with the new, it isn't the opacities that are of priority, but what the code does with them. The variable Eddington factor two-stream approximation solution to the equations of radiative transfer, as implemented in *petitCODE* and ported as the new modelling backbone for *petitRADTRANS 2.0*, is now summarized for further completeness.

The variable Eddington factor method is a method of solving the two-stream Eddington approximation. Recalling the moments of radiative transfer given in equation 2.1 for solving the Guillot (2010) method, the Eddington approximation is defined by the

relation

$$K_\nu = \frac{1}{3} J_\nu , \quad (2.14)$$

where, as before, J_ν is the mean intensity of the light ray, and K_ν is proportional to the radiation pressure (Rybicki and Lightman 1986).

The two-stream approximation assumes that the radiation field can be represented by one ray entering the atmosphere and one ray leaving, each at angle $\mu = \pm 1/\sqrt{3}$. In the case of *petitCODE*, the positive direction I^+ is the intensity of the ray leaving the atmosphere to space at angle $\mu = +1/\sqrt{3}$, and the negative direction I_- is the intensity of the ray travelling into the atmosphere from the stellar source at angle $\mu = -1/\sqrt{3}$. While this decision is arbitrary, it is common in the field (e.g. Pierrehumbert 2010). For our purposes, we can neglect the scattering of incoming stellar light, thereby neglecting the scattering cross-section σ_ν in our optically thin, terrestrial regime. This lack of scattering

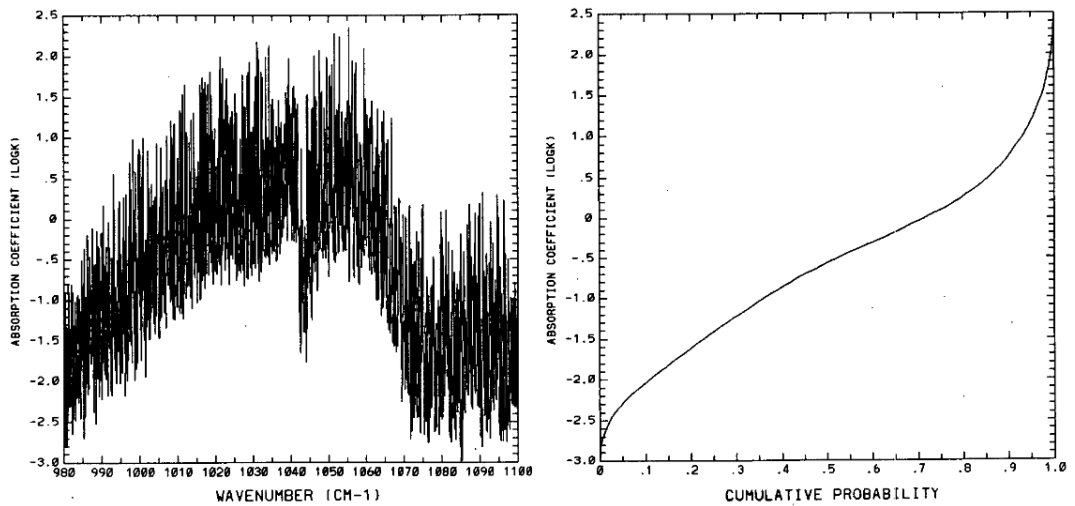


FIGURE 2.7: A plot of the absorption coefficient k vs. its cumulative probability (eqn. 2.13) for the $9.6\mu\text{m}$ absorption band of O_3 at a pressure of 25mb and a temperature of 220K. This is shown as a function of wavenumber (left) and g (eqn. 2.13) (right). This demonstrates the necessity for a much higher resolution and more computationally intensive method in a line-by-line opacity calculation than with the correlated- k method. (Plot from Fu and Liou 1992, Fig. 1)

also simplifies the source function S_ν by removing its dependence on I_ν (Rybicki and Lightman 1986). Elsewhere in the code, scattering is calculated via Rayleigh cross-section opacities attenuating the incoming stellar flux, and the albedo is then calculated self-consistently using the ratio of the attenuated bolometric stellar flux to the bolometric stellar flux at the top of the atmosphere.

Since scattering is being neglected, the change in specific intensity from a ray of specific intensity I_ν that passes along a path ds through a medium with an absorption coefficient α_ν

$$dI_\nu = -\alpha_\nu I_\nu ds. \quad (2.15)$$

Immediately, we are able to relate our opacity tables to this equation with the relation $\alpha_\nu = \rho\kappa_\nu$, in which ρ is the mass density and κ_ν , known as the mass absorption coefficient, is also known as opacity (Rybicki and Lightman 1986). Due to the local thermodynamic equilibrium assumed at every layer of a plane-parallel model, the source function in the code is only dependent upon the temperature, computed as the Planck function $S_\nu = B_\nu(T)$ (Mollière et al. 2015). Given when the medium is also emitting with an emission coefficient j_ν , equation 2.15 can also be written as

$$\frac{dI_\nu}{ds} = -\alpha_\nu I_\nu + j_\nu. \quad (2.16)$$

In the case of a plane-parallel atmosphere, the only quantity that can vary spacially is the vertical component dz . In the case of *petitCODE*, z was chosen to increase toward the upper layers of the atmosphere (Mollière et al. 2015). As the path ds through the atmosphere is related to the path and the angle from the normal by $dz/\cos\theta$, recalling from section 2.3 that $\mu \equiv \cos\theta$. We also know that the source function is defined by $S_\nu \equiv j_\nu/\alpha_\nu$ (Rybicki and Lightman 1986). Importantly, since the source of emission from our atmosphere is the temperature-dependent source function $S_\nu = B_\nu(T)$ the change

of I_ν as a function of path length from equation 2.16 is now written as

$$\mu \frac{dI_\nu}{dz} = -\alpha_\nu(I_\nu - B_\nu(T)), \quad (2.17)$$

as shown in Mollière et al. (2015) (Appendix C).

By integrating equation 2.17 over all solid angles for both the upward facing hemisphere and the downward, and applying the results to our Eddington moment definitions from equation 2.1, we find that our new Eddington moments are now

$$J_\nu = \frac{1}{2}(I_\nu^+ + I_\nu^-) \quad (2.18)$$

$$H_\nu = \frac{1}{2\sqrt{3}}(I_\nu^+ - I_\nu^-) \quad (2.19)$$

$$K_\nu = \frac{1}{6}(I_\nu^+ + I_\nu^-) \equiv \frac{1}{3}J_\nu \text{ in the Eddington limit.} \quad (2.20)$$

By following the definition of the Eddington moments in equation 2.1, integrating equation 2.17 over all solid angles, and multiplying in μ to equation 2.17 and integrating over the solid angle gives, from Mollière (2017),

$$\frac{dH_\nu}{dz} = -\alpha_\nu(J_\nu - B_\nu(T)), \text{ and} \quad (2.21)$$

$$\frac{dK_\nu}{dz} = -\alpha_\nu H_\nu, \quad (2.22)$$

respectively.

Using the optical depth definition in a medium with no scattering, $d\tau_\nu = -\rho\kappa_\nu dz$, and the gravitational acceleration g of the planet, Mollière (2017) used the hydrostatic balance condition of an equilibrium atmosphere to convert this into a pressure-dependent

quantity, with

$$d\tau_\nu = \frac{\kappa_\nu}{g} dP. \quad (2.23)$$

This is a very important step, since in a 1D plane-parallel model such as *petitCODE* and *petitRADTRANS 1.0*, pressure is the only variable that defines the atmosphere’s physical structure during the radiative transfer calculations. This also echoes the Guillot (2010) temperature equation (2.9), in which $\tau = P\kappa_{\text{th}}/g$ is the only parameter [in a homogeneously mixed atmosphere] that varies by layer, each of which are defined by their pressure.

Since this code solves for radiative-convective equilibrium, the incoming and outgoing fluxes must be balanced, and therefore the same at each pressure. This means that through every layer of pressure P , in accordance with Mollière (2017),

$$\frac{dH_{total}}{dP} = 0. \quad (2.24)$$

For a two-stream case, this H_{total} must be a combination of the planetary flux and the stellar flux, given by Mollière (2017) as

$$H_{total} = H_* + H_{planet} = \frac{\sigma_{\text{SB}} T_{int}^4}{4\pi}, \quad (2.25)$$

wherein $\sigma_{\text{SB}} T_{int}^4$ \equiv the total flux generated by the planet as a blackbody emitting at its internal temperature T_{int} . Mollière (2017) then rearranged equation 2.25 to find that the planetary flux at a layer with pressure P is

$$H_{planet}(P) = \frac{\sigma_{\text{SB}} T_{int}^4}{4\pi} - H_*(P). \quad (2.26)$$

This holds due to the attenuation of H_* at every layer through absorption, as is shown in equation 2.21. Since, in the case of *petitCODE*, the negative direction is downward, this H_* will be a negative value. Importantly, equation 2.26 shows us that, in thermodynamic

equilibrium, the flux leaving the planet at every atmospheric layer is dependent upon the sum of the internal flux from the planet itself and the downward flux of stellar light at that layer. If this were not the case, and the outgoing flux was smaller, the planet being simulated would enter a runaway greenhouse regime (Pierrehumbert 2010).

Now — the moment we’ve been waiting for — it is time to calculate the temperature at each layer in the atmosphere. Before we can, we must first define an Eddington factor $f_{K\nu} = K_\nu/J_\nu$ (Mollière 2017). The Eddington approximation is so-called because it begins with an approximate assumption: that $f_K = 1/3$ for both an isometric and collimated radiation field, just as in section 2.3 (Guillot 2010). The reason this factor is considered variable is because it is solved through iteration (Mollière 2017). Recalling the relation in equation 2.14 that defines the Eddington approximation, relating this to the starting assumption for f_K in the isometric radiation field regime, and using our Eddington factor definition $f_{K\nu} = K_\nu/J_\nu$, Mollière (2017) then showed that the frequency-independent variable Eddington factor can be solved using

$$f_K = \frac{\int_0^\infty f_\nu J_\nu d\nu}{\int_0^\infty J_\nu d\nu}. \quad (2.27)$$

Following all of these derivations, Mollière (2017) combined them into equation 2.22, thus giving the pressure-dependence of the mean intensity to be

$$\frac{d}{dP}(f_K J) = \frac{1}{g} \kappa_H H, \quad (2.28)$$

wherein, much like the Planck function weighted opacity from equation 2.5, κ_H is the mean flux-averaged opacity. The values of $f(P)$, $\kappa_H(P)$, and $H_{planet}(P)$ are then used to integrate equation 2.28 from the top of the atmosphere at $P = 0$ down to the desired pressure P to find J (Mollière 2017). This J is then used to evaluate

$$\kappa_{\text{Pla}} \frac{\sigma_{\text{SB}}}{\pi} T^4 - \kappa_J J - \int_0^\infty \kappa_\nu J_\nu^* d\nu = 0. \quad (2.29)$$

In this equation, as with κ_{Pla} and κ_H , the value of κ_J is the mean J -averaged opacity, with J being the mean intensity of the outgoing planetary radiation field, and J^* the mean intensity of the stellar incoming radiation field at each layer (Mollière 2017).

One with a keen eye might look at this final solution and notice that we still aren't finished. This may even look exactly like a situation we've come across before. In using equation 2.29 to solve for the temperature, we must first know the temperature to have a value for κ_{Pla} . How could we have solved all of that radiative transfer to be implemented into *petitRADTRANS 2.0*, and still wound up at the reason we began altering the code in the first place? Luckily, in a similar vein to the Guillot temperature solution (2.9), we can solve this iteratively using

$$T = \left[\frac{\pi}{\sigma_{\text{SB}} \kappa_{\text{Pla}}(T_{\text{old}})} \left(\kappa_J J + \int_0^\infty \kappa_\nu J_\nu^* d\nu \right) \right]^{1/4}, \quad (2.30)$$

or, if that wasn't an impressive enough recovery from another sticky situation, *petitCODE* — and by extension, the newest iteration of *petitRADTRANS 2.0* — skips the iterative equation 2.30 and solves equation 2.29 directly using the `zbrent` root finding algorithm from Press et al. (1992) instead (Mollière 2017).

The newest port of *petitRADTRANS 2.0*, like *petitCODE*, also implements the Schwarzschild criterion in order to check if a layer is convective. When a layer is found by the code to be more efficient at losing heat via convection than radiation, an adiabatic temperature gradient is used in the temperature calculations at that layer instead (Mollière et al. 2015). At each layer i , the radiative temperature gradient

$$\nabla_{\text{rad}} = \left(\frac{T_i - T_{i-1}}{P_i - P_{i-1}} \right) \cdot \left(\frac{P_i + P_{i-1}}{T_i + T_{i-1}} \right) \quad (2.31)$$

is compared with the adiabatic temperature gradient $\nabla_{\text{ad}} = (\Gamma_2 - 1)/\Gamma_2$ for which

$$\Gamma_2 = \left[1 - \frac{P}{c_P} \frac{\chi_T}{\chi_\rho} \right]^{-1} \quad (2.32)$$

in which P is the pressure at that layer, T is the temperature at that layer, ρ is the density of the atmosphere at that layer, c_P is the specific heat capacity, $\chi_T = (\partial \log P / \partial \log T)_\rho$ and $\chi_\rho = (\partial \log P / \partial \log \rho)_T$ (Mollière et al. 2015). In the event that $\nabla_{\text{rad}} > \nabla_{\text{ad}}$,

$$T_i = T_{i-1} \cdot \frac{P_{i-1} + P_i(2\Gamma_2 - 1)}{P_i + P_{i-1}(2\Gamma_2 - 1)} \quad (2.33)$$

will become the new temperature T at this layer i . Specifically, *petitCODE* will only allow two layers to become convective at a time, similar to the work in Marley et al. (1996). This is to prevent a case where one layer's $\nabla_{\text{rad}} \approx \nabla_{\text{ad}}$, repeatedly turning convection on and off in this layer and preventing convergence, or a case where too many layers become convective at once, not allowing the thermal profile of the radiative region to adapt to the change in temperature gradient beneath it (Mollière et al. 2015).

petitRADTRANS 1.0 and *petitCODE* alike both lack a surface boundary condition. Considering that they were built to investigate the properties of gas giants, which lack a solid core and reach very high optical depths, this should come as little surprise (see e.g. Debras and Chabrier 2019). For the terrestrial regime, however, the inclusion of a surface boundary condition becomes very important for accurately computing the radiative transfer. For our Hadean Earth models, we expect to be studying a world that is primarily covered by liquid water oceans, with less than 12.8% of the land surface area on modern Earth (Pearce et al. 2017). When a condensed reservoir exists on the surface of a terrestrial planet, such as Earth's water oceans and Titan's methane oceans (Hörst 2017), these oceans can absorb the incoming stellar radiation, acting as a sink source for heat. Whether this leads to a runaway greenhouse or not depends on the greenhouse gas concentrations and their contribution to the thermal optical depth (Pierrehumbert

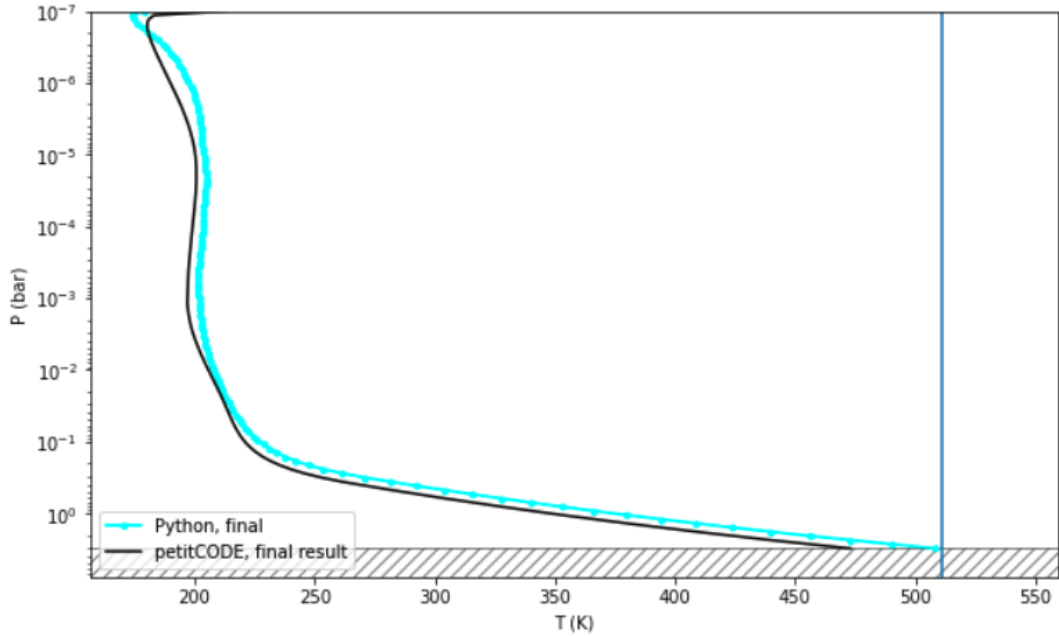


FIGURE 2.8: The thermal profile of the Vesta 2 impactor case of Zahnle et al. (2020) (see Chapter 3) computed self-consistently in the newly ported version of *petitRADTRANS 2.0* (cyan), compared with the surface-less *petitCODE* (black). The vertical line shows the new surface temperature value from *petitRADTRANS 2.0*. It shows that this new ground interaction of the incoming stellar light must increase the surface temperature to balance the incoming and outgoing fluxes.

2010).

This surface boundary condition has been implemented into the new *petitRADTRANS 2.0* by forcing the bottom-most layer of the atmosphere — i.e. the new ‘surface’ — to adopt a temperature that balances the incoming and outgoing flux. This new boundary condition is demonstrated in a preliminary test of the newest code in Fig. 2.8. This Vesta 2 model (see Chapter 3) is optically thin enough for 26.3% of the incoming stellar light to avoid scattering and absorption within the atmosphere and reach the surface, and optically thick enough to have met convergence criteria under the surface-less *petitCODE* described in section 3.1.2). Fig. 2.8 shows that this model has an increased surface temperature now that the surface condition is factored into the flux balance.

There are also plans to implement a latent-heat solution, accounting for the evaporative water pulling heat from the surface and releasing it through radiation as it condenses at the tropopause.

This new version of *petitRADTRANS 2.0*, currently still under development, has been tested against a modern Earth atmosphere under a modern Sun featuring the new surface boundary condition and two-stream equations by Paul Mollière. These results are presented in Fig. 2.9. Due to the current lack of latent heat release, the temperature at the surface boundary condition is too high. The layer above, however, has a temperature $T = 289.42$ K at a pressure of $P = 1.0$ bar, very comparable to the average Earth surface temperature of $T_{surf} = 288$ K at $P = 1.01$ bar. The tropopause with the new two-stream equations was found at $P = 0.04$ bar, close to both the modern Earth’s $P = 0.14$ bar tropopause and the expected $P \approx 0.1$ bar for a terrestrial planet (Catling and Kasting 2017). Due to the current lack of self-consistent chemistry, the $\gamma = c_P/c_V$ value was adjusted, based on the $\gamma \approx 1.3$ for moist air on Earth, until the stratosphere matched closely with the expected, measured profile (Mollière 2021b).

For this port, we have developed an advanced, 1D, forward model for exoplanet retrieval and modelling, as is common in the field (e.g. Waldmann et al. 2015; Mollière et al. 2019; Cubillos and Bleicic 2021), where assumptions are made about the atmosphere, then adjusted until equilibrium is reached. While our new way of computing PT profiles has been implemented, which is the focus of our work, it does retain some of its heritage; *petitRADTRANS 2.0*, as well as the older *petitCODE*, require an initial guess at the thermal profile to begin. Even though it is possible to implement an isothermal atmosphere at a reasonable temperature (such as T_{eq}), our starting thermal profiles are computed by the assumed-discarded Guillot temperature solution (equation 2.9), allowing the thermal profile to start with realistic values for that atmosphere. This thermal profile is then iterated until a radiatively-balanced atmosphere with an equilibrium chemical composition is reached.

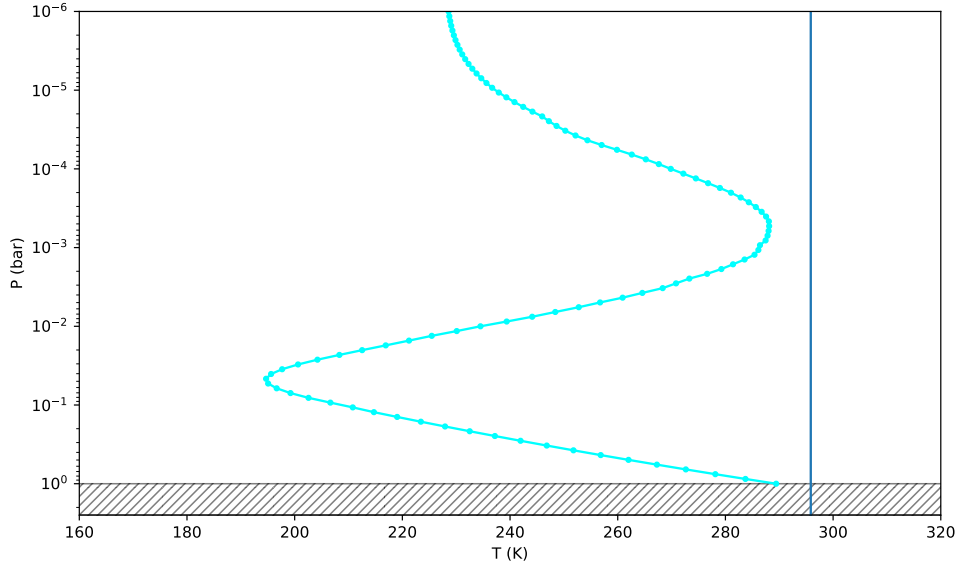


FIGURE 2.9: A modern Earth PT profile computed with the newest version of *petitRADTRANS 2.0* by Paul Mollière. The new surface temperature (vertical, dark blue line) does not account for latent heat release via water evaporation. The layer above has a temperature $T = 289.42$ K, very comparable to the average Earth surface temperature of $T_{surf} = 288$ K. Due to the current lack of a self-consistent chemistry code, the value of $\gamma = c_P/c_V$ was adjusted by eye based on the modern Earth’s moist γ until the calculated and observed PT profiles matched in their stratospheres (see section 3.1.2) (Mollière 2021b).

2.8 Time Wars: Episode IV – A new code

Prior to writing this manuscript, the newest and most advanced version of *petitRADTRANS 2.0* was in the process of having its new radiative transfer and boundary conditions implemented. At the time of writing this manuscript, *petitRADTRANS 2.0* is weeks from completion. The radiative transfer and surface boundary conditions are implemented, and are in need of benchmarking against other codes, such as the already benchmarked *petitCODE*, and the external *easyCHEM* equilibrium chemistry module is able to be used, albeit slowly. The new surface boundary condition, however, will allow for testing against terrestrial atmospheres with known compositions and thermal

profiles, such as Venus, Mars, and, finally, Titan.

As stated in section 2.6, using the previous iteration of *petitRADTRANS 1.5* did not allow for computations of a thick, post-impact Hadean atmosphere. The large impact event of the Late Veneer Hypothesis would have provided Earth with a highly reducing atmosphere. This post-impact chemistry would not only prevent a snowball Earth via its powerful greenhouse (Ramirez and Kaltenegger 2017), it would also provide the proper environment in which biomolecules can form (e.g. Miller and Urey 1959; Zahnle et al. 2020; Pearce et al. 2022). For this early Earth inquiry, the delayed *petitRADTRANS 2.0* will be used to re-create the work prior to publishing. In the interim, *petitCODE* was used in its place. The results of this investigation are presented in Chapter 3.

Chapter 3

The Habitability Of An Impacted, Young Earth

It has long been understood that early in Earth's formation history, ~3-4 Ga (billion years ago), the Sun would have been ~20-30% less luminous than today (Charnay et al. 2020). It has been found that, through stellar evolution, newly formed main sequence stars increase in luminosity as they age, requiring different chemistry conditions in Earth's atmosphere for a liquid water surface (e.g. Sagan and Mullen 1972; Newman and Rood 1977). This is a troubling predicament, as a young Earth with a modern Earth atmosphere would have been outside of the Sun's habitability zone, frozen like a snowball, until 2 Ga (Sagan and Mullen 1972); however, there remains direct evidence of microfossils by 3.4 Ga, and ^{13}C isotopic carbon within the range of reduced carbon compositions created by photosynthetic bacteria (Pearce et al. 2018; Rosing 1999). This implies that Earth's chemistry must have been very different from the atmosphere we have today, and that certain processes on the early Earth allowed life to begin.

The earliest time period in Earth's history is known as the Hadean eon, and began at Earth's formation in the disk. As ancient rocks would not be well preserved, it is difficult to determine events and conditions on the very young Earth, and to separate it into distinct eons; however, the Hadean eon is generally considered to have lasted until

the late heavy bombardment, up to ~3.8 Ga, the date at which the oldest well-preserved sedimentary rocks found thus far are considered to be part of the following eon: the Archean (Sleep 2010).

Zircon minerals found on Earth date back to as early as 4.37 Ga (Harrison et al. 2005). They are able to be dated accurately using Uranium-Lead (U-Pb) ages, from the well studied half-life and decay products on Uranium, reliably to ages as old as 4.404 ± 0.008 Ga (Wilde et al. 2001). It is also difficult to age zircons older than this, as the early Earth was still cooling and recycling its rock into magma frequently (Pearce et al. 2018).

Zircons are silicate minerals that preserve different isotopes of oxygen well. Heavier isotopes of oxygen, such as ^{18}O , form stronger bonds in minerals than lighter isotopes such as ^{16}O , preferentially partitioning this oxygen into these zircons (Bindeman 2008). As a higher percentage of heavy oxygen isotopes have been found in zircons dating to 3.91-4.40 Ga, this is evidence that the parent rock of the magma in which the zircons formed was in prolonged contact with low temperature H_2O , pointing to a consistent presence of liquid surface water throughout the Hadean eon (Pearce et al. 2018).

"Oxidized" and "reduced" refer to the ratio of H atoms to O, N, and other atomic species that would be attached to a carbon "scaffold" in a molecule. A highly reduced atmosphere would be one rich in CH_4 , while a CO_2 rich atmosphere would be the most oxidized. Based on early experiments by Miller and Urey (1959), the biomolecules required for life to form require a highly reduced atmosphere, rich in non-oxidizing molecules, but geological evidence from inside of Earth's mantle suggest that Earth has always been oxidized (Zahnle et al. 2020). A substantial amount of reduced biological precursor molecules, such as hydrogen cyanide (HCN), cyanamide (H_2NCN), cyanoacetylene (HC -CCN), cyanogen (NCCN), ammonia (NH_3), and cyanic acid (HCNO), would need to be

present for RNA to polymerize and form (Benner et al. 2020; Pearce et al. 2022). Photodissociation of reduced molecules, such as NH_3 and CH_4 , would oxidize an atmosphere over time as Jeans escape allows the resulting H_2 to escape and be lost to space due to its comparatively low mass; this would also leave an atmosphere more oxidized than the emitted gases supplying it below (Benner et al. 2020).

As early Earth would have been emitting mostly oxidizing CO_2 in the form of volcanic outgassing, a large impact event or series of events would generate a transient reducing atmosphere that would have lasted an order of millions of years (Pearce et al. 2018; Pearce et al. 2022; Zahnle et al. 2020). A massive, iron (Fe) rich impactor event would be able to mix its melted core with Earth’s vaporized oceans, and through the reaction $\text{Fe} + \text{H}_2\text{O} \rightarrow \text{FeO} + \text{H}_2$, create a transient reducing atmosphere with high pressure and a long cooling time. An impact object with a mass of 10^{24} g, about that of the dwarf planet Ceres, would have enough power to vaporize eight oceans worth of water (Zahnle et al. 2020). The probability of such an event is most evident in the Earth’s veneer, coming from a time period known as the Late Veneer. The veneer, or thin covering, of Earth is that of iron-loving (siderophile) elements. These siderophile elements would have differentiated to Earth’s core during early formation, before the core differentiated itself from the mantle, which occurred after the hypothesized giant impact that would have formed the Moon (Benner et al. 2020); however, there exists a 20km deep layer on Earth’s surface of these elements that must have been delivered later by a large impactor or series of smaller impactors with insufficient energy to penetrate to the core, instead vaporizing the oceans and mixing their siderophile elements over Earth’s molten surface (Zahnle et al. 2020).

While it has been previously suggested that comets may provide the necessary reduced organic materials for biomolecules (e.g. Pearce et al. 2017), and their approach velocity is great enough compared to Earth’s escape velocity that Earth’s gravitational pull would have little effect on their impact probability (Sleep 2010), it is now understood that a

large impact event or series of large impact events are necessary for a reduced chemistry environment capable of sustaining the consistent supply of building block chemicals necessary for biomolecule production — and ultimately RNA — over long periods of time (Pearce et al. 2022).

In this chapter, we examine the thermal structure of post-impact atmospheres from the equilibrium chemistry computed by Zahnle et al. (2020). The pressure-temperature profiles for these atmospheres have not yet been calculated self-consistently using the equilibrium chemistry of the transient reducing atmospheres. It’s important to note that reducing atmospheres rich in H_2 are very efficient at trapping heat: a hydrogen dominant atmosphere may push the modern Sun’s habitable zone out from 1.2 AU to 1.7 AU, past the orbit of Mars (Catling and Kasting 2017). It’s important to investigate self-consistently if an atmosphere is too efficient at trapping heat, because it may not allow for the wet-dry cycle of liquid water on the surface that is necessary for RNA to form (Pearce et al. 2017; Pearce et al. 2022).

3.1 Methods

3.1.1 Models

Zahnle et al. (2020) investigated the atmosphere of early Earth due to impactors during the Late Veneer period. They compared resulting post-impact atmospheric chemistry for 6 classes of impactors. The largest was the Max HSE impactor, which would have delivered all of the Earth’s siderophile elements to its veneer at once. The smallest impactor was the South Pole-Aitken, with a mass of the impactor that would have generated the largest preserved impact basin on the Moon. In the middle, the Pretty Big impactors would have provided the minimum veneer, under the conditions where most of the veneer came from the Moon forming impact itself (e.g. Newsom and Ross Taylor 1989). These impact events were further divided both by the amount of CO_2 in

the pre-impact atmosphere, and by the mineral buffers whose principal reactions with the atmosphere will influence the amount of oxygen available for the equilibrium chemistry to form from. These models are laid out in Table 3.1. See Zahnle et al. (2020) for further details on these equilibrium chemistry computations.

Zahnle et al. (2020) estimated surface temperature conditions for the computed equilibrium chemistry using

$$\begin{aligned} T_{surf} &\approx \left(\frac{(1-A)SF_{\odot}}{8\sigma_B}\right)^{0.25} \left(\frac{p_{surf}}{p_{tr}}\right)^{(\gamma-1)/\gamma} \\ &= 180\left(\frac{p_{surf}}{0.1bar}\right)^{0.13} K, \end{aligned} \quad (3.1)$$

and assumed that the troposphere behaved convectively with the thermal profile of a moist adiabat with the tropopause at skin temperature. The use of an adiabatic temperature gradient neglects any heat transfer from a rising convective parcel of air to its surroundings. The tropopause p_{tr} was assumed to be at 0.1 bar, as expected in thick atmospheres (Zahnle et al. 2020). This minimum occurs due to the square root dependence of pressure with opacity, giving similar scaling to all atmospheres of this type; however, this 0.1 bar stratosphere may not exist in atmospheres lacking a stratospheric visible absorber (Catling and Kasting 2017). As for the remaining variables, $A = 0.3$ is the Bond albedo of modern Earth, p_{surf} is the surface pressure in bars, γ is the specific heat ratio, and $\sigma_B = 5.67 \times 10^{-5}$ is the Stefan-Boltzmann constant in $\text{erg cm}^{-2} \text{s}^{-1} \text{K}^{-4}$.

In Eq. 3.1, $S = 0.72$, scaling the solar constant, $F_{\odot} = 1.36 \times 10^6 \text{erg cm}^{-2} \text{s}^{-1}$, to 72% of the modern Sun. This model assumed that the ~6 bar atmosphere, Vesta 1 from Table 3.1, has a surface temperature of $T_{surf} \sim 320K$ (Zahnle et al. 2020). Zahnle et al. (2020) also noted that their solution for surface temperature was not computed self-consistently with the resulting atmospheric chemistry.

TABLE 3.1: Table of impact models adapted from Zahnle et al. 2020

| Impactor | Buffer ^a | N ^b | CO ₂ ^c | Dry Atmosphere Products (bar) | | | | | |
|------------|---------------------|----------------|------------------------------|-------------------------------|------|-----------------|-----------------|-----------------|--------|
| | | | | H ₂ | CO | CO ₂ | CH ₄ | NH ₃ | |
| Max HSE | 1 | QFI | 0-1 | 100 | 57 | 5E-6 | 1.4E-5 | 9.0 | 0.08 |
| | 2 | | 100 | 74 | 1E-5 | 2E-6 | 7.6 | 0.050 | |
| | 3 | | IW | 100 | 35 | 4E-5 | 6E-4 | 13.7 | 0.086 |
| | 4 | | QFM | 100 | 10 | 0.11 | 65.6 | 13.6 | 0.01 |
| Pretty Big | 1 | | 0-2 | 20 | 7.6 | 5E-4 | 0.06 | 2.9 | 0.03 |
| | 2 | | | 5 | 7.4 | 6E-6 | 4E-4 | 0.34 | 0.01 |
| "Ceres" | | | 1-4 | 5 | 3.9 | 3E-4 | 0.06 | 0.52 | 0.006 |
| "Vesta" | 1 | | 2-10 | 5 | 3.9 | 0.06 | 1.6 | 0.17 | 0.002 |
| | 2 | | | 2 | 2.6 | 6E-4 | 0.4 | 0.054 | 0.0015 |
| | 3 | | | 1 | 2.0 | 2E-4 | 0.14 | 0.023 | 0.0011 |
| | 4 | | | QFM | 2 | 1.8 | 1E-5 | 0.02 | 0.28 |
| Sub-Vesta | 1 | QFM | 3-20 | 5 | 2.7 | 0.005 | 2.7 | 0.008 | 8E-4 |
| | 2 | | | 2 | 1.5 | 6E-5 | 0.1 | 0.36 | 0.037 |
| South Pole | 1 | QFM | 10-100 | 2 | 0.37 | 0.008 | 1.5 | 1E-7 | 2E-5 |
| -Aitken | 2 | | | 2 | 0.65 | 0.015 | 1.32 | 1E-6 | 7E-5 |

^a Mineral buffer that resulting atmosphere is assumed to equilibrate with.

^b Number of impactors of this mass bound between minimum and maximum veneer.

^c Pre-impact atmospheric CO₂ (bar).

3.1.2 Program

petitCODE (**P**ressure-**T**emperature **I**terator and **S**pectral Emission and **T**ransmission **C**alculator for **P**lanetary **A**tmospheres **C**ode) is a 1D plane-parallel radiative transfer code written by Paul Mollière (2017), adapted from the the irradiated circumstellar disk radiative transfer code by Dullemond et al. (2002). *petitCODE* was designed with the intention to calculate atmospheric structures and spectra of gas giant planets, and was benchmarked by Baudino et al. (2017) with *ATMO* (Tremblin et al. 2015) and *Exo-REM* (Baudino, J.-L. et al. 2015) codes. It is a 1D, plane-parallel model that is able to iterate to a converged thermal structure in radiative-convective equilibrium. Beginning with an initial temperature guess, molecular abundances and resulting opacities are then computed. Using the Feautrier method of integrating and balancing both the outgoing and incoming radiation at each layer, a new starting thermal profile is computed

assuming radiative-convective equilibrium, and the process repeats (Mollière et al. 2015). This radiative-convective equilibrium means that the flux of outgoing thermal emission from the planet balances the incoming stellar radiation.

The implementation of the correlated-k method — a cumulative distribution of opacity rather than individual spectral lines (see Lacis and Oinas 1991) — in *petitCODE* permits swift opacity calculations for these molecular species without the loss of detail of the order of 10^6 - 10^{10} spectral absorption lines that molecular species contain. This allows for lower resolution opacity tables to be used without losing the narrow line cores at low pressures, greatly reducing computation time (e.g. Lacis and Oinas 1991; Fu and Liou 1992; Mollière 2017). The relative errors in the flux using this method are generally an order of 1%, with the scattering regime error around 0% (Mollière 2017). The opacity data for these molecules is on a 3D grid ranging from 110nm-215 μ m, 80-3000 K, and 10^{-6} - 10^3 bar, and the nearest-neighbour values are used when regimes are encountered which fall outside of this grid (Mollière 2017; Mollière et al. 2019). For absorption line list, partition function, and pressure broadening sources for these molecules, see Mollière et al. (2015) Table 1, Mollière (2017) Table 3.1.

petitCODE also has a database of *PHOENIX* stellar models of main-sequence stars to model the wavelength-dependent contribution of the stellar spectrum irradiating the planet’s atmosphere from above (Mollière et al. 2015). In the scripting of *petitCODE*, a value of 1/3 of the given star’s main sequence lifetime was chosen for its age. As it is easiest to study hot Jupiter transits of K-type stars, which typically are at less than 1/2 of their main sequence lifetime, a lower value was chosen; however, variations in this value had little effect on resulting stellar spectra (Mollière et al. 2015).

petitCODE is able to handle calculations for both a planetary average and a dayside average. Both regimes assume isotropic incoming stellar flux, with the planetary average assuming that the amount of incoming stellar light is homogeneously spread over the

entire planet (Mollière 2017). The code also accounts for isotropic scattering within the atmospheres. Non-isotropic scattering is approximated in the diffusive regime, where the mean free path of a photon is very short. The depth of a planetary atmosphere compared to the UV to MIR wavelengths of interest (110nm to 250 μ m) allows us to treat the energy transport through the atmospheres as if it were along light rays of intensity I_ν , neglecting any effects of the physical wave property of the incoming light on scattering (Mollière 2017). Since the source function, S_ν , is dependent upon the solution to the mean intensity, and the atmospheric temperature is dependent upon intensity, an initial guess is implemented for a starting temperature, which sets the source function, which is then used to update the intensity and the temperature. This process is iterated until the atmosphere converges to radiative-convective equilibrium. The convergence criteria are met and iteration ceases when the rolling mean flux difference, which measures the deviation of the incoming and outgoing fluxes from the full angle and frequency dependent solutions, falls below 10^{-3} ; the rolling mean change in temperature falls below 10^{-3} ; the rolling mean change in the Planck mean opacity, κ_{Pla} , falls below 10^{-2} ; and the rolling mean change of the Rosseland mean opacity, κ_{Ros} , falls below 10^{-2} .

The Feautrier method was implemented in *petitCODE* to be able to integrate the equations of radiative transfer for the incoming and outgoing radiation, at each layer, simultaneously. At high optical depths, the energy transported by photons falls into the diffusive regime, due to the high probability of absorption at each layer. This regime requires a third order (or higher) numerical method to reach the correct solution. The Feautrier method allows for third order calculations with greater speed and accuracy than a third order quadrature at high optical depths (Dullemond 2012; Mollière 2017). This method is similar to 1D diffusion, and can thus re-produce diffusion in atmospheres well (Dullemond 2012). The Feautrier method is also able to retain full angular dependence of the radiation field, which is important for non-isotropic scattering, as well as the absorption term α_ν 's dependence on all rays in all directions. The radiative transfer is

turned into a tri-diagonalized matrix when solved. This method of solving the radiative transfer is common in stellar atmospheric codes (Dullemond 2012).

petitCODE, like *ATMO* (Tremblin et al. 2015), implements the equilibrium chemistry code outlined in the manual of the NASA Chemical Equilibrium with Applications (*CEA*) code, described in Gordon and McBride (1994) and McBride and Gordon (1996). This module is a Gibbs free energy minimizer which computes the chemistry for an isolated parcel of gas with constant temperature and pressure in the limit of time $t \rightarrow \infty$ using Lagrange multipliers and a multi-dimensional Newton-Raphson solver (Mollière 2017). This does not account for disequilibrium chemistry reactions, including those caused by the incoming stellar flux, such as the formation of O_3 on modern Earth and hazes on Titan. Following the second law of thermodynamics, $\Delta S > 0$, the Gibbs free energy must decrease, $\Delta G < 0$. This change in G is expressed by

$$dG = VdP - SdT + \sum_{j=1}^{N_{species}} \mu_j dN_j, \quad (3.2)$$

where V is volume, P is pressure, S is entropy, T is temperature, μ_j is the chemical potential, and N_j is the number of molecules of species j (Mollière 2017). This method calculates the thermodynamically favourable reactions in each layer of the atmosphere, making non-homogeneously mixed chemistry from the input atomic abundances to satisfy equation 3.2. This method does not include any disequilibrium, UV-driven chemistry.

This chemistry provides gamma values at each layer. This gamma, $\gamma = c_P/c_V$, represents the ratio of specific heats at constant pressure to the specific heats at constant volume, which are dependent upon the states of the gases within the atmosphere. This is not to be confused with the lapse rate, often represented by a capital gamma in $\Gamma = -\frac{dT}{dz}$, nor the ratio of visible to IR opacities in the Guillot (2010) analytic temperature solution, $\gamma = \kappa_v/\kappa_{th}$. For layers with a lapse rate that favours convective cooling, an adiabatic

temperature gradient is used at these pressures within the radiative transfer calculations (Mollière et al. 2015). This is known as adiabatic adjustment (see Marley et al. 1996), not an implementation of mixing length theory (Mollière et al. 2015).

In mixing length theory, a bubble of rising gas can travel a distance proportional to the pressure scale height, $l \propto H_P$. This pressure scale height H_P is the distance over which the pressure in the atmosphere decreases by a factor of e (Pierrehumbert 2010). This can be used to find an energy flux of the rising gas bubbles, which will allude to the time scales over which the convective gas rises from the surface to the tropopause. This time scale can then be used along with the timescale of the chemical reactions to determine whether the convective region contains a homogeneous mixture of chemistry. On modern Earth, this region of homogeneous chemistry extends up to the homopause at $0.3 \mu\text{bar}$, and is caused by convective mixing in the troposphere and turbulent mixing beginning in the stratosphere (Catling and Kasting 2017). In higher atmospheric layers where the pressure falls below $0.3 \mu\text{bar}$, the pressure is low enough to both allow for radiative cooling and prevent turbulent mixing, making this region of the atmosphere able to diffuse lighter molecules to the top. For an optically thick atmosphere, this homogeneous mixture may extend even higher, such as up to $0.02 \mu\text{bar}$ on Venus (Catling and Kasting 2017). In *petitCODE*, the convective regions only impact the temperatures, which then impact the chemistry at each layer, which does not account for homogeneous convective mixing in the higher pressures of the atmospheres or turbulent mixing up to the homopause. This equilibrium chemistry code is also not able to account for the $3.0 \times 10^{11} \text{ cm}^{-2} \text{ s}^{-1}$ of CO_2 outgassing. This value is consistent with the rate of volcanic outgassing from an Earth-like planet, and is commonly used in modern, benchmarked disequilibrium chemistry models (e.g. Hu et al. 2012; Pearce et al. 2022).

3.1.3 Procedure

The stellar effective temperature for the Sun during the Late Veneer was computed to be 5292.9 K using the 70.5% modern Solar flux value during this time period of 4.4 Ga (Heller et al. 2020). As the Earth’s semi-major axis lies at 1 AU ($\sim 215 R_{\odot}$), the Sun’s modern radius of $1 R_{\odot}$ was chosen for the young Sun’s radius. A heat flow value of 0.5 W/m^2 was used to compute an internal temperature of 54.5 K, 20 My after the ~ 4.5 Ga moon forming impact (Sleep 2010). This internal temperature is that of the total flux generated by the planet as a blackbody emitting at its internal temperature T_{int} , and is not representative of Earth’s core temperature. This flux contributes to the outgoing radiation field as σT_{int}^4 . Life would have needed to form sometime after the large, sterilizing impacts of the Late Veneer (Benner et al. 2020). By this time, Earth would have accreted all of its mass (Sleep 2010). As a result, modern Earth’s radius and mass were chosen. These were input into *petitCODE* as $0.089 R_{Jupiter}$ and $0.0031 M_{Jupiter}$, respectively, because *petitCODE* was initially scripted for work with hot Jupiters. Since we are using a 1D plane-parallel model, 130 atmospheric layers were chosen, consistent in order of magnitude with the 120 layers used when *petitCODE* was benchmarked (Baudino et al. 2017).

In Zahnle et al. (2020), after the major impacts occurred, Earth’s atmosphere settled into a chemical equilibrium, summarized in Table 3.1. They chose to focus on H_2 , CO, CO_2 , CH_4 , and NH_3 , as those are five most possible major gases in a reduced Earth atmosphere. All other gases were treated as trace (Zahnle et al. 2020). These were input as atomic number fractions of C, H, N, and O from the given partial pressures of their parent molecules for each model. These atomic abundances were then used by the Gibb’s free energy minimization within the chemistry module of *petitCODE* to build favourable molecules for the given pressures and self-consistent temperature computations. The output species were constrained to the H_2 , CO, CO_2 , CH_4 , and NH_3 of Zahnle et al. (2020), allowing these molecules to be re-formed in each layer in amounts favourable

TABLE 3.2: List of model shorthand and meaning for this work.

| | |
|-------|--|
| Z_D | Dry models using input chemistry from Zahnle et al. (2020), summarized in Table 3.1. |
| Z_W | Wet models using the input chemistry in Table 3.1, allowing H ₂ O to form the input where its presence is favourable to entropy. |
| H_D | Dry models using the same input as Z_D , with H ₂ -H ₂ collisional opacity omitted from the radiative transfer calculations. |
| H_W | Wet models using the same input as Z_W , with H ₂ -H ₂ collisional opacity omitted from the radiative transfer calculations. |

to radiative-convective equilibrium and Gibbs minimization. The opacity data of each species used had a resolution of $\lambda/\Delta\lambda = 10$. This low resolution kept computation time low, and has a relative error from a line-by-line opacity method in spectral regions with a considerable flux of at most 5%, and usually much less (Mollière et al. 2015).

Two sets of models were computed that contained the dry chemistry result of Zahnle et al. (2020) in Table 3.1 after vaporized oceans re-condensed leaving their atmospheres dry. One set was run with H₂-H₂ collisional opacity as an opacity source (Z_D), and the other without (H_D). In collisional opacity, two molecules collide together to form a temporary 'super-particle' featuring its own set of spectral features, effectively adding a new molecular 'species' at higher pressure. Following suit, two more sets of models were run in which the atomic abundances were also allowed to form H₂O wherever favourable (Z_W, H_W), though this does not reflect evaporative atmosphere-ocean coupling. The original chemistry from Zahnle et al. (2020) is the Z_D models, with the others being further investigation on our part. These models and their shorthand are referenced in Table 3.2.

Due to *petitCODE*'s development to model gas giant exoplanets (Mollière et al. 2015), and having been preceded by a circumstellar disk model (Dullemond et al. 2002), the

code currently lacks a surface boundary condition. Surface optical depth must therefore be taken into account when evaluating the models. A high surface optical depth is able to absorb all of the incoming stellar light, effectively acting as a surface condition. This signifies that the higher pressure atmospheres will fall within the acceptable surface conditions, consistent with the findings of Guillot and Showman (2002) that most incoming starlight is absorbed at pressures below 10 bar. This limitation and its allowances for use in this terrestrial regime are further discussed in Section 3.4.

3.2 Results – Thermal profiles

The first batch of models was run for testing the dry chemistry outputs from Zahnle et al. (2020), using the chemistry from Table 3.1 as chemical input (Z_D). We find that the 5 largest impactors fit into the optically thick regime acceptable by the lack of surface boundary, covering the maximum veneer (Max HSE 1) to minimum veneer (Pretty Big 1) impactors. All of the optically thick atmospheres were able to meet the convergence criteria of *petitCODE*. These results are shown in Fig. 3.1, with direct comparison of surface temperature in Table 3.3. We show that these dry models have underestimated surface temperatures using Eq. 3.1 for all cases. As a general trend, for the Z_D cases in Fig. 3.1, as the surface visible optical depth increases, so do both the surface temperature and surface pressure. Currently, we are using the lower optical depth models across all cases as a check of self-consistency. It is important to note that we are working to implement the appropriate surface boundary conditions for future work.

All of the Z_D models in Fig. 3.1 have convective layers. For the optically thick cases, we find that the convective region ends just below the tropopause, which occurs near 10^{-1} bar, consistent with modern Earth. This is the pressure where we expect to find the tropopause in an atmosphere where this region aligns with the coldest part of the thermal profile (Catling and Kasting 2017). Our calculations find that typical values of

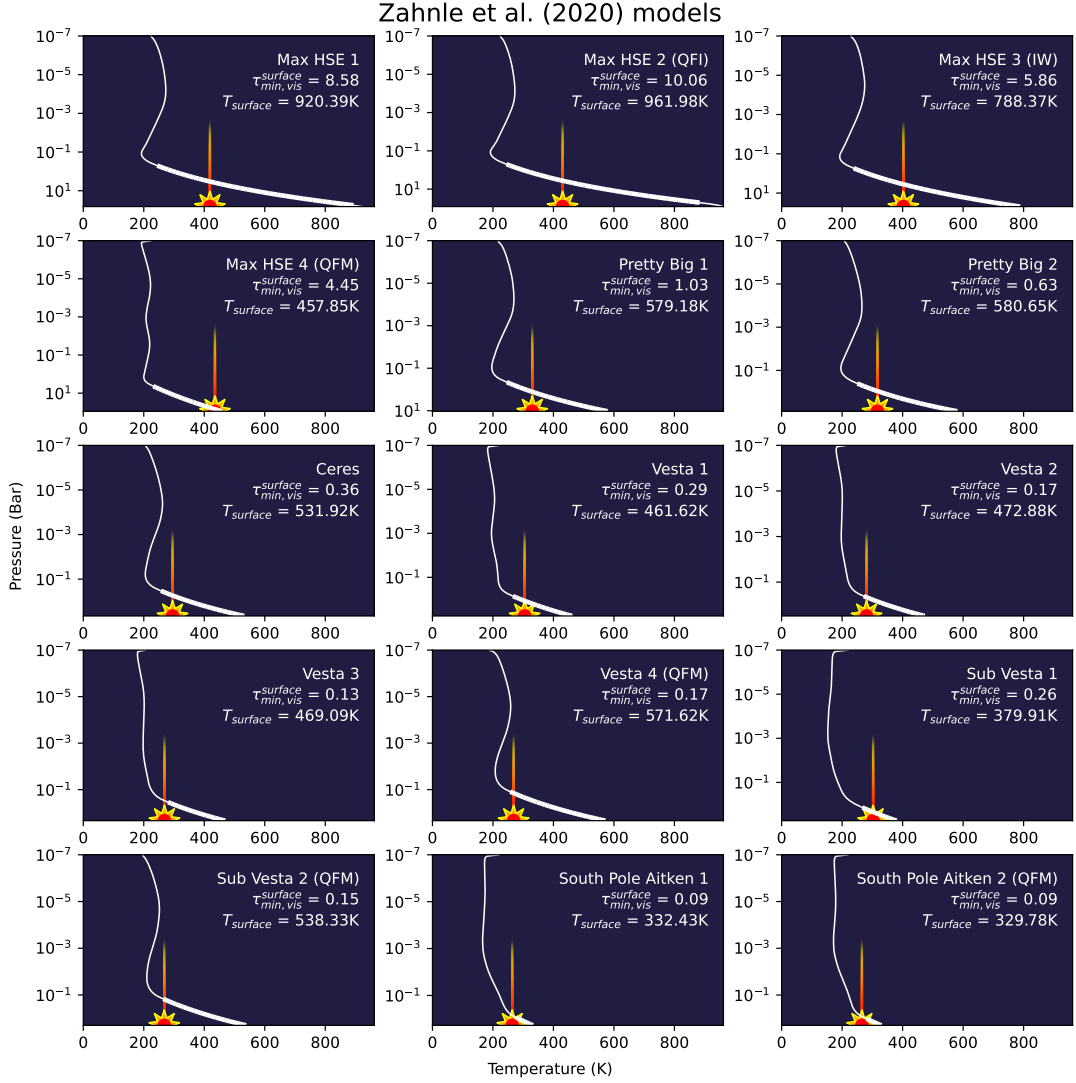


FIGURE 3.1: The self-consistent PT profiles for the dry atmosphere cases of Zahnle et al. (2020), using the input chemistry abundances found in Table 3.1 (Z_D). The bold sections of the thermal profiles indicate convective regions. The impactor in each plot represents the value for the surface temperature solution from Zahnle et al. (2020), found in Table 3.3, to allow for visual comparison between the analytic and computed surface temperatures.

$\gamma = C_P/C_V$ for all cases range around $1.3 \rightarrow 1.4$, consistent with a diatomic ideal gas $\gamma = 7/5$.

We find that, for Max HSE 2, the case with the highest minimum τ value across the

visible spectrum, $2.87 \times 10^{-5}\%$ of the incoming stellar light has not yet been absorbed or scattered by the time it reaches the surface layer. As this is a negligible percentage, we confidently show that the lack of surface boundary condition does not impair results for this optically thick, diffusive regime. For the next highest minimum τ and surface temperature, Max HSE 1, we find that $1.80 \times 10^{-4}\%$ of the incoming stellar light remains at the surface layer. For Max HSE 4, which shows the closest agreement of self-consistent and analytic surface T calculations, $7.38 \times 10^{-2}\%$ of the incoming stellar light remains at the surface. This amount increases to 2.67% for the Pretty Big 1 case, with the Pretty Big 2 case failing to absorb 6.01% of the incoming stellar light, placing these at the low end of optical depths that justify the lack of surface boundary condition in this work.

The most optically thin models, South Pole Aitken 1 & 2, still retain 48.66% and 44.84% of the incoming stellar light at the bottom layers, respectively. As Earth is a terrestrial planet and the steady state atmosphere of modern Earth is optically thin, this obstacle motivates further investigation of this parameter space with the appropriate surface boundary conditions in place.

We note that each case in Fig. 3.1 contains a turnover in the upper atmosphere, creating a stratosphere, pointing to the presence of a visible absorber. We note from the chemistry available to form in Table 3.1 and Fig. 3.6 that there are no strong visible absorbers in the atmosphere. We attempt to understand this by running the radiative transfer and chemistry allowing H₂O to form (Z_W), and removing H₂-H₂ collisional opacity from the radiative transfer for both this dry (H_D) and the subsequent wet (H_W) cases.

The second batch of models, Z_W , allows for the formation of H₂O in solid, liquid, and gas phases within the atmospheres, from the input chemical building blocks of Table 3.1. This H₂O is not a representation of ocean-atmosphere coupling, including its effects on latent heat release from evaporation and condensation into clouds. We find that for

this case as well, the 5 largest impactors fit into the optically thick regime, covering the maximum veneer to minimum veneer impactors. The results in Fig. 3.2 show that Eq. 3.1 underestimates the surface temperature for these cases as well, as they are all hotter than the analytic result. As a general trend, for the wet cases in Fig. 3.2, as the surface visible optical depth increases, so do both the surface temperature and surface pressure, as with Z_D from Fig. 3.1. We note that the wet models for Sub Vesta 1 and South Pole Aitken 2 strayed far from convergence criteria, and are only included in Fig. 3.2 for completeness.

As with Z_D , we find that all of the Z_W models also contain convective regions, ending near the tropopause’s expected 10^{-1} pressure (Catling and Kasting 2017). As above, γ values also range around $1.3 \rightarrow 1.4$, consistent with a diatomic ideal gas $\gamma = 7/5$. This is due to the lack of latent heat release in the code, as this water is not evaporated. Since the air is moist — but not saturated — this similarity to an ideal gas is valid and expected (Williams and Ambaum 2021).

For the Z_W models, Fig. 3.2 shows that the surface temperature and optical depth of Max HSE 2 remain the highest, as with the Z_D case in Fig. 3.1, and Max HSE 4 remains the closest to the analytic solution among the optically thick cases. In the thickest case of Max HSE 2, we compute that $2.86 \times 10^{-5}\%$ of the incoming stellar light has not yet been absorbed, comparable with the Z_D case. For the thinnest optically thick case, Pretty Big 1, $9.60 \times 10^{-1}\%$ of the incoming stellar light is neither absorbed nor scattered by the time it reaches the surface, which is ~ 1 order of magnitude lower than that of the corresponding Z_D case. This may be due to H_2O replacing CO_2 as the third most abundant chemical species in this model. We also find that the stratosphere remains from the Z_D models, still without the introduction of a strong optical absorber.

We next investigate the contribution of $\text{H}_2\text{-H}_2$ collisional opacity to the surface temperature. These models used the same input as the previous models, and were computed

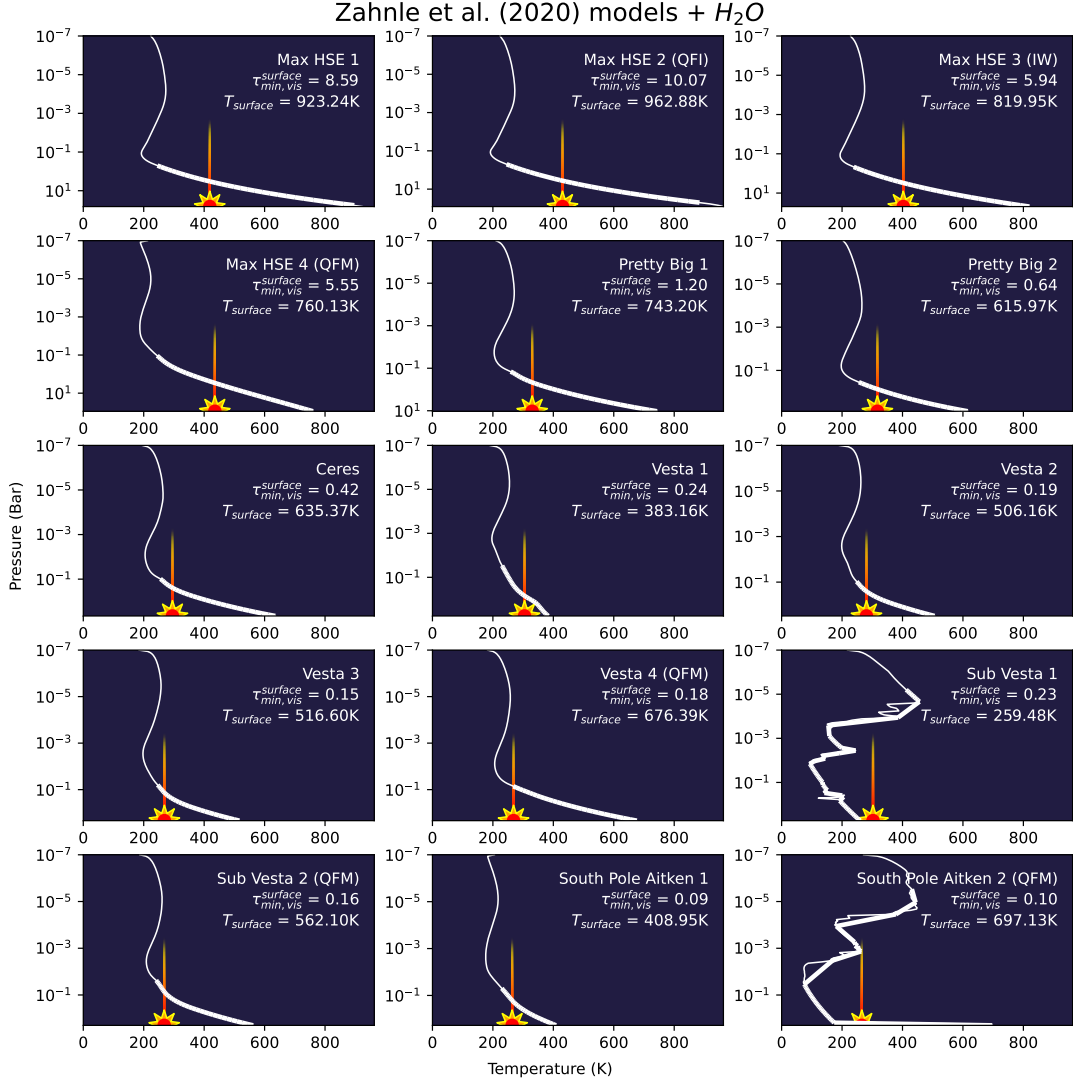


FIGURE 3.2: The self-consistent PT profiles for the wet atmosphere cases of Zahnle et al. (2020), using the input chemistry abundances found in Table 3.1, and allowing H₂O to be built from the input chemistry as discussed in Section 3.1.3 (Z_W). The bold sections of the thermal profiles indicate convective regions. The impactor in each plot represents the value for the surface temperature solution from Zahnle et al. (2020), found in Table 3.3, to allow for visual comparison between the analytic and computed surface temperatures. The solutions for Sub Vesta 1 and South Pole Aitken 2 diverged, failing to meet convergence criteria, and are only included for completeness.

self-consistently with the H₂-H₂ absorption features missing from the radiative transfer calculations. In the H_D case, the largest effect, shown in Fig. 3.3, occurred in the higher pressure atmospheres when compared with Fig. 3.1. Max HSE 4 in this case remained close to the analytic solution even with the removal of the H₂-H₂ collisional opacity; this atmosphere remained CO₂ dominant throughout, as with the cases in Fig. 3.1, 3.6.

The optically thick models in Fig. 3.3 all have self-consistent surface temperatures that fall near their analytic solutions from Zahnle et al. (2020). This suggests that the analytic solutions of Eq. 3.1 and the moist adiabat they represent do not account for the collisional opacities within high pressure H₂ dominant atmospheres. The contribution of H₂-H₂ collisions to the optical depth at each wavelength are shown in Fig. 3.4. The implications of this are discussed further in Section 3.4.

The H_W case shows that the increase in H₂O abundance is able to help trap heat more efficiently as well. Whereas before, our self-consistent result for Max HSE 4 was very close to the analytic temperature solution, with the inclusion of H₂O, it heats up as much as the Z_W case, since this atmosphere is CO₂ and not H₂ dominant. It is interesting to note that, while the higher pressure optically thick atmospheres expectedly cool when H₂-H₂ collisional opacity is removed from the radiative transfer calculations, we note a lack of convection in the Max HSE 2 case in Fig. 3.5. This atmosphere was efficient at radiative cooling, suggesting that the collisional opacity of H₂ plays an important role in how heat is trapped in these optically thick, reducing atmospheres.

3.3 Results – Atmospheric chemistry

Using the homogeneous composition of Table 3.1, we show in Fig. 3.6, the Z_D case, that the atmospheric composition does not favour a homogeneous mix among the trace species. Contrary to the work of Zahnle et al. (2020), we note in Fig. 3.6 that CO is very sensitive to the atmosphere’s thermal profile, closely matching each respective profile

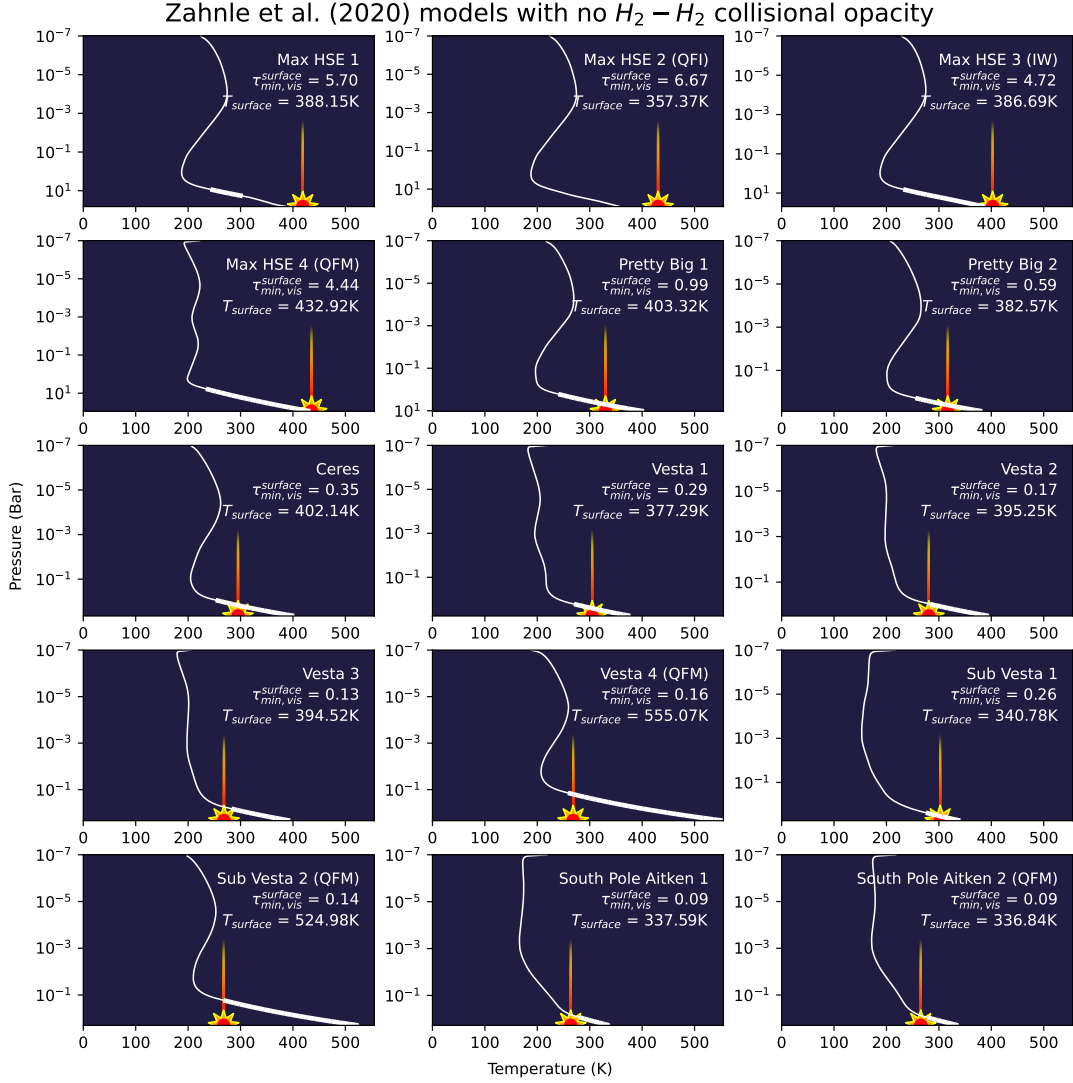


FIGURE 3.3: The self-consistent PT profiles for the dry atmosphere cases of Zahnle et al. (2020), with the opacity contribution of H_2-H_2 collisions omitted from the radiative transfer, using the input chemistry abundances found in Table 3.1 (H_D). The bold sections of the thermal profiles indicate convective regions. The impactor in each plot represents the value for the surface temperature solution from Zahnle et al. (2020), found in Table 3.3, to allow for visual comparison between the analytic and computed surface temperatures.

from Fig. 3.1. As previously stated, the reduced biological precursor models which need to be present in large amounts are all Carbon-carriers, with the exception of ammonia. This shows an important altitude-dependence on the abundances of at least one C source,

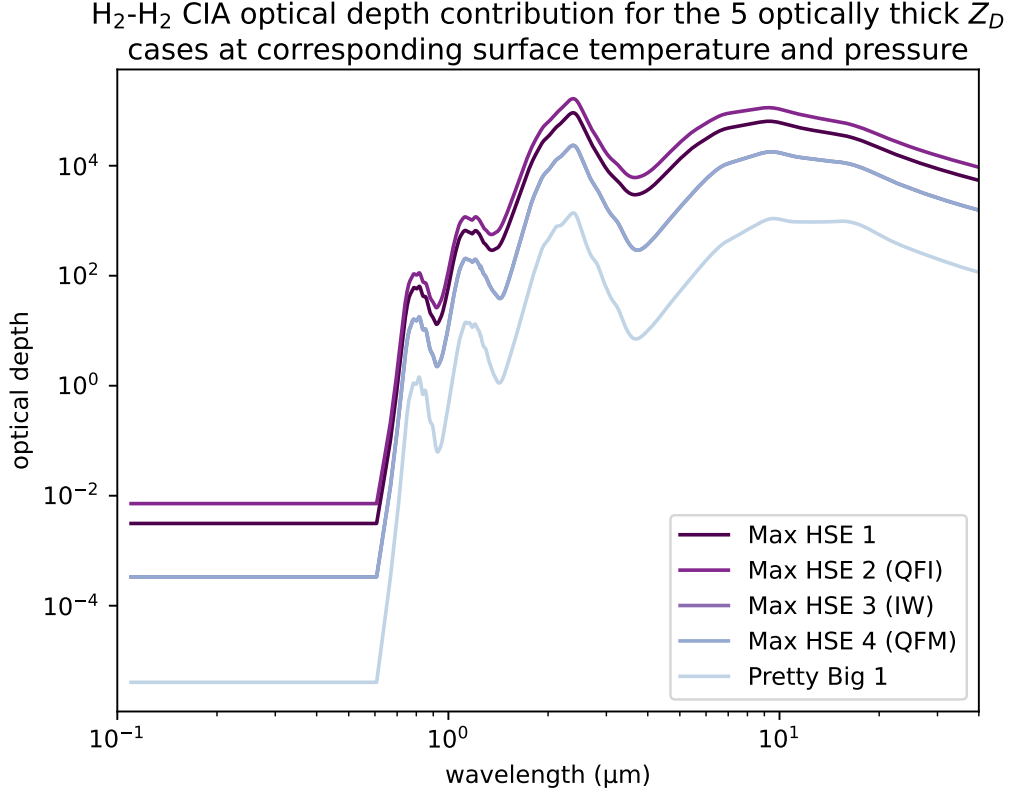


FIGURE 3.4: The contribution of the collisional induced absorption of H₂-H₂ collisions to the optical depth at each wavelength, applied to the surface layers of the Z_D cases with $\tau_{min,vis}^{surface} > 1$. The opacities are calculated accounting for the abundance of H₂, pressure, and temperature at the lowest layer of the atmosphere. This contribution to the optical depth is excluded from the thermal profile calculations of the H_D cases.

which should be factored in when studying altitude-dependent disequilibrium chemistry.

In all optically thick Z_D cases, compared with the final, and input, chemistry found in Table 3.1, the dominant species remained the dominant species of each atmosphere. That species is H₂ for all optically thick cases, except for Max HSE 4 which is CO₂ dominant; however, following our self-consistent calculations in this Max HSE 4 case, the second-most dominant molecular species in Table 3.1, CH₄, is switched with H₂ as the new second-most dominant species.

Allowing water to form in the Z_W atmospheres has a large impact on CO₂ abundances

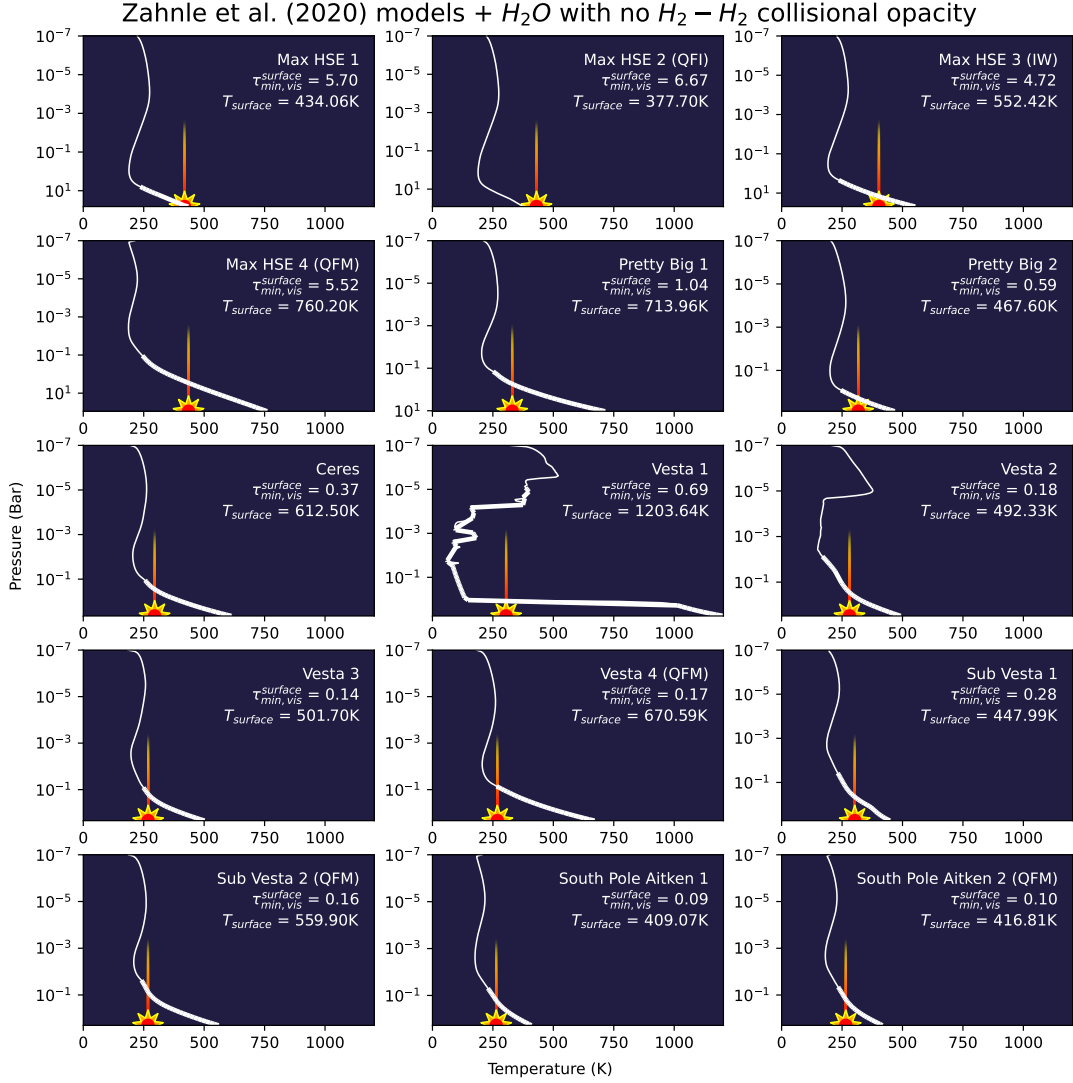


FIGURE 3.5: The self-consistent PT profiles for the wet atmosphere cases of Zahnle et al. (2020), with the opacity contribution of H₂-H₂ collisions omitted from the radiative transfer, using the input chemistry abundances found in Table 3.1 and allowing H₂O to form from these input abundances (H_W). The bold sections of the thermal profiles indicate convective regions. The impactor in each plot represents the value for the surface temperature solution from Zahnle et al. (2020), found in Table 3.3, to allow for visual comparison between the analytic and computed surface temperatures. Vesta 1 and Vesta 2 strayed far from convergence, and are included for completeness.

TABLE 3.3: Comparison of Zahnle et al. (2020) analytic surface temperature solutions using Eq. 3.1 to our self-consistent surface temperature calculations from Zahnle et al. (2020), Table 3.1.

| | | Surface Temperatures (K) | | | | | |
|------------|------------------------|--------------------------|--------|--------|--------|--------|---------|
| Impactor | Surface P ^a | Analytic ^b | Z_D | Z_W | H_D | H_W | |
| Max HSE | 1 | 66.08 | 418.68 | 920.39 | 923.24 | 388.15 | 434.06 |
| | 2 | 81.65 | 430.35 | 961.98 | 962.88 | 357.37 | 377.70 |
| | 3 | 48.79 | 402.49 | 788.37 | 819.95 | 386.69 | 552.42 |
| | 4 | 89.22 | 435.34 | 457.85 | 760.13 | 432.92 | 760.20 |
| Pretty Big | 1 | 10.59 | 330.00 | 579.18 | 743.20 | 403.32 | 713.96 |
| | 2 | 7.75 | 316.87 | 580.65 | 615.97 | 382.57 | 467.60 |
| "Ceres" | | 4.49 | 295.16 | 531.92 | 635.37 | 402.14 | 612.50 |
| "Vesta" | 1 | 5.73 | 304.69 | 461.62 | 383.16 | 377.29 | 1203.64 |
| | 2 | 3.06 | 280.81 | 472.88 | 506.16 | 395.25 | 492.33 |
| | 3 | 2.16 | 268.38 | 469.09 | 516.60 | 394.52 | 501.70 |
| | 4 | 2.16 | 268.38 | 571.62 | 676.39 | 555.07 | 670.59 |
| Sub-Vesta | 1 | 5.41 | 302.40 | 379.91 | 259.48 | 340.78 | 447.99 |
| | 2 | 2.00 | 267.71 | 538.33 | 562.10 | 524.98 | 559.90 |
| South Pole | 1 | 1.89 | 263.76 | 332.43 | 408.95 | 337.59 | 409.07 |
| Aitken | 2 | 1.99 | 265.45 | 329.78 | 697.13 | 336.84 | 416.81 |

^a Surface pressure of atmosphere in bar.

^b Analytic temperature solution from Zahnle et al. (2020) using equation 3.1, using given surface P.

in every case, overwhelming the potent greenhouse gas with H₂O's even more powerful greenhouse (Held and Soden 2000), shifting the absorption to longer wavelengths with much wider absorption bands. Fig. 3.7 shows that, for the optically thick models, there is no liquid water formed this way, with the exception of a small amount below the tropopause in Max HSE 4, showing again that this H₂O treatment is not a replacement for cooling from latent heat release of evaporating and condensing liquid water clouds.

Unlike the Z_D Max HSE 4, the Z_W Max HSE 4 retains CH₄ as the second-most dominant molecular species. In this case, we also find that, following our self-consistent calculations, H₂ is a trace species now that H₂O is able to form. Even following this switch, we find that the presence of H₂O heats this surface much higher than the analytic

TABLE 3.4: Self-consistent Bond albedo for each atmosphere.

| Impactor | | Bond albedo | | | |
|-----------------|---|-------------|-------|-------|-------|
| | | Z_D | Z_W | H_D | H_W |
| Max HSE | 1 | 0.45 | 0.45 | 0.52 | 0.52 |
| | 2 | 0.45 | 0.45 | 0.52 | 0.52 |
| | 3 | 0.46 | 0.45 | 0.52 | 0.49 |
| | 4 | 0.27 | 0.28 | 0.53 | 0.28 |
| Pretty Big | 1 | 0.46 | 0.31 | 0.49 | 0.31 |
| | 2 | 0.43 | 0.41 | 0.46 | 0.44 |
| "Ceres" | | 0.40 | 0.27 | 0.41 | 0.28 |
| "Vesta" | 1 | 0.39 | 0.26 | 0.31 | 0.28 |
| | 2 | 0.32 | 0.21 | 0.32 | 0.21 |
| | 3 | 0.28 | 0.20 | 0.28 | 0.20 |
| | 4 | 0.31 | 0.25 | 0.31 | 0.25 |
| Sub-Vesta | 1 | 0.39 | 0.36 | 0.39 | 0.23 |
| | 2 | 0.29 | 0.22 | 0.29 | 0.22 |
| South Pole | 1 | 0.24 | 0.20 | 0.24 | 0.20 |
| Aitken | 2 | 0.25 | 0.25 | 0.25 | 0.20 |

solutions. This increase in temperature due to the presence of H₂O is also seen in the Pretty Big 1 case, where H₂O replaces CO₂ as the third-most dominant species, pushing the concentration of CO₂ to a trace species. This action is shown to be negligible in the three highest opacity cases, which we show in Fig. 3.7.

Fig. 3.8 and 3.9 demonstrate that removing the H₂-H₂ collisional opacity, thus altering the thermal structure of the atmosphere, has very little effect on the amount of the dominant species within the atmosphere for both wet and dry cases. They are included here for completeness, and to demonstrate that removing the effect of the H₂-H₂ collisional opacity does not have significant impact on the mixture of chemistry, nor the final radiative transfer results presented in Section 3.2.

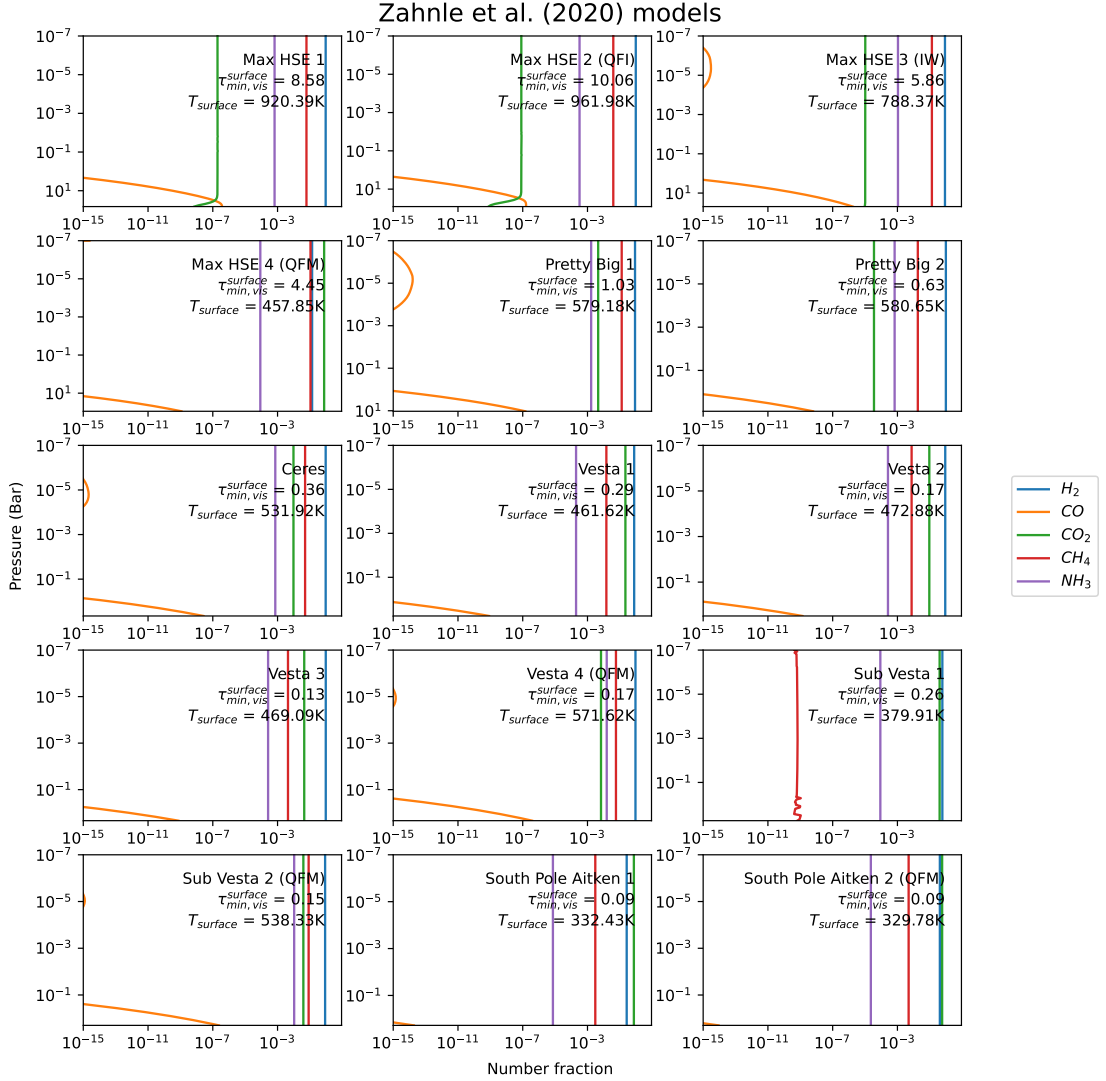


FIGURE 3.6: The self-consistent number fraction abundances of the resulting chemistry species for the dry atmosphere cases of Zahnle et al. (2020), using the input chemistry abundances found in Table 3.1 (Z_D). The x-axes are plotted in a logarithmic scale for ease of differentiating the lower number mass abundances from the dominant species. An arbitrary cutoff number to plot the number fraction of each species was chosen because a very small number fraction is $\sim 0\%$ of the composition.

3.4 Discussion

With our self-consistent results, we are able to prove that water may have a large impact on the thermal structure of an atmosphere, depending on the overall atmospheric

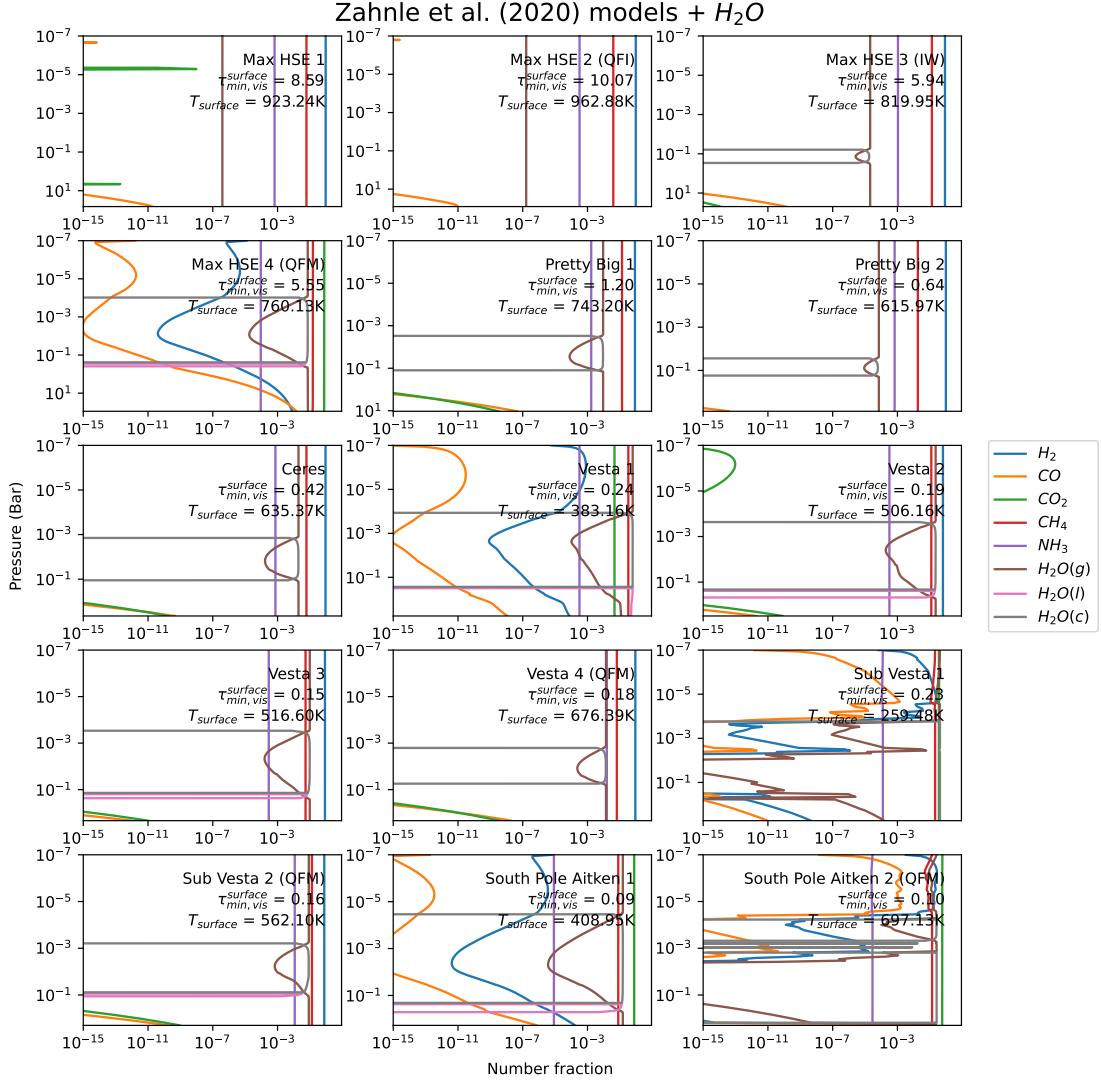


FIGURE 3.7: The self-consistent number fraction abundances of the resulting chemistry species for the wet atmosphere cases of Zahnle et al. (2020), using the input chemistry abundances found in Table 3.1, and allowing H₂O to form from the input species as describe in Section 3.1.3 (Z_W). For H₂O, *g* denotes the gas phase, *l* denotes the liquid phase, and *c* denotes the crystalline phase. The x-axes are plotted in a logarithmic scale for ease of differentiating the lower number mass abundances from the dominant species. An arbitrary cutoff number to plot the number fraction of each species was chosen because a very small number fraction is ~0% of the composition.

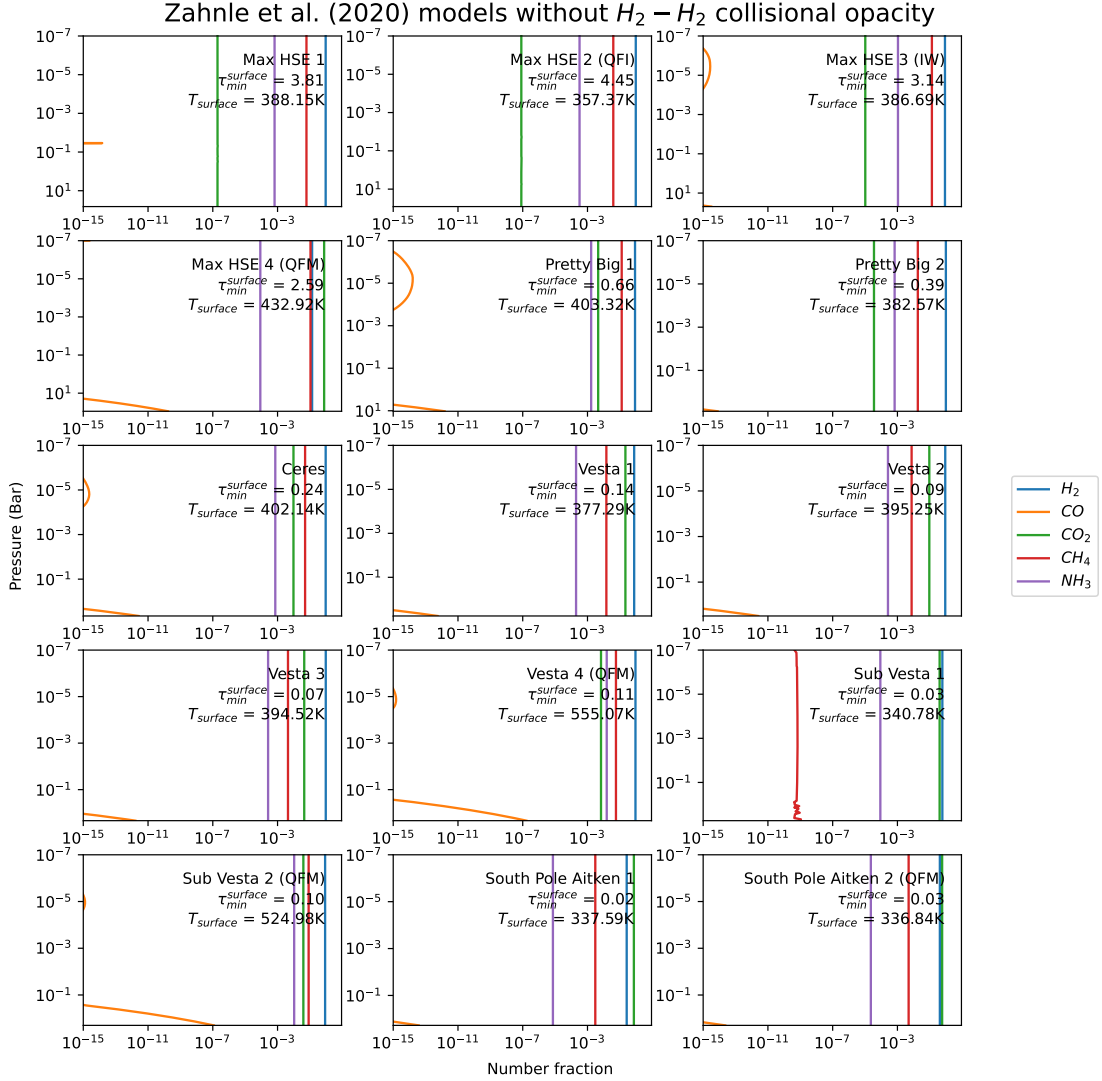


FIGURE 3.8: The self-consistent number fraction abundances of the resulting chemistry species for the dry atmosphere cases of Zahnle et al. (2020) without H_2 - H_2 collisional opacity, using the input chemistry abundances found in Table 3.1 (H_D). The x-axes are plotted in a logarithmic scale for ease of differentiating the lower number mass abundances from the dominant species. An arbitrary cutoff number to plot the number fraction of each species was chosen because a very small number fraction is $\sim 0\%$ of the composition.

composition. This includes the possible latent heat release that the introduction of a water cycle with evaporative cloud condensation may provide to allow for a better picture of the thermal structure of an atmosphere. This is the case with Max HSE 4, a

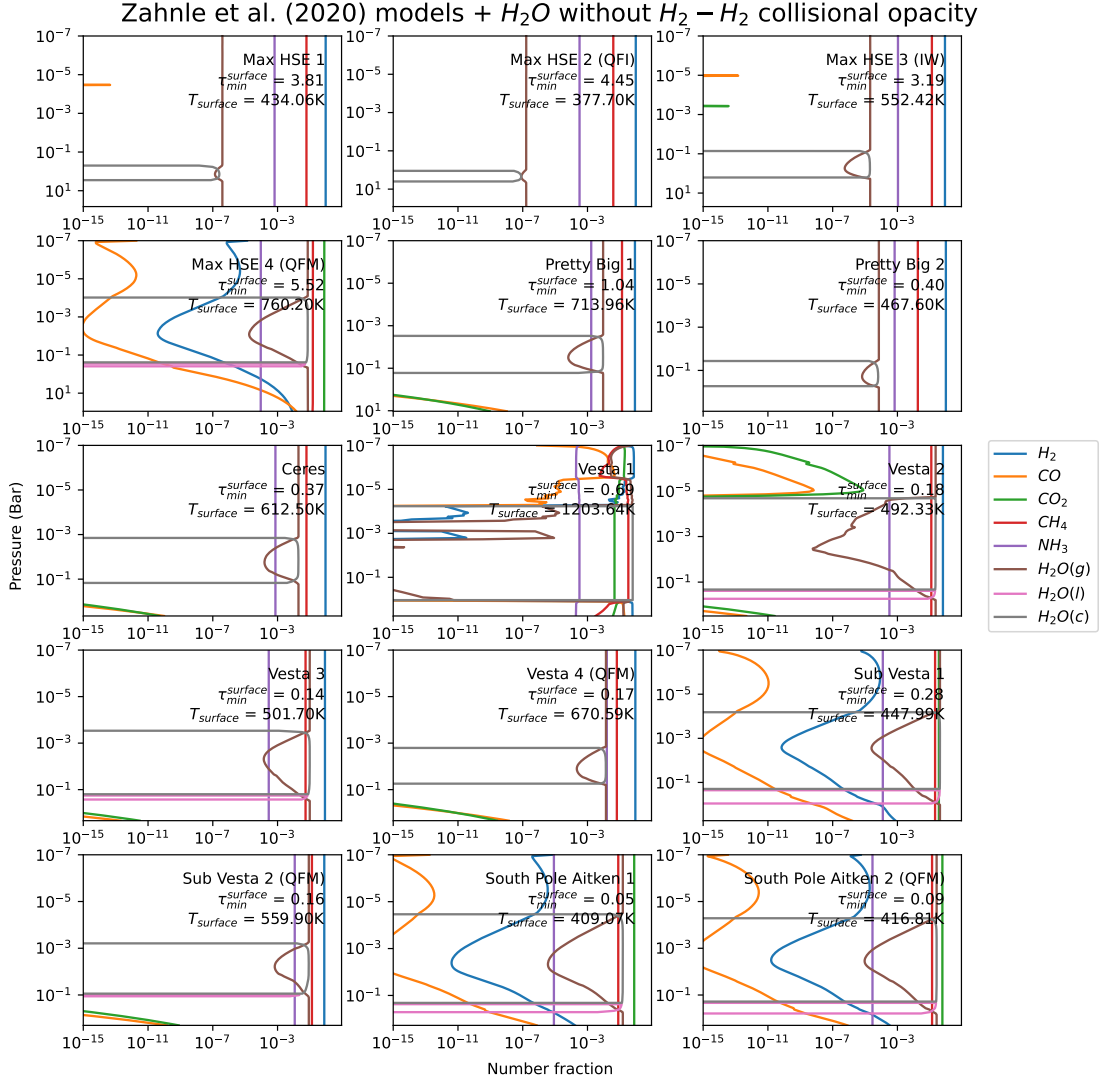


FIGURE 3.9: The self-consistent number fraction abundances of the resulting chemistry species for the wet atmosphere cases of Zahnle et al. (2020) without H_2-H_2 collisional opacity, using the input chemistry abundances found in Table 3.1, and allowing H_2O to form from the input species as describe in Section 3.1.3 (H_W). For H_2O , g denotes the gas phase, l denotes the liquid phase, and c denotes the crystalline phase. The x-axes are plotted in a logarithmic scale for ease of differentiating the lower number mass abundances from the dominant species. An arbitrary cutoff number to plot the number fraction of each species was chosen because a very small number fraction is $\sim 0\%$ of the composition.

CO₂ dominant model that may be indicative of the type of reducing chemistry in an atmosphere following H₂ escape, which saw the largest changes in temperature between wet to dry cases out of all of the optically thick models, as illustrated in Table 3.3. We also demonstrate the importance of self-consistent chemistry and radiative transfer calculations to account for the opacity induced through H₂-H₂ collision in high pressure post-impact atmospheres, which will alter the length of time before the surface has cooled enough to sustain a water cycle. An important note is that Zahnle et al. (2020) adjusted the analytic solution to fit that of modern Earth, whose atmospheric chemistry is well understood to have been quite different in the past (e.g. Sagan and Mullen 1972). We ultimately show that a self-consistent treatment of equilibrium chemistry is imperative for both the starting thermal profiles from which disequilibrium chemistry may be computed and the initial mixture of chemistry from which these important biomolecule precursors can form.

In these results, the limitation of lack of surface boundary condition, as mentioned in Section 3.1.2, is possible to be overlooked. The optically thick atmospheres, which function as the surface boundary condition by preventing incident stellar light from reaching the planetary surfaces, are from the largest impactor cases. These cases of large impactors are more likely to have occurred due to the absence of a substantial veneer on the Moon. If only a small number of high mass impactors delivered the Earth's veneer, either the Moon or Earth would have collected the veneer (Benner et al. 2020); however, if a series of smaller impact events were to have occurred, 80 of the Vesta mass impactors found in Table 3.1 would have been necessary to deliver the Earth's full veneer, and the ratio of Earth to the Moon's veneer would more closely resemble that of their gravitational cross-sections (Benner et al. 2020). This series of smaller impacts would have also left behind evidence in the zircon record, of which none has been discovered (Benner et al. 2020).

3.4.1 Effects of Water

In general, the inclusion of water in the equilibrium chemistry not only alters the composition by favouring water formation over other molecules, it can also have a significant impact on surface temperature, especially in the lower pressure optically thick cases of Max HSE 4 and Pretty Big 1. Between the Z_D and Z_W cases, Max HSE 4 and Pretty Big 1 showed an increase in surface temperature by 302.28 K and 249.18 K, respectively, following the inclusion of water as a new source of greenhouse opacity. In the Z_W Max HSE 4, the dominant species are now more oxidized than before, though these oxidizing conditions may still allow for sufficient biomolecule formation (Pearce et al. 2022). To obtain the full picture of H_2O concentration in all cases, it will be necessary to self-consistently include the vapour pressure and corresponding opacities near and at saturation for water and its effect on the thermal structure and amount of further formation of water in the atmosphere.

These models also lack condensed clouds, which we are able to overlook in our models. Importantly, pre-industrial cloud condensation nuclei (CCN) levels were not only lower than on modern Earth, but the majority of CCN form from oxidation of plant and eukaryotic algae respiration (Rosing et al. 2010). A lower amount of CCN results in larger water droplets that rain out more quickly than the evaporative clouds on modern Earth, and scatter incoming visible light less efficiently (Rosing et al. 2010). This can be seen on modern Earth, where regions of ocean with low biologic productivity are more transparent to incoming visible light than areas with a higher biologic productivity (Kump and Pollard 2008). There is evidence of this larger droplet sizes on early Earth from Som et al. (2012), in which they show that the average droplet radius during the Archean eon (3.8-2.5 Ga), which follows the Hadean, was $17\mu m$, larger than the modern Earth's $12\mu m$. The largest possible droplet size due to raindrop fragmentation, regardless of air density, shows that droplets can not exceed a theoretical radius of 3.4mm for all stages of Earth's history (Som et al. 2012). The possibility of a bias in this

fossilized raindrop size was determined to be statistically unlikely given the 18 distinct bedding surfaces that were studied (Goosmann et al. 2018).

These larger cloud droplets that rain out more quickly would have lowered Earth’s albedo. During the Late Veneer, continental crust growth models show that the amount of Earth’s crust above sea level would only have reached 12.8% of the modern crustal surface area by 3.7 Ga (Pearce et al. 2017); this lower continental coverage further lowers the average surface albedo, resulting in higher absorption and less scattering of the incoming visible light, leading to further heating (Rosing et al. 2010). Hazes may play an important role in attenuating incoming stellar light in high pressure, post-impactor atmospheres.

3.4.2 Effects of H₂

Following the cooling of Earth’s magma surface post-impact, the dipole-induced greenhouse could have kept Earth’s surface too hot for a liquid water cycle for millions of years. While the equilibrium chemistry inputs from Zahnle et al. (2020) were computed from reactions during the impact until the evaporated oceans had fully rained out, our models don’t account for the subsequent H₂ loss due to atmospheric escape, and show a differing surface temperature from the analytic solutions from Eq. 3.1. Zahnle et al. (2020) do account for this escape of hydrogen, including the photodissociation and subsequent oxidation of CH₄ and the photodissociation of H₂O, in their disequilibrium photochemical models, but do not compute the thermal profile with the large amount of H₂ in mind. This may lead to a calculation of reducing chemistry and biomolecule yields of an atmosphere whose thermal profile suggests a neutral atmosphere after H₂ escape that is potentially cool enough for liquid water, but whose disequilibrium abundances suggest an atmosphere rich in H₂, potentially too hot for a wet-dry cycle.

A case of strong evidence for this is the CO₂ dominant Max HSE 4 atmosphere. The Z_D case, depicted in Fig. 3.1 and compared in Table 3.3, shows a greenhouse comparable

to that expected from the analytic solution by Eq. 3.1. This case also holds promise, as the atmospheric chemistry was allowed to equilibrate post-impact with the QFM mineral buffer; this buffer represents the mantle of modern Earth and the chemistry of volcanic outgassing. This suggests that, following hydrogen escape, the analytic surface temperature solution may hold more validity under such a strong greenhouse, as long as this escaped hydrogen is accounted for in the disequilibrium calculations, and the correct abundances of H₂O including the lower concentration of CCN and H₂O photodissociation are accounted for in the $\gamma = C_P/C_V$ used in each analytic solution.

3.4.3 Possible Solutions

The lack of hazes in our presented models may be a source of increased heating. A solar system object analogous to the type of reducing atmosphere expected on early Earth is Saturn’s largest moon Titan. In Titan’s nitrogen and methane-dominant, strongly reducing atmosphere, photochemical hazes called tholins are able to form. These hazes consist of the breakdown of atmospheric methane (CH₄) into long-chain hydrocarbons, such as ethane (C₂H₆), propane (C₃H₈), and methylacetylene (CH₃CCH) (Hörst 2017).

While the albedos for our models, shown in Table 3.4, are quite large for the optically thick cases, the early Earth and its strong reducing atmosphere are expected to have had thicker hazes than those of modern Titan (Zahnle et al. 2020). These hazes increase the atmosphere’s ability to reflect incoming light, acting as an antigreenhouse and cooling the surface. Titan’s Bond albedo is measured to be 0.27 ± 0.04 (Younkin 1974), comparable with the Bond albedo computed by McKay et al. (1989) for both the cloudless (0.32) and nominal cloud models (0.33) of Titan, where their haze model was determined by Titan’s geometric albedo. McKay et al. (1989) also noted that the visible spectrum between 0.3–0.6 μ m lacks notable methane absorption lines, allowing this wavelength region in Titan’s atmosphere to be used in determining the properties of the hazes.

The optical depth of Titan’s hazes at 0.5 μ m is $\tau \approx 3$, with latitudinal and seasonal

variations due to the Sun’s effect on haze production (McKay et al. 2001). For the the Max HSE cases, Zahnle et al. (2020) calculated that the haze optical depth at $0.5\mu\text{m}$ is in the range of $\tau = 4 \rightarrow 8$, over double the optical depth of hazes on Titan, with a haze production rate $10^3\times$ that of modern Titan’s. The faint young Sun would have been rotating more quickly, creating a strong magnetic dynamo. The processes affected by this magnetic field would have greatly increased the intensity of X-ray, EUV, and FUV spectral bands from the young Sun (Cnossen et al. 2007). The computed optical depth τ by Zahnle et al. (2020) for the Max HSE cases exceeds 100 in the UV spectrum, potentially protecting the nucleobases and RNA, along with sedimentation and deep ponds, from solar damage (Pearce et al. 2017). Meanwhile, the single minimum veneer Pretty Big impactors favoured an organic haze production whose optical depth at $0.5\mu\text{m}$ ranged over $\tau = 3 \rightarrow 5$, around that of modern Titan’s $\tau \approx 3$ (Zahnle et al. 2020). McKay et al. (1991) were able to calculate that the haze layer on Titan is sufficient to provide 9 K worth of cooling due to its antigreenhouse effect.

Looking to the Z_D cases, in order for our post-impact atmospheres to cool to the analytic solution without H_2 escape, after rearranging Eq. 3.1 and using our solar flux of 70.5% that of modern day, we find that the albedo must be 0.99 in all optically thick cases using the computed $\gamma = 7/5$, as reflective as Saturn’s moon Enceladus. Using a modern Earth moist adiabat $\gamma = 1.15$, we instead find that the Bond albedo must be ~ 0.5 for the optically thick cases, including the very close Max HSE 4 case that only has a self-consistent albedo of 0.29. This demonstrates that further processes beyond just an increased albedo are necessary to cool the surface, and as evidenced by Max HSE 4, must be incorporated self-consistently to account for various climate feedbacks. As an alternative example, a doubling of CO_2 on modern Earth would raise surface temperatures by ~ 1.2 K, but including the climate feedback of increased water evaporation at these higher temperatures, the overall surface increase would be 2.0-4.5 K. This suggests a complex chain of interrelated conditions and processes that could

ultimately lead to a cooler or hotter surface (Catling and Kasting 2017).

Another possible solution is that the impact(s) of the Late Veneer Hypothesis never occurred. With the limited evidence of an extended period of bombardment by such massive impactors in both the zircon record and the veneer ratio between the Moon and Earth, it is plausible that the veneer was deposited entirely by the Moon-forming impactor. This lack of sufficient veneer on the Moon has also been investigated by Sleep (2016). Their models show that it is possible for the veneer to have moved to the core of the Moon as it was solidifying, without an equivalent event taking place on Earth; however it is still necessary for an impact to have created this essential prebiotic chemistry on the young, solid Earth. Had the compounds necessary to form RNA precursors come from the disk during Earth's formation and absorbed into solids instead of diluting into Earth's oceans, these molecules would not have survived the intense conditions of Earth's formation, especially not the $\sim 10^{24}$ kg Moon forming impact, demonstrating that they were formed in the tens to hundreds of millions of years following this event (Benner et al. 2020).

The lower veneer on the Moon may also be explained through escape of iron under the Moon's lower gravity (Kraus et al. 2015). If this condition were the case to explain the terran to lunar veneer ratio, the Hadean atmosphere would not have been as reduced due to a higher frequency of smaller impacts, lowering the probability of RNA formation (Benner et al. 2020). An impactor of $\sim 10^{21}$ kg or more is sufficient to re-sterilize the surface of Earth, corresponding to the "Ceres" and more massive impactors in this study. While the presence of smaller impactors heat the surface of Earth less, allowing for the formation of RNA precursors earlier due to lack of complete surface sterilization, the transient reducing atmosphere from such impactors would not have lasted as long as one produced by a single, large impactor (Benner et al. 2020). The atmosphere left behind by such a large impactor would need ~ 200 My for the H_2 to fully escape through photodissociation and oxidation (Genda et al. 2017).

3.4.4 Relevance to the Origins of Life

Liquid surface water in the form of a wet-dry cycle is essential for RNA to form via polymerization (Da Silva et al. 2015). This water cycle allows for the delivery of the reduced chemistry to form nucleobases in the warm little ponds, which then polymerize into RNA during the pond’s dry cycle (Pearce et al. 2017). This shows that RNA would have formed under conditions where there is a consistent water cycle like on modern Earth. Without partial pressure of evaporative water, it is not possible to know if our atmospheres are able to sustain the wet-dry cycles necessary for the polymerization of RNA, which motivates future exploration of the early Earth’s complex atmosphere (Pearce et al. 2017).

With the Moon forming impactor constrained to ~ 4.5 Ga, and a single maximum Late Veneer impact occurring at 4.48 Ga (Benner et al. 2020), life must to have formed by 4.3 Ga, within ~ 200 My of the Moon-forming impact, to fit within the chemical window presented by Pearce et al. (2022). While the surface following the impact remains too hot for an order of $\sim 10^6$ years (Benner et al. 2020), and the reducing power of the atmosphere takes ~ 200 My to neutralize via hydrogen escape (Genda et al. 2017), this single impactor would generate the reducing atmosphere needed for producing reduced biomolecule precursors until around ~ 4.36 Ga, which falls within the constraints determined by Pearce et al. (2022). This magma surface would also cool in a time frame on the order of 10^6 years, potentially allowing for the precipitation and evaporation of liquid water soon thereafter. This points again to the greater likelihood of one or very few larger Late Veneer impacts, consistent with our reliable optically thick cases. This work demonstrates that self-consistent calculations of a liquid water cycle and haze formation with H_2 escape over the 200 My following the Moon-forming impact are essential for accurate thermal profiles that will aid in further pinpointing the time-frame for the earliest possible formation of life on Earth, whether the Late Veneer Hypothesis holds true or not.

3.5 Conclusions

How likely is a planet to produce life? This is a complex question that requires a complex solution. Existing exploration using 1D models ignores the computation of radiative transfer and its effects on overall equilibrium chemistry. Analytic treatments following the atmosphere of modern Earth may be an over-simplification of the physical processes involved to both heat and cool the atmosphere, and how these work in conjunction with one another to finalize a surface temperature and steady-state composition. In implementing this approach, we have made several fundamental discoveries.

- **The opacity effects on the radiative transfer must be computed self-consistently.** We find that our self-consistent optically thick models disagree with the analytic surface temperature solutions of Zahnle et al. (2020), becoming hotter than the solution suggests they should be. Evidence in the field of geology and geophysics points toward very optically thick post-impact atmospheres caused by one or few large Hadean Late Veneer impacts. Not only does this self-consistent approach change the thermal profiles of the planet, it can mix the chemistry in ways that may impact the biomolecule yield of the transient atmosphere.
- **H₂ plays an important role in surface temperature.** This post-impact abundance of H₂ may heat the surface enough to extend a habitable zone to a region where a water cycle may not normally occur, possibly allowing RNA to form on now-icy planets. It also greatly heats up the surface of early Earth at higher post-impact pressures, shortening the window for life to form as the surface cools due to hydrogen escape.
- **The impacts of water on an atmosphere are very complex.** Introducing the ability to form water into our models not only increased surface temperatures of the optically thick cases overall, it also adjusted the chemistry. This water further oxidized the dominant chemical species in the CO₂ dominant Max HSE 4 case.

While this water may lend some surface cooling via evaporation or function as a potent greenhouse gas to trap heat further at a planet’s surface, it may also raise the oxidation of the atmosphere, in turn providing less optimal conditions for life to form.

The Late Veneer Hypothesis itself remains poorly understood. Some in the field have worked to disprove this by explaining Earth’s veneer could have formed through other means. It is evidenced, though, that some sort of large impact, be it the Moon forming impact or following, was necessary for the formation of life on Earth. This large impact allows for Earth to possess a reduced chemistry atmosphere in contrast with its otherwise oxidizing conditions, and hold an atmosphere thick enough to act as an incubator under the Faint Young Sun, keeping the surface warm enough to sustain liquid water.

This work highlights the complex problems of both origins of life on Earth and exoplanet habitability for terrestrial planets. The need for a complex solution arises from terrestrial mass planet atmospheric processes including opacity and optical depth, chemistry, latent heat release, and outgassing from adjusting planetary interior, processes that go beyond the non-escaping, steady-state H₂ atmospheres found on Super Earths and more massive planets. We include this self-consistent computation of pressure-variations in chemistry and the impact of forming water on thermal profile and oxidation. Further refinement of models is necessary to tackle these hurdles and work towards pinpointing the exact conditions present on our young Earth. If a planet is given the correct chemistry to create life, what other sets of conditions are necessary for this life to form and thrive?

Bibliography

- Alam, M. K., López-Morales, M., MacDonald, R. J., Nikolov, N., Kirk, J., Goyal, J. M., Sing, D. K., Wakeford, H. R., Rathcke, A. D., Deming, D. L., Sanz-Forcada, J., Lewis, N. K., Barstow, J. K., Mikal-Evans, T., and Buchhave, L. A. (Jan. 2021). Evidence of a Clear Atmosphere for WASP-62b: The Only Known Transiting Gas Giant in the JWST Continuous Viewing Zone. The Astrophysical Journal 906(2), L10.
- Anglada-Escudé, G., Amado, P. J., Barnes, J., Berdiñas, Z. M., Butler, R. P., Coleman, G. A. L., de La Cueva, I., Dreizler, S., Endl, M., Giesers, B., Jeffers, S. V., Jenkins, J. S., Jones, H. R. A., Kiraga, M., Kürster, M., López-González, M. J., Marvin, C. J., Morales, N., Morin, J., Nelson, R. P., Ortiz, J. L., Ofir, A., Paardekooper, S.-J., Reiners, A., Rodríguez, E., Rodríguez-López, C., Sarmiento, L. F., Strachan, J. P., Tsapras, Y., Tuomi, M., and Zechmeister, M. (Aug. 2016). A terrestrial planet candidate in a temperate orbit around Proxima Centauri. 536(7617), 437–440.
- Attwater, J., Wochner, A., and Holliger, P. (Dec. 2013). In-ice evolution of RNA polymerase ribozyme activity. eng. Nature chemistry 5(12). nchem.1781[PII], 1011–1018. ISSN: 1755-4349.
- Avila, P. J., Grassi, T., Bovino, S., Chiavassa, A., Ercolano, B., Danielache, S. O., and Simoncini, E. (Aug. 2021). Presence of water on exomoons orbiting free-floating planets: a case study. International Journal of Astrobiology 20(4), 300–311.
- Ballard, R. D. (1977). NOTES ON A MAJOR OCEANOGRAPHIC FIND. Oceanus 20(3), 35–44.

Bibliography

- Barstow, J. K., Changeat, Q., Garland, R., Line, M. R., Rocchetto, M., and Waldmann, I. P. (Mar. 2020). A comparison of exoplanet spectroscopic retrieval tools. Monthly Notices of the Royal Astronomical Society 493(4), 4884–4909. ISSN: 0035-8711.
- Baudino, J.-L., Mollière, P., Venot, O., Tremblin, P., Bézard, B., and Lagage, P.-O. (Nov. 2017). Toward the Analysis of JWST Exoplanet Spectra: Identifying Troublesome Model Parameters. The Astrophysical Journal 850(2), 150.
- Baudino, J.-L., Bézard, B., Boccaletti, A., Bonnefoy, M., Lagrange, A.-M., and Galicher, R. (2015). Interpreting the photometry and spectroscopy of directly imaged planets: a new atmospheric model applied to toris b and SPHERE observations. A&A 582, A83.
- Belu, A. R., Selsis, F., Morales, J. -C., Ribas, I., Cossou, C., and Rauer, H. (Jan. 2011). Primary and secondary eclipse spectroscopy with JWST: exploring the exoplanet parameter space. 525 A83, A83.
- Benneke, B. (Apr. 2015). Strict Upper Limits on the Carbon-to-Oxygen Ratios of Eight Hot Jupiters from Self-Consistent Atmospheric Retrieval. arXiv e-prints arXiv:1504.07655, arXiv:1504.07655.
- Benner, S. A., Bell, E. A., Biondi, E., Brassier, R., Carell, T., Kim, H.-J., Mojzsis, S. J., Omran, A., Pasek, M. A., and Trail, D. (2020). When Did Life Likely Emerge on Earth in an RNA-First Process? ChemSystemsChem 2(2), e1900035.
- Bernhardt, H. S. and Tate, W. P. (Jan. 2012). Primordial soup or vinaigrette: did the RNA world evolve at acidic pH? eng. Biology direct 7. 1745-6150-7-4[PII], 4. ISSN: 1745-6150.
- Bindeman, I. (Jan. 2008). Oxygen Isotopes in Mantle and Crustal Magmas as Revealed by Single Crystal Analysis. Reviews in Mineralogy and Geochemistry 69(1), 445–478. ISSN: 1529-6466.

Bibliography

- Birkmann, S. M., Ferruit, P., Rawle, T., Sirianni, M., Alves de Oliveira, C., Böker, T., Giardino, G., Lützgendorf, N., Marston, A., Stuhlinger, M., te Plate, M. B. J., Jensen, P., Rumler, P., Dorner, B., Karl, H., Mosner, P., Wright, R. H., and Rapp, R. (July 2016). The JWST/NIRSpec instrument: update on status and performances. In: Space Telescopes and Instrumentation 2016: Optical, Infrared, and Millimeter Wave. Ed. by H. A. MacEwen, G. G. Fazio, M. Lystrup, N. Batalha, N. Siegler, and E. C. Tong. Vol. 9904. Society of Photo-Optical Instrumentation Engineers (SPIE) Conference Series, 99040B.
- Brion, J., Chakir, A., Charbonnier, J., Daumont, D., Parisse, C., and Malicet, J. (June 1998). Absorption Spectra Measurements for the Ozone Molecule in the 350–830 nm Region. Journal of Atmospheric Chemistry 30, 291–299.
- Buck, A. L. (Dec. 1981). New Equations for Computing Vapor Pressure and Enhancement Factor. Journal of Applied Meteorology 20(12), 1527–1532.
- Buck, A. L. (1996). Model CR-1A Hygrometer with Autofill: Operating manual. English. Buck Research Instruments L.L.C. 26 pp. 1996.
- Campbell, B., Walker, G. A. H., and Yang, S. (Aug. 1988). A Search for Substellar Companions to Solar-type Stars. 331, 902.
- Carleo, I. et al. (Aug. 2020). The Multiplanet System TOI-421. The Astronomical Journal 160(3), 114.
- Catling, D. C. and Kasting, J. F. (2017). Atmospheric Evolution on Inhabited and Lifeless Worlds. Cambridge University Press.
- Chandrasekhar, S. (Nov. 1935). The radiative equilibrium of the outer layers of a star, with special reference to the blanketing effect of the reversing layer. 96, 21.
- Chandrasekhar, S. (1960). Radiative transfer.
- Charnay, B., Forget, F., Wordsworth, R., Leconte, J., Millour, E., Codron, F., and Spiga, A. (2013). Exploring the faint young Sun problem and the possible climates of

Bibliography

- the Archean Earth with a 3-D GCM. Journal of Geophysical Research: Atmospheres 118(18), 10, 414–10, 431.
- Charnay, B., Wolf, E., Marty, B., and Forget, F. (July 2020). Is the Faint Young Sun Problem for Earth Solved? Space Science Reviews 216.
- Cnossen, I., Sanz-Forcada, J., Favata, F., Witasse, O., Zegers, T., and Arnold, N. F. (2007). Habitat of early life: Solar X-ray and UV radiation at Earth’s surface 4–3.5 billion years ago. Journal of Geophysical Research: Planets 112(E2).
- Cubillos, P. E. and Bleicic, J. (Aug. 2021). The PYRAT BAY framework for exoplanet atmospheric modelling: a population study of Hubble/WFC3 transmission spectra. 505(2), 2675–2702.
- Da Silva, L., Maurel, M.-C., and Deamer, D. (Feb. 2015). Salt-Promoted Synthesis of RNA-like Molecules in Simulated Hydrothermal Conditions. Journal of Molecular Evolution 80(2), 86–97. ISSN: 1432-1432.
- Debras, F. and Chabrier, G. (Feb. 2019). New Models of Jupiter in the Context of Juno and Galileo. 872(1) 100, 100.
- Deeg, H. J. and Belmonte, J. A. (2018). Handbook of Exoplanets.
- Diamond-Lowe, H., Stevenson, K. B., Bean, J. L., Line, M. R., and Fortney, J. J. (Nov. 2014). New Analysis Indicates No Thermal Inversion in the Atmosphere of HD 209458b. 796(1) 66, 66.
- Dullemond, C. (2012). Lecture Notes in Radiative Transfer.
- Dullemond, C., Zadelhoff, G. V., and Natta, A. (2002). Vertical structure models of T Tauri and Herbig Ae/Be disks. Astronomy and Astrophysics 389, 464–474.
- Elton, D. C. (July 2015). Why physicists still use Fortran.
- Ezer, D. and Cameron, A. (1965). A study of solar evolution. Canadian Journal of Physics 43(8), 1497–1517.

Bibliography

- Fortney, J. J., Ikoma, M., Nettelmann, N., Guillot, T., and Marley, M. S. (Mar. 2011). Self-consistent Model Atmospheres and the Cooling of the Solar System's Giant Planets. *729(1)* 32, 32.
- Fortney, J. J., Lodders, K., Marley, M. S., and Freedman, R. S. (May 2008). A Unified Theory for the Atmospheres of the Hot and Very Hot Jupiters: Two Classes of Irradiated Atmospheres. *678(2)*, 1419–1435.
- Fu, Q. and Liou, K. N. (1992). On the Correlated k-Distribution Method for Radiative Transfer in Nonhomogeneous Atmospheres. *Journal of Atmospheric Sciences* *49(22)*, 2139–2156.
- Fukushi, K., Sekine, Y., Sakuma, H., Morida, K., and Wordsworth, R. (Oct. 2019). Semiarid climate and hyposaline lake on early Mars inferred from reconstructed water chemistry at Gale. *Nature Communications* *10(1)*, 4896. ISSN: 2041-1723.
- Genda, H., Iizuka, T., Sasaki, T., Ueno, Y., and Ikoma, M. (2017). Ejection of iron-bearing giant-impact fragments and the dynamical and geochemical influence of the fragment re-accretion. *Earth and Planetary Science Letters* *470*, 87–95. ISSN: 0012-821X.
- Gillon, M., Triaud, A. H. M. J., Demory, B.-O., Jehin, E., Agol, E., Deck, K. M., Lederer, S. M., de Wit, J., Burdanov, A., Ingalls, J. G., Bolmont, E., Leconte, J., Raymond, S. N., Selsis, F., Turbet, M., Barkaoui, K., Burgasser, A., Burleigh, M. R., Carey, S. J., Chaushev, A., Copperwheat, C. M., Delrez, L., Fernandes, C. S., Holdsworth, D. L., Kotze, E. J., Van Grootel, V., Almlaky, Y., Benkhaldoun, Z., Magain, P., and Queloz, D. (Feb. 2017). Seven temperate terrestrial planets around the nearby ultracool dwarf star TRAPPIST-1. *542(7642)*, 456–460.
- Goody, R., West, R., Chen, L., and Crisp, D. (Dec. 1989). The correlated-k method for radiation calculations in nonhomogeneous atmospheres. *42*, 539–550.

Bibliography

- Goosmann, E. A., Catling, D. C., Som, S. M., Altermann, W., and Buick, R. (2018). Eolianite Grain Size Distributions as a Proxy for Large Changes in Planetary Atmospheric Density. Journal of Geophysical Research: Planets 123(10), 2506–2526.
- Gordon, S. and McBride, B. (1994). Computer Program for Calculation of Complex Chemical Equilibrium Compositions and Applications I. In: NASA Reference Publication 1311.
- Guillot, T. (2010). On the radiative equilibrium of irradiated planetary atmospheres. A&A 520, A27.
- Guillot, T. and Showman, A. P. (Apr. 2002). Evolution of “51 Pegasus b-like” planets. 385, 156–165.
- Haldane, J. B. S. (1929). The origin of life. Rationalist Annual 148, 3–10.
- Harrison, T. M., Blichert-Toft, J., Müller, W., Albarede, F., Holden, P., and Mojzsis, S. J. (2005). Heterogeneous Hadean Hafnium: Evidence of Continental Crust at 4.4 to 4.5 Ga. Science 310(5756), 1947–1950.
- Hatzes, A. P., Cochran, W. D., Endl, M., McArthur, B., Paulson, D. B., Walker, G. A. H., Campbell, B., and Yang, S. (Dec. 2003). A Planetary Companion to Cephei A. The Astrophysical Journal 599(2), 1383–1394.
- Held, I. M. and Soden, B. J. (2000). Water Vapor Feedback and Global Warming. Annual Review of Energy and the Environment 25(1), 441–475.
- Heller, R., Duda, J.-P., Winkler, M., Reitner, J., and Gizon, L. (July 2020). Habitability of the early Earth: Liquid water under a faint young Sun facilitated by strong tidal heating due to a nearby Moon.
- Heng, K., Hayek, W., Pont, F., and Sing, D. K. (Feb. 2012). On the effects of clouds and hazes in the atmospheres of hot Jupiters: semi-analytical temperature-pressure profiles. 420(1), 20–36.
- Heng, K. and Lyons, J. R. (Feb. 2016). Carbon Dioxide in Exoplanetary Atmospheres: Rarely Dominant Compared to Carbon Monoxide and Water in Hot, Hydrogen-dominated Atmospheres. 817(2) 149, 149.

Bibliography

- Henning, T. (Dec. 3, 2020). Personal correspondence.
- Herbort, O., Woitke, P., Helling, C., and Zerkle, A. (Apr. 2020). The atmospheres of rocky exoplanets. I. Outgassing of common rock and the stability of liquid water. 636 A71, A71.
- Hörst, S. M. (2017). Titan’s atmosphere and climate. Journal of Geophysical Research: Planets 122(3), 432–482.
- Hu, R., Seager, S., and Bains, W. (Dec. 2012). PHOTOCHEMISTRY IN TERRESTRIAL EXOPLANET ATMOSPHERES. I. PHOTOCHEMISTRY MODEL AND BENCHMARK CASES. The Astrophysical Journal 761(2), 166.
- Irwin, P. G. J., Teanby, N. A., de Kok, R., Fletcher, L. N., Howett, C. J. A., Tsang, C. C. C., Wilson, C. F., Calcutt, S. B., Nixon, C. A., and Parrish, P. D. (Apr. 2008). The NEMESIS planetary atmosphere radiative transfer and retrieval tool. 109, 1136–1150.
- Jin, S., Mordasini, C., Parmentier, V., Boekel, R. van, Henning, T., and Ji, J. (Oct. 2014). PLANETARY POPULATION SYNTHESIS COUPLED WITH ATMOSPHERIC ESCAPE: A STATISTICAL VIEW OF EVAPORATION. The Astrophysical Journal 795(1), 65.
- Kaltenegger, L. and Traub, W. A. (May 2009). TRANSITS OF EARTH-LIKE PLANETS. The Astrophysical Journal 698(1), 519–527.
- Kasting, J. F. (2013). What caused the rise of atmospheric O₂? Chemical Geology 362(Complete), 13–25. ISSN: 00092541.
- Kasting, J. F., Whitmire, D. P., and Reynolds, R. T. (Jan. 1993). Habitable Zones around Main Sequence Stars. 101(1), 108–128.
- Kite, E. S. and Barnett, M. N. (2020). Exoplanet secondary atmosphere loss and revival. Proceedings of the National Academy of Sciences 117(31), 18264–18271. ISSN: 0027-8424.

- Kitzmann, D., Heng, K., Rimmer, P. B., Hoeijmakers, H. J., Tsai, S.-M., Malik, M., Lendl, M., Deitrick, R., and Demory, B.-O. (Aug. 2018). The Peculiar Atmospheric Chemistry of KELT-9b. *863(2)* 183, 183.
- Koll, D. D. B. and Abbot, D. S. (Mar. 2015). Deciphering Thermal Phase Curves of Dry, Tidally Locked Terrestrial Planets. *802(1)* 21, 21.
- Kratz, D. P. (1995). The correlated k-distribution technique as applied to the AVHRR channels. *Journal of Quantitative Spectroscopy and Radiative Transfer* *53(5)*, 501–517.
- Kraus, R. G., Root, S., Lemke, R. W., Stewart, S. T., Jacobsen, S. B., and Mattsson, T. R. (Apr. 2015). Impact vaporization of planetesimal cores in the late stages of planet formation. *Nature Geoscience* *8(4)*, 269–272. ISSN: 1752-0908.
- Kump, L. R. and Pollard, D. (2008). Amplification of Cretaceous Warmth by Biological Cloud Feedbacks. *Science* *320(5873)*, 195–195.
- Lacis, A. A. and Oinas, V. (1991). A description of the correlated k distributed method for modeling nongray gaseous absorption, thermal emission, and multiple scattering in vertically inhomogeneous atmospheres. *J. Geophys. Res.* *96*, 9027–9063.
- Lenoble, J. (1985). *Radiative transfer in scattering and absorbing atmospheres : standard computation* eng. Studies in geophysical optics and remote sensing. Hampton, Va., USA: A. Deepak. ISBN: 0937194050.
- Line, M. R., Wolf, A. S., Zhang, X., Knutson, H., Kammer, J. A., Ellison, E., Deroo, P., Crisp, D., and Yung, Y. L. (Sept. 2013). A SYSTEMATIC RETRIEVAL ANALYSIS OF SECONDARY ECLIPSE SPECTRA. I. A COMPARISON OF ATMOSPHERIC RETRIEVAL TECHNIQUES. *The Astrophysical Journal* *775(2)*, 137.
- Lü, G., Zhu, C., Wang, Z., and Imminiyaz, H. (Sept. 2017). Effects of Irradiation on the Evolution of Ultracompact X-Ray Binaries. *847(1)* 62, 62.
- MacDonald, R. J. and Madhusudhan, N. (Aug. 2017). HD 209458b in new light: evidence of nitrogen chemistry, patchy clouds and sub-solar water. *469(2)*, 1979–1996.

Bibliography

- Malygin, M. G., Kuiper, R., Klahr, H., Dullemond, C. P., and Henning, T. (2014). Mean gas opacity for circumstellar environments and equilibrium temperature degeneracy. A&A 568, A91.
- Marley, M. S., Saumon, D., Guillot, T., Freedman, R. S., Hubbard, W. B., Burrows, A., and Lunine, J. I. (1996). Atmospheric, Evolutionary, and Spectral Models of the Brown Dwarf Gliese 229 B. Science 272(5270), 1919–1921.
- Mcbride, B. and Gordon, S. (1996). Computer Program for Calculation of Complex Chemical Equilibrium Compositions and Applications II. In: NASA Reference Publication 1311.
- McKay, C. P., Coustenis, A., Samuelson, R. E., Lemmon, M. T., Lorenz, R. D., Cabane, M., Rannou, P., and Drossart, P. (Jan. 2001). Physical properties of the organic aerosols and clouds on Titan. 49(1), 79–99.
- McKay, C. P., Pollack, J. B., and Courtin, R. (1989). The thermal structure of Titan’s atmosphere. Icarus 80(1), 23–53. ISSN: 0019-1035.
- McKay, C. P., Pollack, J. B., and Courtin, R. (Sept. 1991). The greenhouse and anti-greenhouse effects on Titan. English. Science 253. Article, 1118+. ISSN: 00368075.
- Meador, W. E. and Weaver, W. R. (1980). Two-Stream Approximations to Radiative Transfer in Planetary Atmospheres: A Unified Description of Existing Methods and a New Improvement. Journal of Atmospheric Sciences 37(3), 630–643.
- Mihalas, D., Auer, L. H., and Mihalas, B. R. (Mar. 1978). Two-dimensional radiative transfer. I. Planar geometry. 220, 1001–1023.
- Miller, S. L. and Urey, H. C. (1959). Organic Compound Synthesis on the Primitive Earth. Science 130(3370), 245–251.
- Molaverdikhani, K., Henning, T., and Mollière, P. (Oct. 2019). From Cold to Hot Irradiated Gaseous Exoplanets: Fingerprints of Chemical Disequilibrium in Atmospheric Spectra. The Astrophysical Journal 883(2), 194.

- Mollière, P., Boekel, R., Dullemond, C., Henning, T., and Mordasini, C. (2015). Model atmospheres of irradiated exoplanets: The influence of stellar parameters, metallicity, and the C/O ratio. The Astrophysical Journal 813, 47.
- Mollière, P. and Snellen, I. A. G. (2018). Detecting isotopologues in exoplanet atmospheres using ground-based high-dispersion spectroscopy. A&A 622, A139.
- Mollière, P., van Boekel, R., Bouwman, J., Henning, T., Lagage, P. -O., and Min, M. (Apr. 2017). Observing transiting planets with JWST. Prime targets and their synthetic spectral observations. 600 A10, A10.
- Mollière, P., Wardenier, J., Boekel, R. van, Henning, T., Molaverdikhani, K., and Snellen, I. (2019). petitRADTRANS. A Python radiative transfer package for exoplanet characterization and retrieval. Astronomy and Astrophysics 627.
- Mollière, P. (July 2017). Modeling of Exoplanet Atmospheres. [Doctoral dissertation, Universität Heidelberg]
- Mollière, P. (Dec. 5, 2020). Personal correspondence.
- Mollière, P. (2021a). Personal correspondence.
- Mollière, P. (Nov. 2021b). Zoom meeting.
- Mordasini, C. (June 11, 2020). Personal correspondence.
- Nakamoto, T. and Nakagawa, Y. (Feb. 1994). Formation, Early Evolution, and Gravitational Stability of Protoplanetary Disks. 421, 640.
- Newman, M. J. and Rood, R. T. (1977). Implications of Solar Evolution for the Earth's Early Atmosphere. Science 198(4321), 1035–1037.
- Newsom, H. E. and Ross Taylor, S. (Mar. 1989). Geochemical implications of the formation of the Moon by a single giant impact. Nature 338(6210), 29–34. ISSN: 1476-4687.
- Newton, I. (1726). Philosophiæ naturalis principia mathematica. Includes index. Editio tertia, aucta & emendata. Londini : Apud G. & J. Innys, 1726.
- Nisbet, E. G. and Fowler, C. M. R. (Aug. 1996). Some liked it hot. Nature 382(6590), 404–405. ISSN: 1476-4687.

Bibliography

- O’Connell, D. and (VATICAN), P. A. S. (1958). Stellar Populations. Proceedings of the Conference Spoleto, Castel Gandolfo, Italy. Specola Astronomica Vaticana. Ricerche astronomiche. North Holland Publishing Company.
- Oparin, A. I. (1938). The origin of life.
- Osterbrock, D. E. (Nov. 1953). The Internal Structure of Red Dwarf Stars. 118, 529.
- Otegi, J. F., Bouchy, F., Helled, R., Armstrong, D. J., Stalport, M., Psaridi, A., Delisle, J. -B., Stassun, K. G., Delgado-Mena, E., Santos, N. C., Hara, N. C., Collins, K., Gandhi, S., Dorn, C., Brogi, M., Fridlund, M., Osborn, H. P., Hoyer, S., Udry, S., Hojjatpanah, S., Nielsen, L. D., Dumusque, X., Adibekyan, V., Conti, D., Schwarz, R., Wang, G., Figueira, P., Lillo-Box, J., Hadjigeorghiou, A., Bayliss, D., Strøm, P. A., Sousa, S. G., Barrado, D., Osborn, A., Barros, S. C. C., Brown, D. J. A., Eastman, J. D., Ciardi, D. R., Vanderburg, A., Goeke, R. F., Guerrero, N. M., Boyd, P. T., Caldwell, D. A., Henze, C. E., McLean, B., Ricker, G., Vanderspek, R., Latham, D. W., Seager, S., Winn, J., and Jenkins, J. M. (Sept. 2021). TESS and HARPS reveal two sub-Neptunes around TOI 1062. 653 A105, A105.
- Parmentier, V. and Guillot, T. (2014). A non-grey analytical model for irradiated atmospheres - I. Derivation. A&A 562, A133.
- Parmentier, V., Guillot, T., Fortney, J. J., and Marley, M. S. (Feb. 2015). A non-grey analytical model for irradiated atmospheres. II. Analytical vs. numerical solutions. 574 A35, A35.
- Pearce, B. K. D., Molaverdikhani, K., Pudritz, R. E., Henning, T., and Cerrillo, K. E. (2022). Constraining the Time Interval for the Origin of Life on Earth. Accepted by The Astrophysical Journal.
- Pearce, B. K. D., Molaverdikhani, K., Pudritz, R. E., Henning, T., and Hébrard, E. (Oct. 2020). HCN Production in Titan’s Atmosphere: Coupling Quantum Chemistry and Disequilibrium Atmospheric Modeling. 901(2) 110, 110.

Bibliography

- Pearce, B. K. D., Pudritz, R. E., Semenov, D. A., and Henning, T. K. (2017). Origin of the RNA world: The fate of nucleobases in warm little ponds. Proceedings of the National Academy of Sciences 114(43), 11327–11332. ISSN: 0027-8424.
- Pearce, B. K. D., Tupper, A. S., Pudritz, R. E., and Higgs, P. G. (Mar. 2018). Constraining the Time Interval for the Origin of Life on Earth. Astrobiology 18(3), 343–364.
- Peretó, J., Bada, J. L., and Lazcano, A. (Oct. 2009). Charles Darwin and the Origin of Life. Origins of Life and Evolution of Biospheres 39(5), 395–406. ISSN: 1573-0875.
- Pierrehumbert, R. T. (2010). Principles of Planetary Climate.
- Planavsky, N., Asael, D., Hofmann, A., Reinhard, C., Lalonde, S., Knudsen, A., Wang, X., Ossa Ossa, F., Pecoits, E., Smith, A., Beukes, N., Bekker, A., Johnson, T., Konhauser, K., Lyons, T., and Rouxel, O. (Apr. 2014). Evidence for oxygenic photosynthesis half a billion years before the Great Oxidation Event. English (US). Nature Geoscience 7(4). Funding Information: N.J.P. acknowledges financial support from NSF EAR-PF; O.J.R. and D.A. from Europe Mer and ANR-10-LABX-19-01; A.H. and F.O.O. from the NRF of South Africa and Acclaim Exploration; S.V.L. from NSERC-PF and LabexMer-PF; K.O.K. from NSERC; N.J.P., T.W.L., C.T.R. and T.M.J. from NASA Exobiology; and T.W.L. from NSF EAR. C. Delvigne, J. Hancox and N. Hicks provided access to drill core and samples; E. Ponzevera and Y. Germain provided technical assistance., 283–286. ISSN: 1752-0894.
- Poser, A. J., Nettelmann, N., and Redmer, R. (Oct. 2019). The Effect of Clouds as an Additional Opacity Source on the Inferred Metallicity of Giant Exoplanets. Atmosphere 10(11), 664.
- Press, W. H., Flannery, B. P., Teukolsky, S. A., and Vetterling, W. T. (Sept. 1992). Numerical Recipes in FORTRAN 77: The Art of Scientific Computing. 2nd ed. Cambridge University Press. ISBN: 052143064X.

Bibliography

- Ramirez, R. and Kaltenegger, L. (Feb. 2017). A Volcanic Hydrogen Habitable Zone. The Astrophysical Journal Letters 837.
- Al-Refaie, A. F., Changeat, Q., Waldmann, I. P., and Tinetti, G. (Aug. 2021). TauREx 3: A Fast, Dynamic, and Extendable Framework for Retrievals. 917(1) 37, 37.
- Ricker, G. R., Winn, J. N., Vanderspek, R., Latham, D. W., Bakos, G. Á., Bean, J. L., Berta-Thompson, Z. K., Brown, T. M., Buchhave, L., Butler, N. R., Butler, R. P., Chaplin, W. J., Charbonneau, D., Christensen-Dalsgaard, J., Clampin, M., Deming, D., Doty, J., De Lee, N., Dressing, C., Dunham, E. W., Endl, M., Fressin, F., Ge, J., Henning, T., Holman, M. J., Howard, A. W., Ida, S., Jenkins, J. M., Jernigan, G., Johnson, J. A., Kaltenegger, L., Kawai, N., Kjeldsen, H., Laughlin, G., Levine, A. M., Lin, D., Lissauer, J. J., MacQueen, P., Marcy, G., McCullough, P. R., Morton, T. D., Narita, N., Paegert, M., Palle, E., Pepe, F., Pepper, J., Quirrenbach, A., Rinehart, S. A., Sasselov, D., Sato, B., Seager, S., Sozzetti, A., Stassun, K. G., Sullivan, P., Szentgyorgyi, A., Torres, G., Udry, S., and Villaseñor, J. (Jan. 2015). Transiting Exoplanet Survey Satellite (TESS). Journal of Astronomical Telescopes, Instruments, and Systems 1 014003, 014003.
- Rimmer, P. B. and Shorttle, O. (Jan. 2019). Origin of Life's Building Blocks in Carbon- and Nitrogen-Rich Surface Hydrothermal Vents. eng. Life (Basel, Switzerland) 9(1). life9010012[PII], 12. ISSN: 2075-1729.
- Rogers, L. A. (2015). Most 1.6 Earth-radius planets are not rocky. The Astrophysical Journal 801(1), 41.
- Rosing, M. T. (1999). ¹³C-Depleted Carbon Microparticles in >3700-Ma Sea-Floor Sedimentary Rocks from West Greenland. Science 283(5402), 674–676.
- Rosing, M. T., Bird, D. K., Sleep, N. H., and Bjerrum, C. J. (Apr. 2010). No climate paradox under the faint early Sun. Nature 464(7289), 744–747. ISSN: 1476-4687.
- Russell, M. J., Daniel, R. M., and Hall, A. J. (1993). On the emergence of life via catalytic iron-sulphide membranes. Terra Nova 5(4), 343–347.

Bibliography

- Rybicki, G. B. and Lightman, A. P. (1986). Radiative Processes in Astrophysics.
- Sagan, C. and Mullen, G. (1972). Earth and Mars: Evolution of Atmospheres and Surface Temperatures. Science 177(4043), 52–56.
- Schlesinger, G. and Miller, S. L. (1983). Prebiotic synthesis in atmospheres containing CH₄, CO, and CO₂. Journal of molecular evolution 19(5), 383–390.
- Schoonen, M. A. and Xu, Y. (2001). Nitrogen Reduction Under Hydrothermal Vent Conditions: Implications for the Prebiotic Synthesis of C-H-O-N Compounds. Astrobiology 1(2). PMID: 12467117, 133–142.
- Schwarzschild, M., Howard, R., and Härm, R. (Jan. 1957). Inhomogeneous Stellar Models. V. a. Solar Model with Convective Envelope and Inhomogeneous Interior. 125, 233.
- Schwarzschild, M. (1958). Structure and Evolution of Stars. Princeton University Press. ISBN: 9781400879175.
- Seager, S., Bains, W., and Hu, R. (Oct. 2013). A Biomass-based Model to Estimate the Plausibility of Exoplanet Biosignature Gases. 775(2) 104, 104.
- Shields, A. L. (Aug. 2019). The Climates of Other Worlds: A Review of the Emerging Field of Exoplanet Climatology. 243(2) 30, 30.
- Sleep, N. H. (June 2010). The Hadean-Archaeon Environment. Cold Spring Harbor Perspectives In Biology 2(6).
- Sleep, N. H. (2016). Asteroid bombardment and the core of Theia as possible sources for the Earth's late veneer component. Geochemistry, Geophysics, Geosystems 17(7), 2623–2642.
- Som, S. M., Catling, D. C., Harnmeijer, J. P., Polivka, P. M., and Buick, R. (Apr. 2012). Air density 2.7 billion years ago limited to less than twice modern levels by fossil raindrop imprints. Nature 484(7394), 359–362. ISSN: 1476-4687.
- Stribling, R. and Miller, S. L. (Sept. 1987). Energy yields for hydrogen cyanide and formaldehyde syntheses: The hcn and amino acid concentrations in the primitive ocean. Origins of life and evolution of the biosphere 17(3), 261–273. ISSN: 1573-0875.

Bibliography

- Toon, O. B., McKay, C. P., Ackerman, T. P., and Santhanam, K. (1989). Rapid calculation of radiative heating rates and photodissociation rates in inhomogeneous multiple scattering atmospheres. Journal of Geophysical Research: Atmospheres 94(D13), 16287–16301.
- Tremblin, P., Amundsen, D. S., Mourier, P., Baraffe, I., Chabrier, G., Drummond, B., Homeier, D., and Venot, O. (May 2015). Fingering Convection and Cloudless Models for Cool Brown Dwarf Atmospheres. 804(1) L17, L17.
- Valley, J. W., Lackey, J. S., Cavosie, A. J., Clechenko, C. C., Spicuzza, M. J., Basei, M. A. S., Bindeman, I. N., Ferreira, V. P., Sial, A. N., King, E. M., Peck, W. H., Sinha, A. K., and Wei, C. S. (Dec. 2005). 4.4 billion years of crustal maturation: oxygen isotope ratios of magmatic zircon. Contributions to Mineralogy and Petrology 150(6), 561–580.
- Venot, O., Hébrard, E., Agúndez, M., Dobrijevic, M., Selsis, F., Hersant, F., Iro, N., and Bounaceur, R. (2012). A chemical model for the atmosphere of hot Jupiters. A&A 546, A43.
- Wacey, D., Kilburn, M., Saunders, M., Cliff, J., and Brasier, M. (2011). Microfossils of sulphur-metabolizing cells in 3.4-billion-year-old rocks of Western Australia. English. Nature Geoscience 4, 698–702. ISSN: 1752-0894.
- Waldmann, I. P., Tinetti, G., Rocchetto, M., Barton, E. J., Yurchenko, S. N., and Tennyson, J. (Mar. 2015). TAU-REX I: A NEXT GENERATION RETRIEVAL CODE FOR EXOPLANETARY ATMOSPHERES. The Astrophysical Journal 802(2), 107.
- Watson, E. B. and Harrison, T. M. (2005). Zircon Thermometer Reveals Minimum Melting Conditions on Earliest Earth. Science 308(5723), 841–844.
- Wilde, S. A., Valley, J. W., Peck, W. H., and Graham, C. M. (Jan. 2001). Evidence from detrital zircons for the existence of continental crust and oceans on the Earth 4.4 Gyr ago. Nature 409(6817), 175–178. ISSN: 1476-4687.

Bibliography

- Chapter 6 - Vertical structure of the moist atmosphere (2021). In: Thermal Physics of the Atmosphere (S. S. Stevens, Ed. by P. D. Williams and M. H. P. Ambaum. Second Edition. Developments in Weather and Climate Science. Elsevier, 115–132. ISBN: 978-0-12-824498-2.
- Yelle, R. V., Strobell, D. F., Lellouch, E., and Gautier, D. (Jan. 1997). The Yelle Titan Atmosphere Engineering Models. In: Huygens: Science, Payload and Mission. Ed. by A. Wilson. Vol. 1177. ESA Special Publication, 243.
- Yin, J. and Zhao, M. (Oct. 2021). Influence of the Atlantic meridional overturning circulation on the U.S. extreme cold weather. Communications Earth & Environment 2(1), 218. ISSN: 2662-4435.
- Younkin, R. L. (Mar. 1974). The Albedo of Titan. 21(3), 219–229.
- Zahnle, K. J. (1986). Photochemistry of methane and the formation of hydrocyanic acid (HCN) in the Earth's early atmosphere. Journal of Geophysical Research: Atmospheres 91(D2), 2819–2834.
- Zahnle, K. J., Catling, D. C., and Claire, M. W. (2013). The rise of oxygen and the hydrogen hourglass. Chemical Geology 362(Complete), 26–34. ISSN: 00092541.
- Zahnle, K. J., Lupu, R., Catling, D. C., and Wogan, N. (May 2020). Creation and Evolution of Impact-generated Reduced Atmospheres of Early Earth. The Planetary Science Journal 1(1), 11.
- Zilinskas, M., Miguel, Y., Lyu, Y., and Bax, M. (Nov. 2020). Temperature inversions on hot super-Earths: the case of CN in nitrogen-rich atmospheres. Monthly Notices of the Royal Astronomical Society 500(2), 2197–2208. ISSN: 0035-8711.